CFD SIMULATION AND EXPERIMENTAL TESTING OF MULTIPHASE FLOW INSIDE THE MVP ELECTRICAL SUBMERSIBLE PUMP

A Dissertation

by

EMANUEL GUIRGUIS RASMY MARSIS

Submitted to the Office of Graduate Studies of
Texas A&M University
in partial fulfillment of the requirements for the degree of

DOCTOR OF PHILOSOPHY

Approved by:

Chair of Committee,	Gerald L. Morrison
Committee Members,	Debjyoti Banerjee
	Andrew T. Duggleby
	Robert E. Randall
Head of Department,	Jerald A. Caton

December 2012

Major Subject: Mechanical Engineering

ABSTRACT

The MVP is a special type of Electrical Submersible Pumps (ESPs) manufactured by Baker Hughes, model no. G470, and is capable of handling multiphase flow up to 70% Gas Volume Fraction (GVF). Flows at high GVF cause conventional ESPs to surge. However, the special design of the impeller blades of the MVP ESP enables it to handle higher GVF. Dynamic behavior of the multiphase flow is studied experimentally and theoretically for this pump for the first time. In this work, a Computational Fluid Dynamics (CFD) simulation of an entire pump and detailed experimental analysis are performed.

Meshing and CFD simulations are performed using the commercially available software ANSYS Fluent. An experimental facility has been designed and constructed to test the pump at different operating conditions. The pump is modeled and tested at two speeds; 3300 and 3600 rpm, using air-water mixtures with GVFs of 0, 5, 10, 25, 32 and 35%. The flow loop is controlled to produce different suction pressures up to 300psi. Pump pressure head is used to validate the CFD model for both single and two phase flows. Single phase CFD model was validated at 100 psi inlet pressure, while two phase models were validated at 200 psi inlet pressure. CFD simulations can predict the behavior of the pump at different speeds, flow rates, GVFs, and inlet pressures. Different diffuser designs are studied and simulated to improve the multistage pump performance. Enhanced diffuser designs increased the pump pressure head to up to 3.2%.

DEDICATION

To my loving parents and sisters

ACKNOWLEDGEMENTS

I would like to start by thanking my committee chair, Dr. Gerald Morrison for all his help, support, understanding and guidance. I would like also to thank him for accepting me as a PhD student in his team, and for being a great boss who always made himself available for his students. Special thanks to Dr. Morrison for trusting me and believing in me and encouraging me throughout my research.

I would also like to thank my committee members, Dr. Banerjee, Dr. Duggleby, and Dr. Randall, for their guidance and support throughout the course of this research.

Thanks also to my friends and colleagues and staff in the turbolab for making my time at Texas A&M University a great experience.

Thanks to Sahand Pirouzpanah for his help and support.

Thanks to Dr. Stuart Scott and Dr. Lissett Barrios for their guidance, help and support.

Thanks to Shell Oil for funding this project, and providing me with all the knowledge and information I needed throughout my research.

Finally, thanks to my mother, father, sisters for their encouragement, without their support I could not accomplish this.

NOMENCLATURE

β	Coefficient of thermal expansion
CFD	Computational Fluid Dynamics
C_1 , C_2 , C , $_k$,	Constants for K-epsilon model
	Density
y^*	Dimensionless velocity near wall
y_p	Distance from point p to the wall
μ	Dynamic viscosity
$\hat{\rho}_q$	Effective density of the phase q
ESP	Electrical Submersible Pump
E	Empirical constant (=9.793)
F	Force vector
GPM	Gallons per Minute
GVF	Gas Volume Fraction
P_b	Generation of turbulent kinetic energy due to buoyancy
P_k	Generation of turbulent kinetic energy due to the mean velocity gradient
g_i	Gravity vector
$\bar{q}$	Heat flux
Q_{pq}	Intensity of the heat exchange between the two phases
ν	Kinetic viscosity

U_c	Mean velocity magnitude
S	Modulus of the mean rate of strain tensor
P_r	Molecular Prandtl number for energy
ρ_{yq}	Phase reference density of the phase q
a_q	Phasic volume fraction
P_{rt}	Prandtl number for energy
S_q	Source term that includes the source enthalpy
h	Specific enthalpy
c_p	Specific heat of the fluid
$\bar{\tau}$	Stress-strain tensor
T	Temperature of the fluid
T_ω	Temperature of the fluid at the wall
T_p	Temperature of the fluid to the cell adjacent to the wall
	Turbulent dissipation rate
k	Turbulent kinetic energy
k_p	Turbulent kinetic energy at the near-wall node p
$_t$	Turbulent viscosity
V_q	Volume fraction of phase q
A	Van Driest constant (=26)
κ	Von Karman constant (=0.4187)

TABLE OF CONTENTS

Page

LIST OF FIGURES

Page

LIST OF TABLES

Page

1. INTRODUCTION

Electrical Submersible Pump (ESP) systems have been widely used by the oil and gas industry for artificial lift. The idea behind an ESP system is based on the electrical transmission of power to a centrifugal pump that is operating in a vertical position inside the well bore. The pump consists of a multistage stack of impellers and diffusers as seen in Fig. 1. Each stage consists of an impeller that is connected to the pump shaft that rotates at different speeds and a stationary diffuser that redirects the flow from the outlet of the previous impeller to the inlet of the next impeller. The pump stages increase the pressure head across the pump providing the head needed to transport the fluids.

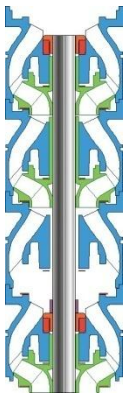

Figure 1. Electrical submersible pump (ESP)

Currently ESPs are used to pump the mixture of oil and gas in production oil wells. Since ESPs are mainly centrifugal pumps, their performance highly depends on the amount of the gas in the pumped mixture. When pumping mixed flow; liquid and

gas, entrapped gas can affect the pump performance in many ways ranging from a small degradation to complete flow blocking known as “gas locking”, (Pessoa and Prado 2003). A study was performed in the University of Tulsa (Barrios 2007), that included theoretical and experimental visualization of multiphase flow in a conventional ESP. Barrios concluded that the accumulation of gas inside the impeller in the form of gas pockets caused pump head degradation. The same exact phenomenon occurs in centrifugal pumps as well.

With the increasing demand of oil and gas as one of the major sources of energy, many companies are interested in utilizing the ESP technology as means of handling high GVF flows in oil and gas wells. Baker Hughes designed and manufactures a special type ESP that is proven to handle higher GVF than conventional ESPs. The MVP ESP designed and manufactured by Baker Hughes has a special impeller (Fig. 2) that enables the pump to handle higher GVF flows than nominal ESPs.

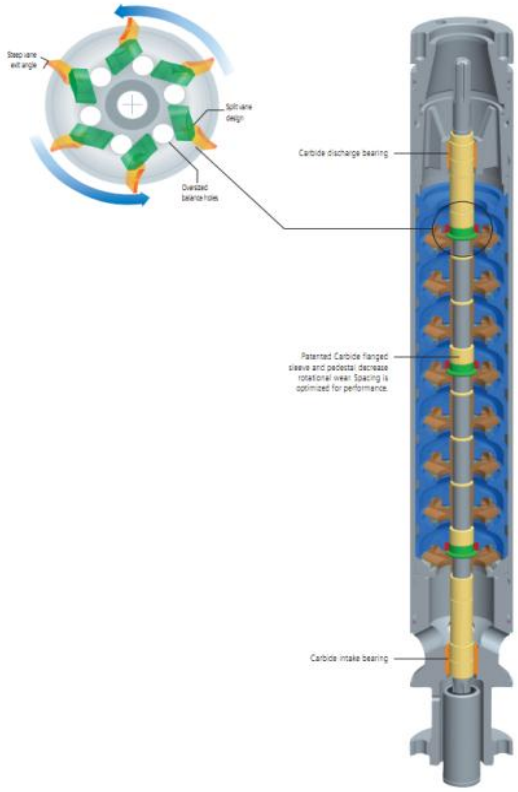

Figure 2. Baker Hughes MVP ESP

The patented impeller design enables the pump to provide more mixing for gas and liquid than conventional impeller ESPs. The MVP pump can be used alone in an ESP system, or it can be assembled in series with other conventional ESPs that will provide higher pressure head while the MVP provides more homogenous flow through better mixing of liquid and gas. Thus, MVP pumps can be used first, as each stage reduces the GVF and provide higher pressure head until standard ESP stages will work and have higher efficiency.

Predicting the pump performance for two phase flow theoretically has been of great importance lately. CFD modeling and simulation for different ESPs that handle two phase flows has been attempted previously. However, due to highly sophisticated geometry of the MVP and the high GVFs that it handles many CFD solvers could not converge or reach an accurate solution using different models. The objective of this research is to present a CFD model that can predict and analyze the two phase flow inside the MVP ESP, and also be utilized as a design tool that can improve the pump design, and hence increasing the pump efficiency.

1.1 CFD modeling and validation

Simple numerical modeling for pumps started back in the 1970's. Many analytical one dimensional models were attempted by researchers such as Mikielewicz et al. (1978), Wilson et al. (1979), and Zakem (1980). In their research, Mikielewics, Wilson, and Zakem depended on semi empirical formulas that require some experimental information. Later on, starting in the 1980's, researchers developed a one dimensional model based on the streamline approach as shown in the works presented in Furuya (1985), Sachdeva et al. (1994), Minemura et al. (1998), and Sun (2002).

Later in the 1990's researchers had access to computers with more memory and powerful processors that could handle complicated problems. Computational Fluid Dynamics (CFD) became a useful tool in simulating complicated geometries using different types of models like the Reynolds Average Navier-Stokes Equation (RANS),

and Large Eddy Simulation (LES). In 1998 Pak and Lee (1998) used a 3D RANS model utilizing the K-epsilon model and a bubbly flow assumption to simulate a two phase flow in a centrifugal impeller. This model was based on water-air mixture that used a void fraction variable with a single set of continuity, energy, and momentum equations. The CFD simulation results for both the void fraction and pressure distribution agreed with the experimental results.

Medvitz et al. (2002) used multiphase CFD analysis to study the cavitating flow inside a centrifugal pump. The authors used the two-phase homogenous RANS equations. The simulation included both steady state and transient analysis for different flow coefficients and different cavitation numbers and could successfully predict cavitation inside the pump. Gonzalez et al. (2002) conducted many CFD analyses to study the rotor-stator interaction in a centrifugal pump. The authors compared the transient data from the simulation with the experimental results. They also utilized Finite Element Analysis (FEM) to perform a fluid structure interaction study on the blades of the rotor.

Schilling and Frobenius (2002) also used one set of equations to simulate a two phase flow in three dimensions with a very low GVF; less than 4%. Schilling and Frobenius assumed the same velocity of the two phases and used a mixture density to describe the flow. Their objective was to build a model that would consume less computational time. Moreover, the model could not predict higher GVF flows. Byskov and Pedersen (2003) detected separation in the shrouded impeller of a centrifugal pump using LES that agreed with PIV experimental data.

In 2004, Benra and Dohmen (2004) used a commercial CFD solver to compute a 3D simulation of a centrifugal pump. The 3D simulation was able to predict the periodic forces that the flow exerts on the impeller. A Finite Element Model (FEM) was used to analyze the vibrations response on the impeller due to the hydrodynamic forces. The predicted vibrations frequency and amplitude agreed with the experimental data. In the same year, Caridad and Kenyery (2004) simulated two phase flow in an ESP using a 3D CFD model. Caridad and his team found that when the GVF increased, the degradation of the pump head increased as well. The authors used a 3D model to predict the pressure distribution and the void fraction distribution inside the impeller of an ESP. Also, in their research, Caridad and Kenyery were able to detect the gas pocket on the pressure side of the pump impeller as other researchers predicted as well. In his model, Caridad assumed a bubble diameter of 5 mm. As seen in Fig. 3, the gas pocket accumulated increased in size when the GVF increased, which caused more degradation of the pump head. This explains the phenomenon of the gas lock in the normal ESP when it operates at high GVFs.

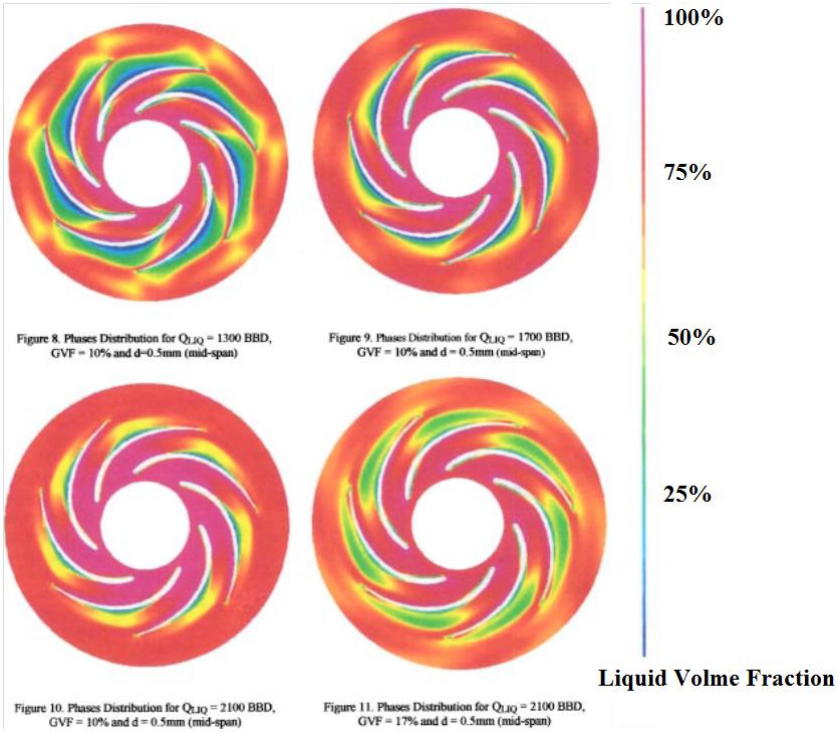

Figure 3. Liquid volume fraction distribution for different flow conditions (Caridad and Kenyery 2004)

In 2005, Majidi (2005) performed a study that included a 3D simulation of a centrifugal pump. The author used transient CFD analysis to simulate the flow in both the impeller and the diffuser. The main objective of the study was to determine the unsteady blade loading. Majidi was able to detect the pressure fluctuation of the flow due to the interaction between the impeller blade and the volute tongue.

Bonaiuti et al. (2006) were able to utilize a 3D CFD solver for the analysis and design optimization of a centrifugal compressor. They used Bezier curve to design the compressor blades and used a CFD-based optimization iterative process to reach the optimum compressor design and also understand the effect of different parameters on the

compressor performance. Gonzalez and Santolaria (2006) predicted the separation in the volute of a centrifugal pump. They also validated their CFD model by comparing different variables, like pressure head, power, and pump efficiency with experimental data.

In 2006, Yedidiah (2006a, 2006b) established a design optimization method using CFD for pump design. Two years later, Dostal et al. (2008) performed a CFD study to simulate and analyze the two phase flow inside a Pb-Bi cooled direct contact steam generation fast reactor. The authors used a 2D simulation model to simplify the original problem. They used mass flow inlet and pressure outlet as the boundary conditions. They also used Volume of Fluid (VOF) model available in ANSYS Fluent commercial software, to simulate the two phases. The model showed very good agreement with the experimental data. In the same year, Yang et al. (2008) investigated the two phase flow inside a coiled tube. The study included both numerical and experimental analysis. They used a high speed camera to visualize the flow transiently in the pipe, and they matched the experimental data with transient numerical simulation. The authors assumed no slip velocity and used the VOF model available in Fluent. The authors also used realizable K-epsilon turbulence model but they had to keep the Under Relaxation Factors (URF) below 0.2 to get the CFD model to converge.

In 2009, Barrios and Prado (2009) studied the dynamic behavior of the multiphase flow inside an ESP. They utilized the bubble size to model the flow inside the ESP and predicted the optimum operating conditions for the pump. They measured the bubble size experimentally using high speed camera and used this dimension in the

CFD model. The bubble size was measured at the impeller intake. Barrios and Prado found out that the bubbles collected at the impeller blade leading edge (at the pump intake), and at higher GVF, gas pockets are formed on the impeller blade pressure side. Feng et al. (2009), performed a study to visualize the flow inside a radial diffuser pump. Their study included both CFD analysis and PIV experimental visualization of the flow as well. The pump was simulated using Detached Eddy Simulation (DES) turbulence model that was able to predict the flow field inside the pump. The simulation showed good agreement with the experimental PIV data. The authors were able to observe separation on the suction side of the impeller where the highest turbulence occurred. Kaewnai et al. (2009), conducted a CFD study on a radial flow type impeller of a centrifugal pump. The authors used CFD analysis to predict the pump performance and compare it to the experimental data from previous literature. In their work, Kaewnai et al. used single phase flow with water as the working fluid. They used different K-epsilon models in their study. The mesh used was all structured hexahedral type mesh and the maximum residual convergence was 10^{-4}. The model showed very good agreement with the experimental data and hence they concluded that CFD modeling can be used to predict flows in other radial-flow type impellers in centrifugal pumps.

Jayakumar et al. (2010) used CFD to simulate the two phase flow of air and water inside helical pipes. The authors used the Euler-Euler scheme that solves different set of equations for each phase unlike the VOF model that uses one set of equation with varying the volume fraction of one phase only. The advantage of using Euler-Euler model is that it shows the slip velocity between the two phases. The authors used Green

Gauss cell gradient pressure based model together with a pressure velocity coupled simple model. In their simulation, Jayakumar et al. used QUICK scheme for momentum and void fraction equations, and used Power-Law, which is a second order scheme, for turbulent kinetic energy and dissipation rate equations. They assumed an isothermal model with no change in temperature across the whole flow.

1.2 Experimental analysis of fluid flow in pumps

Literature focusing on the experimental analysis of different types of pumps including centrifugal and ESP pumps exists. Many experimental works have been conducted to test pumps and determine pump curves to find the optimum operating point of the pump. Experimental testing included measuring pressure heads, power consumption, flow rates, flow visualization, bubble size measurement in two phase flows, and void fraction distribution. Most of this work was conducted on centrifugal pumps with volute diffusers, and very limited work investigated the ESP pump impeller, and no work was done to study the flow in the ESP diffusers.

In 1974, Murakami and Minemura (1974a) conducted one of the most important experimental tests to understand the behavior of the two phase flow inside a centrifugal pump. The pump type was a semi open impeller, and the casing used was a transparent acrylic casing that enabled them to visualize the flow using a camera. They conducted their tests at different flow rates and GVFs. At low GVF and high flow rates, the flow

was homogenous and the bubbles had a uniform distribution in the flow, but more bubbles tended to adhere to the pressure side of the blade. However, at higher GVF more gas adhered to the pressure side of the blade, where no pressure increment is observed, causing the formation of a gas pocket on the blade. This phenomenon is shown below in Fig. 4 and it is in agreement with the CFD analysis of the similar pump shown above in Fig. 3.

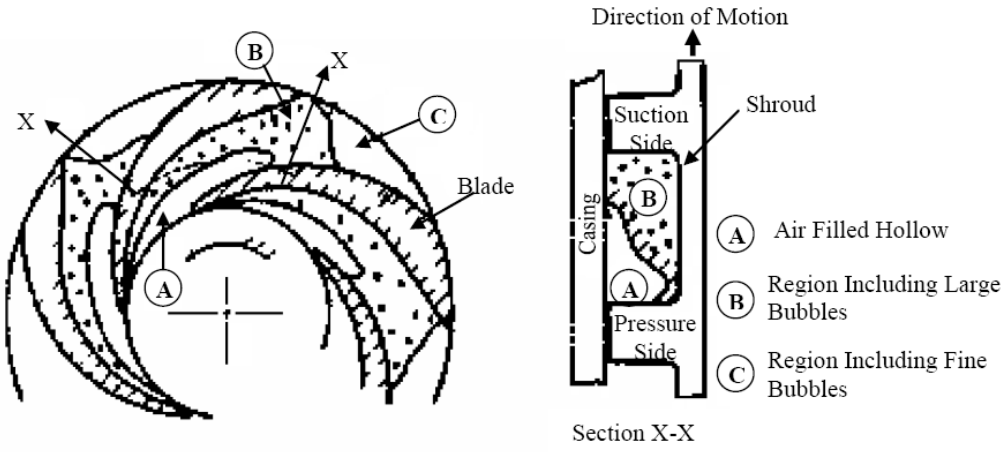

Figure 4. Centrifugal impeller channel flow pattern (Murakami and Minemura 1974a)

In their research, Murakami and Minemura also found that the GVF directly affected the flow pattern of the mixed flow inside the impeller. This was mainly due to the density change of the mixture that directly affected the momentum of the flow, and hence the direction and the pattern of the flow. Moreover, the authors observed a negative pressure gradient at the leading edge of the blade that reduced the speed of the air bubbles causing another accumulation of some air bubbles on the suction side of the

impeller blade near the blade leading edge. This phenomenon, as seen in Fig. 5, reduced the area of the flow, and directly affected the magnitude and direction of the velocity vectors of the flow.

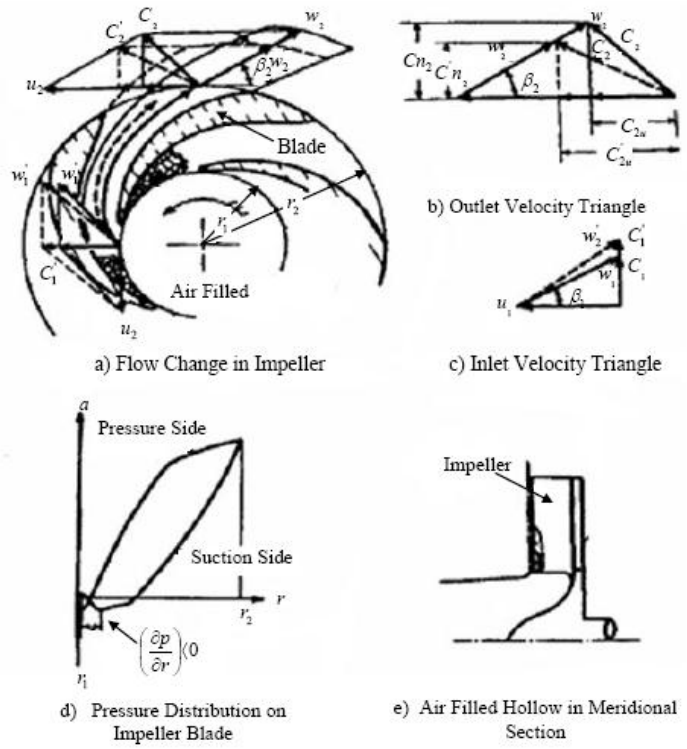

Figure 5. Flow pattern change at low GVF (Murakami and Minemura 1974a)

During their research, Murakamiand Minemura observed instability and a strong vibration response in the pump at higher GVF. In this running condition, the authors observed a large air pocket on the blade pressure side. These low density air pockets accumulated on the impeller blades causing the impeller to be unbalanced and hence

unstable. The authors also found that when the GVF increased it increased the head degradation in the pump causing more losses in the pressure head.

In another study conducted by Murakami and Minemura (1974b) in the same year, the authors studied the effect of changing the number of impeller blades on the two phase flow pattern. The authors were able to measure the bubble size and they found that the bubble size changed with changing the impeller speed. Also they conducted experiments on impellers with 3, 5, and 7 blades and found out that the bubble size decreased when the number of impeller increased. Kim et al. (1985) tested a radial pump used to pump two phase flow, liquid and gas, in the nuclear industry to better understand the behavior of the two phases inside the impeller. The pump was made out of acrylic to visualize the flow. The authors concluded that the main mechanism behind the pressure degradation at higher GVFs is the liquid phase acceleration. The authors claimed that when gas accumulated on the impeller blade, the liquid phase had to accelerate more to exit the impeller which reduced the pressure head, and hence causing more degradation.

In their research, Sato et al. (1996) performed experimental analysis on a centrifugal pump with a vane-less diffuser. The authors used a high speed video camera and a transparent shrouded impeller to observe the flow inside the pump. Again, they discovered that the gas pockets were formed on the pressure side of the impeller, and the gas pockets got larger when the GVF increased. They also observed that the size of the gas pocket directly affected the pump head degradation as when the gas accumulated on the impeller increased, the pump head decreased.

Andras (1997) performed an experimental study on an open type centrifugal pump using a high speed camera to visualize the flow inside the impeller and diffuser vanes for two phase flow. Andras found that the gas pocket started to form on the suction of the pump at the impeller intake. He also found that at higher GVF, the gas pocket got larger leading eventually to a gas lock in the whole pump. In the same year, Takemura et al. (1997) studied the flow in an axial flow centrifugal pump. The pump was designed to generate better mixing for the two phases, gas and liquid, by reducing the bubble size. The authors used transparent casing to visualize the flow, and they concluded that the gas accumulation on the impeller blade can be controlled by changing the blade load distribution.

In 2001, Suryawijaya (2001) performed an experimental analysis on a centrifugal pump that handled two phase flow. The pump's casing was transparent and the authors used the high speed camera to visualize the flow and measure the bubble size. Gas accumulation was detected on the pressure side of the impeller blade which agreed with the data from earlier researches. Moreover, the pressure was measured on the pump's impellers using sub miniature pressure transducers. The pressure on the blade depended on the amount of accumulated gas on the blade. When the GVF increased the size of the gas pocket on the impeller pressure side increased causing the pressure to drop and be non-uniformly distributed on the impeller blade.

Estevam (2002) used a downscaled radial pump with a transparent acrylic casing together with a high speed camera to visualize the two phase flow inside the pump impeller. Estevam observed gas accumulation on the pressure side of the impeller blade.

The author also observed a significant drop in the pump head when increasing the GVF as the accumulated gas pocket gets larger. In 2003, Poullikkas (2003) experimentally investigated the flow inside a nuclear reactor cooling pump using high speed camera. The author was trying to visualize the bubbles inside the impeller. The author observed that at low GVFs the gas accumulated near the intake of the impeller blade, while at high GVF, the gas accumulated on the whole blade and blocked the flow. Three years later, Thum et al. (2006) performed an experimental study on a centrifugal pump impeller to visualize the two-phase flow inside the pump. The authors observed that at higher GVF the separation increased in the pump leading to gas accumulation and total flow blockage.

In her research, Barrios (2007) studied the two phase flow in an ESP and used a high speed camera to visualize the flow in an impeller stage. The author was able to detect the gas accumulation on the pressure side of the impeller blades at high GVF. Also the author studied the factors that would cause surging in the pump. The bubble size played a very important role in the pressure head degradation of the pump.

Nowadays it is crucial for the oil and gas industry to understand how different types of ESPs perform under different two phase flow conditions. This is important as it directly impacts the production cost of oil and gas, and it allows the operator to choose the optimum operating point for an ESP system.

1.3 CFD based design

CFD has been a very powerful tool to simulate and understand the fluid dynamics in very complicated geometries and extreme operating conditions. Moreover CFD can perform analysis on fluid flows that could not be easily captured using experimental analysis tools. Recently with the availability of powerful computers that can handle complicated problems with several millions nodes in the computational domain, CFD analysis can be used to replace much experimentation. This is mainly due to the cost of running a simulation is much less than the cost of building a testing facility. Lately, many researchers have been utilizing CFD codes as a design tool that enabled them to change the design of their geometry, or the operating conditions, and run simulations in order to achieve the optimum design before investing in the manufacturing and testing of the product.

In their research, Tonomura et al. (2004) performed a CFD-based study to optimize the design of a manifold in micro devices. Their results showed that the longer branched channels were better in allowing a more uniform equally distributed fluid in all channels as shown in Fig. 6. However, the proposed method of CFD-based optimization required extensive computational time.

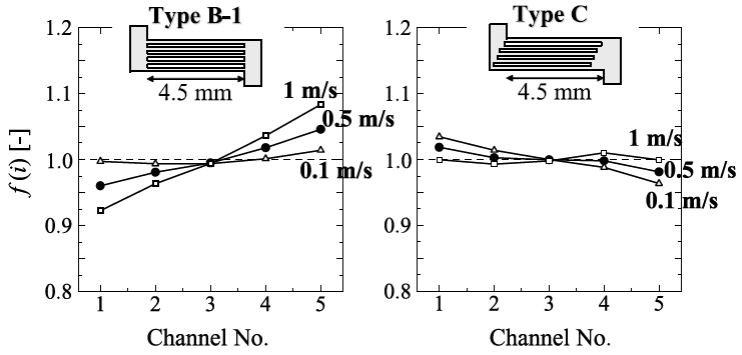

Figure 6. Flow comparison for different manifold designs (Tonomura, et al. 2004)

Hui-min et al. (2010) utilized CFD techniques to modify the design of an implanted axial flow blood pump. The authors were able to make the flow of the blood smoother and to reduce the rotor speed from 1200 to 1000 rpm with the new pump design as seen in Fig. 7. The new proposed design was proven to reduce the vortices and secondary flows. PIV experimental data were used to validate the CFD model and both experimental and theoretical results agreed.

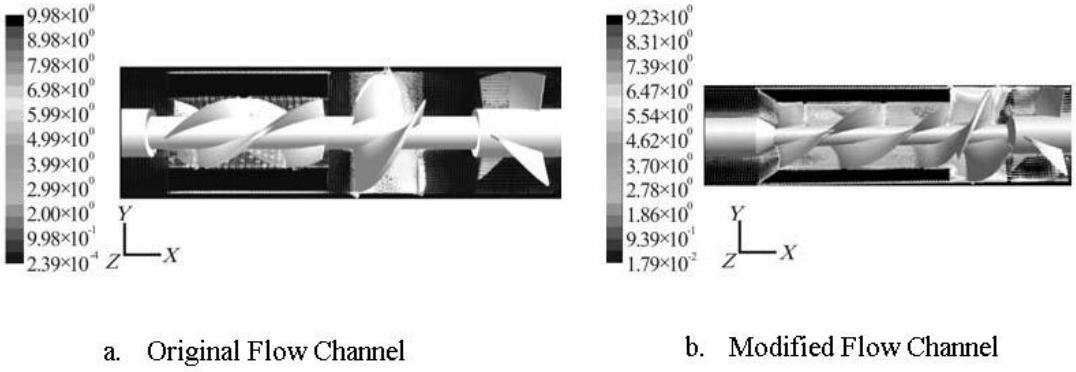

Figure 7. Flow velocity in different pump designs (Hui-min, et al. 2010)

Fan et al. (2011) used CFD as a tool to optimize the design of jet pumps. First the authors used an analytical approach to design the baseline configuration of the jet pump. Utilizing CFD, the authors were able to modify the pump design and increased the efficiency of the pump from 29% to 33%.

There are a limited number of projects that utilized CFD as a design and analysis tool for multiphase ESPs. Many of the studies only focused on the impeller, and almost none studied the diffuser and its effect on the ESP multistage efficiency. In this research a multistage MVP ESP will be studied both experimentally and theoretically using CFD. Different designs will be considered as well as a comprehensive analysis of the current design will be presented.

2. OBJECTIVES

While most of the previous works simulating ESPs are directed at understanding the flow behavior in a single stage of an impeller only, full 3D CFD simulations will be performed for single and multistage MVP ESP to understand the pump performance under different operating conditions and try to reach the optimum design and operating point.

The CFD model will be validated using experimental data including pressure head for the pump, power, and efficiency. A preliminary CFD simulation using K-epsilon RANS model can predict the pump performance accurately for both single phase and two phase flows. Also, the CFD model shows separation losses in the pump diffuser that affects the total pump efficiency. Modeling of a multistage MVP pump will be performed to investigate the effect of one stage on the next stage's performance. CFD analysis will be used to compare different diffuser designs to reduce the losses in the diffuser and improve the whole multistage pump efficiency.

Different multiphase inlet conditions will also be modeled and compared to determine how the pump performs with non-homogenous inlet boundary conditions. This will be helpful to understand whether the pump is capable of mixing gas and liquid effectively or not. Therefore, modeling the mixing chamber at the pump inlet is critical to understanding the pump behavior.

Once the CFD model is validated, it can be used to understand the reason behind the pressure degradation in the pump at higher GVF, and how this MVP design is better than the traditional ESP design.

With the validated CFD model, values of forces, pressure heads, and GVF distributions across the pump will be analyzed easily. These values are very difficult and expensive to be measured using experimental instrumentation. Moreover, the CFD model can be used to predict the pump performance for different viscosity fluids, and different types of gases at extreme conditions at much lower cost compared to experimental analysis.

3. PROCEDURES

The experimental testing facility, including the MVP multistage pump design that enables the flow visualization, and the computational and experimental test matrices are presented in this chapter. The MVP ESP consists of 3 stages consisting of a rotating shrouded impeller and a stationary shrouded diffuser per stage. This 3-stage pump is built to conduct the experimental program at the Turbomachinery Laboratory at Texas A&M University. Figure 8 shows the impeller hub and blades, and the diffuser hub and blades without showing the impeller and diffuser's shrouds.

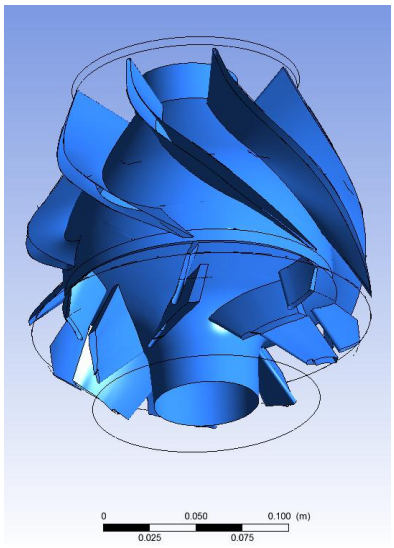

Figure 8. Single stage hub and blades

Experimental testing is conducted on the 3 stage pump, and the data are used to validate the CFD model that will be used to better understand the pump performance in different operating conditions.

3.1 Experimental testing

In this test program, Shell supplied the 3 Stage MVP ESP that is manufactured by Baker Hughes to be used to conduct the experimental testing in the Turbomachinery Laboratory. A team lead by another PhD student, Sahand Pirouzpanah, in the Turbomachinery Laboratory was responsible for the design and installation of the test rig. After helping them with building the system, they carried out the pump testing at different operating conditions. These data were used later to validate the CFD model presented in this research.

Figure 9 shows the 3 Stages pump before assembly. The pump is mounted vertically to simulate the actual operating conditions in a traditional production oil well.

Figure 9. 3-stages MVP ESP under investigation

The MVP pump under investigation has a window on the casing that allows for flow visualization through the second stage diffuser. The mixing chamber at the inlet of the pump is made of acrylic that allows for flow visualization at the pump inlet as well. Liquid and gas are supplied at the pump inlet mixing chamber at the bottom where the mixing takes place, the mixture is then pumped out from the top. The next two sections will present the testing facility and the data acquisition systems in more details.

3.1.1. Pump facility

Figure 10 shows the pump testing facility that can handle up to 400 psi pressure at the inlet of the pump. This is a closed loop testing facility that utilizes a cyclone separator tank to separate the liquid and gas phase after they are mixed in the MVP pump.

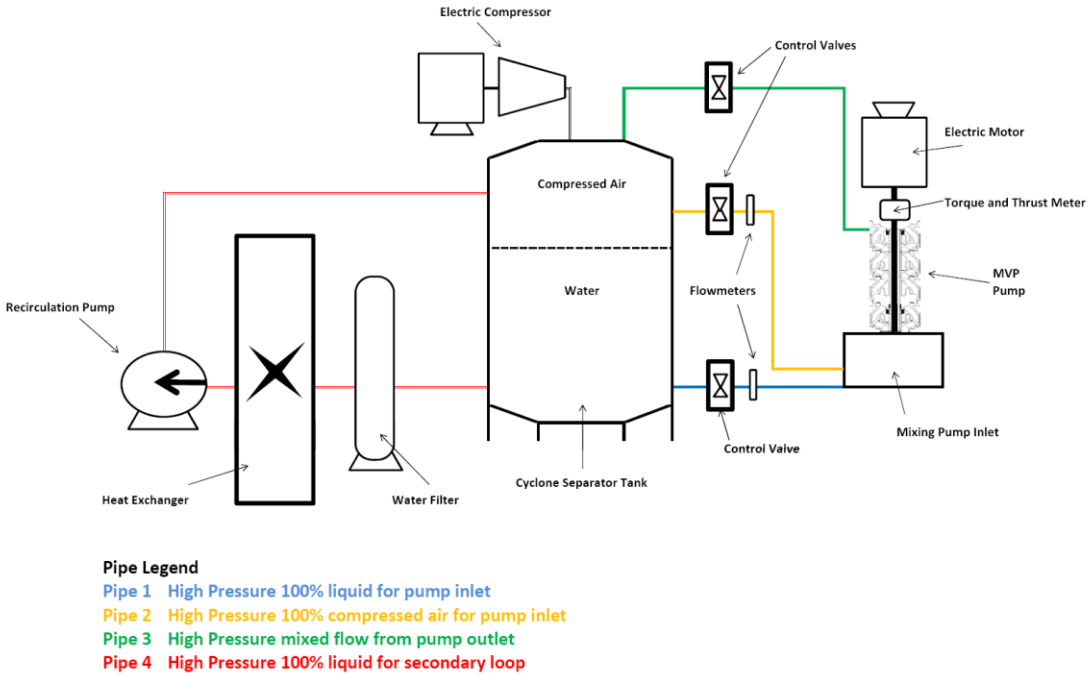

Figure 10. MVP pump testing facility

The whole test rig is pressurized using an electric air compressor that is connected to the top of the tank. After reaching the desired testing pressure, the MVP pump is started. The MVP is driven by a 250hp electric motor mounted vertically above the pump. Water is supplied to the pump inlet from the bottom of the separating tank while air is supplied to the pump inlet from the top of the tank. Mixing of the two phases takes place at the acrylic mixing chamber located at the pump inlet. The mixed flow exits the MVP pump from the top, and the mixture is pumped back to the tank that separates the two phases again. A secondary loop is shown on the left side of the schematic diagram (Fig. 10). A secondary centrifugal pump is used to circulate the water in the tank through a filter and a heat exchanger to control the temperature inside the test

rig. Both the recirculation pump and the MVP pump motors are controlled using Variable Frequency Drives (VFD). VFD is used with the MVP to control the pump rotating speed in order to examine the effect of the pump speed on the pump performance. VFD is also used with the recirculation pump to control the amount of fluid flowing into the heat exchanger, and hence control the temperature in the test rig.

The pump has two pipes at the inlet; a 6” pipe for water supply and a 2” pipe for air supply. The mixing chamber at the pump inlet has a 10” diameter. The pump has a total length of 33” and an outer casing diameter of 8”. To control the water flow rate, a pneumatic control valve is used in the water line, as seen in Fig.10, which uses the feedback signal of the water flow rate from the turbine meter. Pump inlet pressure is controlled using a pneumatic airline control valve. The GVF entering the pump is calculated and controlled using the pneumatic control valve on the outlet line.

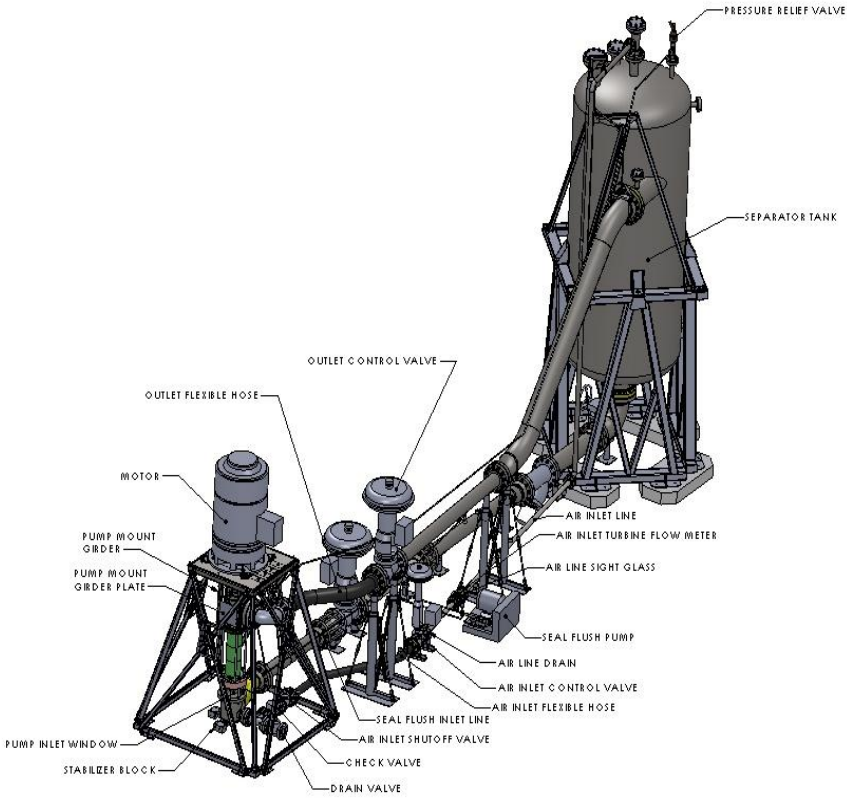

Figure 11. SolidWorks model for the test rig

Figure 12. Test rig for MVP ESP

Figure 13. MVP with instrumentation installed

Figure 11 shows the SolidWorks Model that is used to initially design the whole test rig while Figs. 12-13 show the actual test rig with after installation.

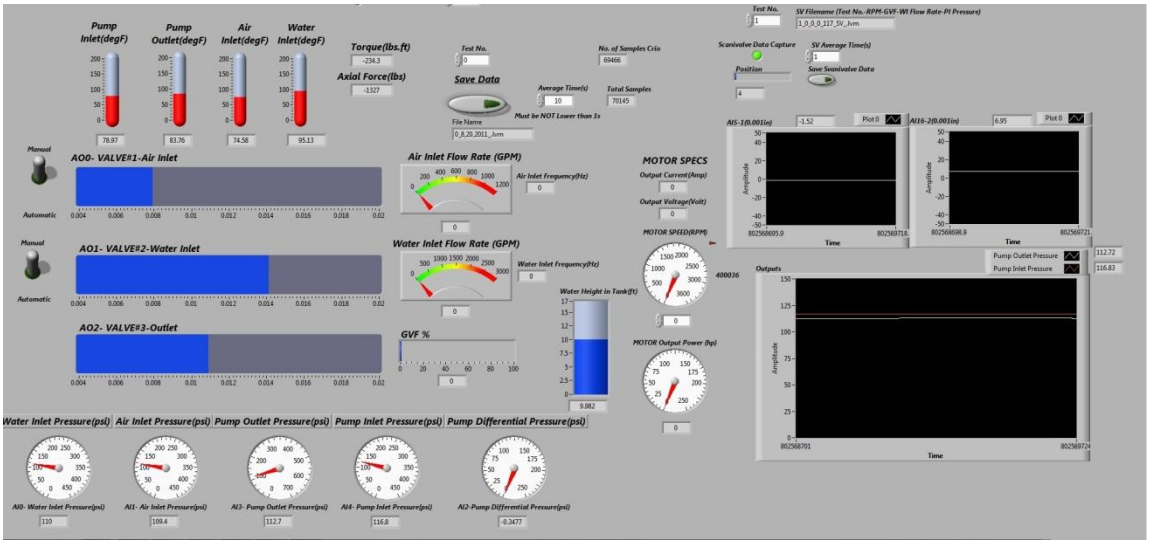

Figure 14. LabVIEW VI screenshot

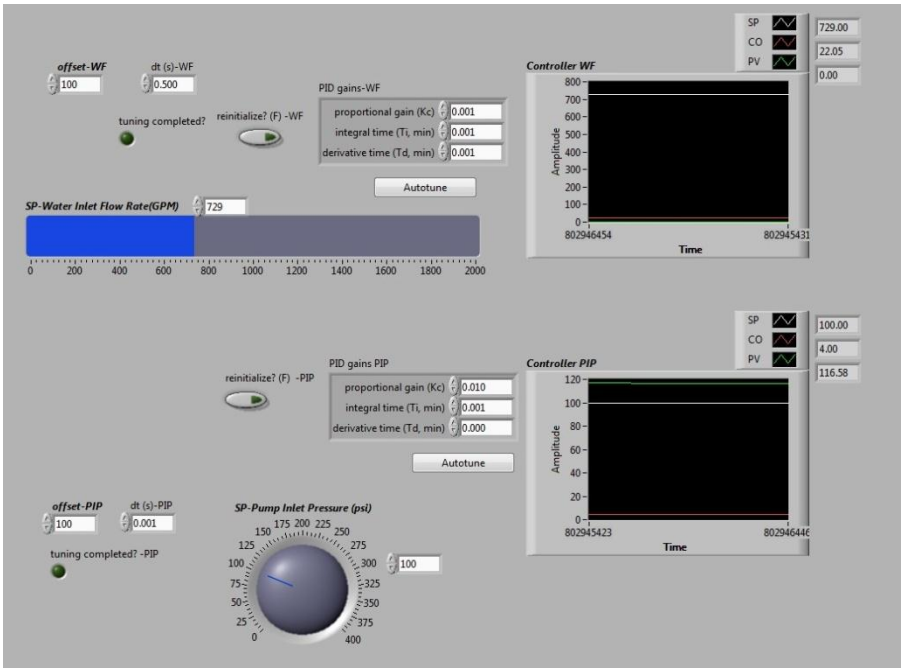

Figure 15. PID Controller in LabVIEW

All data from experimental testing are collected on a PC using National Instruments LabVIEW software. A Virtual Instrument (VI) is used to collect the data and control the process using built in PID controllers. Figure 14 shows the LabVIEW VI, while Fig. 15 shows the automatic PID controller with the auto-tune option that allows the software to compute the gains of the controller. In this work, the MVP pump is rotated at speeds ranging from 1800-3600 rpm. Flow rates in this pump ranges from 300-2000 Gallons per Minute (GPM), while the GVFs will range from 0 to 35%.

3.1.2. Data acquisition

The turbine meters shown above in the test loop (Fig.10) are used to measure the volumetric flow rates of water and air. Pressure is measured at the inlet and the exit of the 3-stage pump, and then divided by three to find the pressure head in each stage for single phase flow using incompressible fluid (water). There are other pressure taps on each stage of the MVP pump to measure the pressure increase in each stage separately to be able to compare it with the CFD model data. Electric Tomography is used at the inlet mixing chamber to measure the GVF of the flow, and also compare it with the calculated GVF. Thermocouples are used to measure the temperature of the flow before and after the MVP pump.

The main motor VFD is controlled using a remote control panel that shows the speed and the power consumed. The power consumed is used to calculate the pump efficiency. Torque and thrust are also measured using strain gages and wireless

transmitters mounted on the shaft. The set of transmitters and receivers together with the strain gages are supplied by Binsfeld Engineering. Proximity probes are used to monitor the shaft alignment with respect to the seal and also to monitor shaft vibrations. This is critical since large misalignment can destroy the pump exit seal.

Data are sampled at a frequency of 7kHz and averaged for pressure, temperature, and flowrates. LabView VI is also set to read data from the VFD output and record it with each test.

3.2 Computational analysis

Four computers are used to run the CFD simulations for the MVP pump. CFD simulation includes many geometries, and different operating conditions. Solidworks is used to prepare or edit the geometry that is then exported to Gambit 2.4.6 which is an ANSYS product. The mesh is then exported to Fluent 13.0 which is an ANSYS solver that is used for computational fluid dynamics.

The MVP mesh is created using 3D hexahedral elements that are proven to converge faster than 3D tetrahedral elements. Hexahedral elements also reduce the number of nodes for the same geometry significantly compared to the tetrahedral elements and can be adapted in Fluent as well.

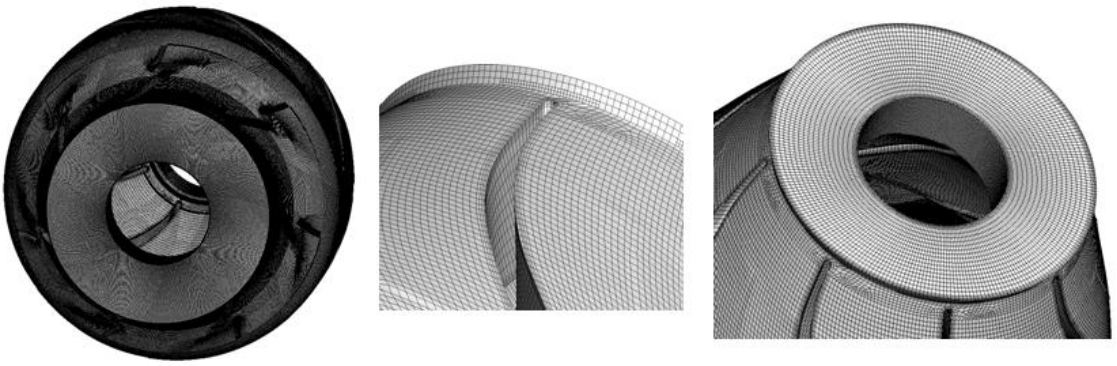

Figure 16. MVP mesh

Figure 16 shows different views of the mesh for the MVP pump. 95% of the mesh created for the pump is structured hexahedral while only 5% is unstructured hexahedral. The single stage MVP pump model is 4.3 million nodes before any adaption is carried out. A boundary layer mesh is created near all the walls using Gambit to keep the y* value within limits. The K-epsilon model is used to simulate the flow inside the MVP pump as it is well known of its ability to handle time transient turbomachinery problems with moving mesh or rotating reference frames. The K-epsilon model is a type of eddy viscosity models that is based on Reynolds Averaged Navier-Stokes equation (RANS) where the continuity and momentum equations are given as follows:

$$\frac{\partial \rho}{\partial t} + \frac{\partial}{\partial x_i}(\rho \overline{u_\iota}) = 0 \tag{1}$$

$$\frac{\partial}{\partial t}(\rho \overline{u_i}) + \frac{\partial}{\partial x_j}(\overline{u_i}\overline{u_j}) = -\frac{\partial \bar{p}}{\partial x_i} + \frac{\partial}{\partial x_j}\left[\mu\left(\frac{\partial u_i}{\partial x_j} + \frac{\partial u_j}{\partial x_i} - \frac{2}{3}\delta_{ij}\frac{\partial u_l}{\partial x_l}\right)\right] + \frac{\partial}{\partial x_j}(-\rho\overline{u_i'u_j'}) \tag{2}$$

The Reynolds shear stress term is related to the mean velocity gradient by the following equation:

$$-\rho\overline{u_i'u_j'} = \mu_t\left(\frac{\partial u_i}{\partial x_j}+\frac{\partial u_j}{\partial x_i}\right)-\frac{2}{3}\left(\rho k+\mu_t\frac{\partial u_k}{\partial x_k}\right)\delta_{ij} \quad (3)$$

The Standard K-epsilon model is given by the following formulas:

Transport equation for turbulent kinetic energy "k";

$$\frac{\partial}{\partial t}(\rho k)+\frac{\partial}{\partial x_i}(\rho k u_i)=\frac{\partial}{\partial x_j}\left[\left(\mu+\frac{\mu_t}{\sigma_k}\right)\frac{\partial k}{\partial x_j}\right]+P_k+P_b-\rho\varepsilon-Y_M+S_k \quad (4)$$

Transport equation for turbulent dissipation rate "ε";

$$\frac{\partial}{\partial t}(\rho\varepsilon)+\frac{\partial}{\partial x_i}(\rho\varepsilon u_i)=\frac{\partial}{\partial x_j}\left[\left(\mu+\frac{\mu_t}{\sigma_\varepsilon}\right)\frac{\partial\varepsilon}{\partial x_j}\right]+C_{1\varepsilon}\frac{\varepsilon}{k}(P_k+C_{3\varepsilon}P_b)-C_{2\varepsilon}\rho\frac{\varepsilon^2}{k}+S_\varepsilon \quad (5)$$

Turbulent viscosity is modeled as:

$$\mu_t = \rho C_\mu\frac{k^2}{\varepsilon} \quad (6)$$

$$P_k = \mu_t S^2 \quad (7)$$

Where S is the modulus of the mean rate of strain tensor and given by:

$$S = \sqrt{2\,S_{ij}S_{ij}} \quad (8)$$

$$P_b = \beta g_i\frac{\mu_t}{P_{rt}}\frac{\partial T}{\partial x_i} \quad (9)$$

Where P_{rt} is the Prandtl number for energy, and g_i is the gravity, and for realizable models, the default value of $P_{rt} = 0.85$, and β is the coefficient of thermal expansion given by:

$$\beta = -\frac{1}{\rho}\left(\frac{\partial\rho}{\partial T}\right)_p \quad (10)$$

The model constants are given as follows:

$$C_{1\varepsilon} = 1.44 \quad (11)$$

$$C_{2\varepsilon} = 1.92 \tag{12}$$

$$C_{\mu} = 0.09 \tag{13}$$

$$\sigma_k = 1.0 \tag{14}$$

$$\sigma_{\varepsilon} = 1.3 \tag{15}$$

According to Fluent Theory Guide (2009), the standard wall function is implemented in the CFD simulations as it is widely used in the industrial problems. The governing momentum equation of the mean velocity law of the wall is given by:

$$U^* = \frac{1}{\kappa} \ln(Ey^*) \equiv \frac{U_p C_{\mu}^{1/4} K_p^{1/2}}{\tau_{\omega}/\rho} \tag{16}$$

Where, κ is the Von Karman constant (=0.4187), and E is an empirical constant (=9.793), and the logarithmic law is valid for $30 < y^* < 300$

The y* value is the dimensionless velocity near wall and is given by:

$$y^* = \frac{\rho C_{\mu}^{1/4} k_p^{1/2} y_p}{\mu} \tag{17}$$

Where k_p is the turbulent kinetic energy at the near-wall node p,

And y_p is the distance from point p to the wall

A Reynold's analogy between the momentum and energy transport equation leads to a similar temperature logarithmic law as follows:

$$T^* = \frac{(T_\omega - T_p)\rho C_\mu^{1/4} k_p^{1/2} c_p}{\dot{q}} =$$

$$\begin{cases} P_r y^* + \frac{1}{2}\rho P_r \frac{C_\mu^{1/4} k_p^{1/2}}{\dot{q}} U_p^2 & (y^* < y_t^*) \\ P_{rt}\left[\frac{1}{\kappa}\ln(E y^*) + P\right] + \frac{1}{2}\rho \frac{C_\mu^{1/4} k_p^{1/2}}{\dot{q}}\left\{P_{rt} U_p^2 + (P_r - P_{rt}) U_c^2\right\} & (y^* > y_t^*) \end{cases} \quad (18)$$

The wall is assumed to be smooth with surface roughness coefficient equal to zero.

3.2.1. Single phase simulations

The MVP is a 7-blade impeller and 8-blade diffuser to prevent shocks in the flow while the pump is running. Therefore, modeling one impeller blade and one diffuser blade using periodic boundary conditions is only applicable when modeling steady state flow. In order to run a transient simulation of the pump, the whole pump must be meshed and modeled and the use of periodic boundary conditions becomes inappropriate.

The liquid used to test and simulate the MVP pump is water. Single phase flow is simulated for different pump operating conditions. The MVP is simulated using both steady state and transient CFD simulations. When using a steady state CFD simulation, which is less accurate than the transient simulation, the geometry has to be constant and no moving mesh can be simulated which may result in an inaccurate prediction of the

flow. Rotating machinery is proven to be better simulated using moving mesh rather than rotating reference frames.

A single stage is modeled using mass flow inlet at the impeller inlet and pressure outlet as the outlet of the diffuser. Different flowrates and pump speeds are modeled ranging from 583 to 1200 GPM and from 3300 to 3600 rpm respectively.

The effect of the pump inlet on the pump efficiency is also studied by simulating the pump inlet and the 3 stages all together. Primary data show that separation in the flow at the outlet of one pump stage may affect the efficiency of the following stage.

Transient simulations are compared to experimental data, and are also used to examine the flow more closely in the pump to better understand the type and places of the losses.

3.2.2. Two phase simulations

Two phase flow simulations are carried out for the MVP pump using different techniques and operating conditions. The working fluids for the two phase flow are air and water. The MVP ESP is designed to create better mixing for the two phases, liquid and gas. The patented impeller is designed to provide better mixing in the flow and make it more homogenous. To simulate the current test cell setup, the pump inlet mixing chamber has to be simulated with the two separate inlet pipes; air inlet and water inlet.

Two designs were considered in the early design stage of the test cell, a design with a perforated tube for air, and another design without the air perforated tube. Figure 17 shows the fluid domain of the first design that can provide better mixing for the two phases before entering the pump, while Fig. 18 shows the fluid domain of the second design that would provide less mixing for the two phases.

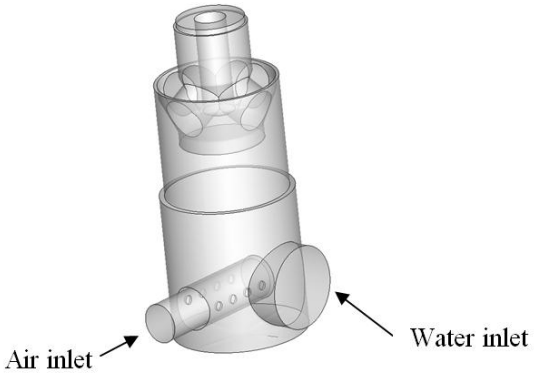

Figure 17. Fluid domain design 1 with perforated tube for air inlet

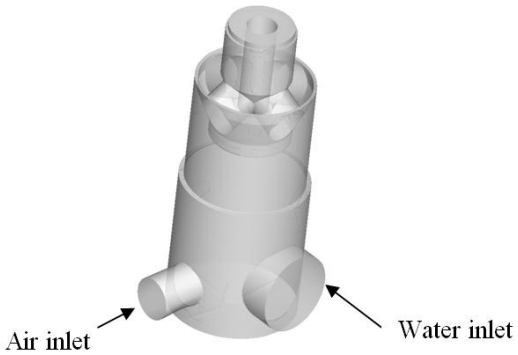

Figure 18. Fluid domain design 2 without perforated tube for air inlet

Preliminary results shows that the second design; as seen in Fig.18, provides non homogenous mixture of the two phase flow at the pump inlet that will be helpful to show if the pump can provide good mixing of the two phases or not.

Transient analysis of the two phase flow inside the pump has to be carried out with moving mesh to show how each phase of the flow behaves inside the pump impeller and diffuser. Steady state analysis will lead to wrong results and can not predict the pump behavior under non-homogenous mixture at the pump inlet.

The pump is also simulated with homogenous mixture boundary condition of the two phases at the inlet to compare the effect of different flow rates, and different GVFs on the pump efficiency and behavior. Applying homogenous boundary conditions at the pump inlet has to be simulated transiently with moving mesh technique to accurately predict the pump performance. The CFD model used is a realizable K-epsilon model with the energy equation on and fixed temperature using compressible ideal gas for air, and incompressible liquid for water. The realizable K-epsilon model is given by the following equations:

Transport equation for realizable turbulent kinetic energy "k";

$$\frac{\partial}{\partial t}(\rho k) + \frac{\partial}{\partial x_j}(\rho k u_j) = \frac{\partial}{\partial x_j}\left[\left(\mu + \frac{\mu_t}{\sigma_k}\right)\frac{\partial k}{\partial x_j}\right] + P_k + P_b - \rho\varepsilon - Y_M + S_k \quad (19)$$

Transport equation for realizable turbulent dissipation rate "ε";

$$\frac{\partial}{\partial t}(\rho \varepsilon) + \frac{\partial}{\partial x_j}(\rho \varepsilon u_j) = \frac{\partial}{\partial x_j}\left[\left(\mu + \frac{\mu_t}{\sigma_\varepsilon}\right)\frac{\partial \varepsilon}{\partial x_j}\right] + \rho C_1 S_\varepsilon - \rho C_2 \frac{\varepsilon^2}{k+\sqrt{\nu\varepsilon}} + C_{1\varepsilon}\frac{\varepsilon}{k} C_{3\varepsilon} P_b + S_\varepsilon \quad (20)$$

Where,

$$C_1 = max\left[0.43, \frac{\eta}{\eta+5}\right],\ \eta = S\frac{k}{\varepsilon},\ S = \sqrt{2\,S_{ij}S_{ij}} \tag{21}$$

$$C_{1\varepsilon} = 1.44 \tag{22}$$

$$C_2 = 1.9 \tag{23}$$

$$\sigma_k = 1.0 \tag{24}$$

$$\sigma_\varepsilon = 1.2 \tag{25}$$

The Euler-Euler Model proposed by Fluent is the most generic multi-phase model as it includes a set of governing equations for each phase separately and this accounts for the slip velocity between the two phases. Other models used in Fluent such as Volume Of Fluid (VOF), has only one set of equations for the mixture and does not account for the slip velocity. For the Euler-Euler Model used, consider the two phases; p & q, the continuity equation for each phase is given by:

$$\frac{1}{\rho_{yq}}\left(\frac{\partial}{\partial t}\left(a_q\rho_q\right) + \nabla.\left(a_q\rho_q\bar{v}_q\right) = \sum_{p=1}^{n}(\dot{m}_{pq} - \dot{m}_{qp})\right) \tag{26}$$

Where ρ_{yq} is the phase reference density of the phase q

The volume fraction V_q of phase q is given by:

$$V_q = \int_V a_q\, dV \tag{27}$$

Where a_q is the phasic volume fraction as $\sum_{q=1}^{n}\left(a_q\right) = 1$

Hence, the effective density of the phase q is:

$$\hat{\rho}_q = a_q\rho_q \tag{28}$$

The Fluid-Fluid conservation of momentum for the fluid phase q is given by:

$$\frac{\partial}{\partial t}\left(a_q \rho_q \bar{v}_q\right) + \nabla.\left(a_q \rho_q \bar{v}_q \bar{v}_q\right) = -a_q \nabla p + \nabla.\bar{\tau}_q + a_q \rho_q \vec{g} + \sum_{p=1}^{n}(K_{pq}\left(V_p - V_q\right) + \dot{m}_{pq}\bar{v}_{pq} - \dot{m}_{qp}\bar{v}_{qp}) + \left(\vec{F}_q + \vec{F}_{lift,q} + \vec{F}_{vm,q}\right) \quad (29)$$

Where F is the force vector, and $\bar{\tau}$ is the stress-strain tensor

The conservation of energy is shown below through separate enthalpy equation for each phase and is written as:

$$\frac{\partial}{\partial t}\left(a_q \rho_q h_q\right) + \nabla.\left(a_q \rho_q \bar{u}_q h_q\right) = a_q \frac{\partial \rho_q}{\partial t} + \bar{\tau}_q . \nabla \bar{u}_q - \nabla.\bar{q}_q + S_q + \sum_{p=1}^{n}(Q_{pq} + \dot{m}_{pq}h_{pq} - \dot{m}_{qp}h_{qp}) \quad (30)$$

Where, h is the specific enthalpy, $\bar{q}$ is the heat flux, S_q is the source term that includes the source enthalpy, and Q_{pq} is the intensity of the heat exchange between the two phases. The exchange coefficient between the two phases is given by K_{pq} as follows:

$$K_{pq} = \frac{a_q a_p \rho_p f}{\tau_p} \quad (31)$$

Where f is the drag function that includes the drag coefficient, and τ_p is the particulate relaxation time and is given by the following equation:

$$\tau_p = \frac{\rho_p d_p^2}{18\mu_q} \quad (32)$$

And d_p is the bubble diameter.

CFD simulation test matrix includes liquid flowrates that range from 438 to 1000 GPM, and GVFs that range from 5 to 35% and two different inlet pressures; 400 and 950psi to simulate testing at both the Turbomachinery Laboratory facility that can handle the 400psi testing, and Shell testing facilities that can handle the 950psi testing.

3.2.3. CFD based design

According to Hui-min et al. (2010), CFD can be used to improve existing designs. Hui-min et al. were able to improve a blood pump design by changing the diffuser blade design. Moreover the authors were able to reduce the pump speed and attain the same pump performance.

In this work, the MVP pump impeller and diffuser are simulated, and flow is studied inside the diffuser for both single and two phase flows for the first time. Primary studies show that there are considerable amount of losses in the diffuser due to flow separation. Not only does this phenomenon affect the pump stage efficiency due to the separation losses in the diffuser, but it also reduces the next stage's pumping efficiency as the flow velocity exiting one stage's diffuser and entering the next stage impeller is not uniform. Therefore, a study is conducted to examine how different diffuser designs would improve the multistage pump performance in the MVP ESP.

This study is mainly applied to single phase flows using water as the working fluid. Since single phase flow takes less computational time and memory, it is more convenient to use it for comparison between different diffuser designs.

4. RESULTS AND DISCUSSION

This chapter presents both experimental and CFD simulations results for the MVP pump. The first section of this chapter presents the pump performance for single phase flow. In the second section, the two phase model of the pump is presented and compared to the experimental test results, and the third section presents the utilization of CFD analysis to reach a better pump design and improve the pump performance.

4.1. Single phase CFD simulation and experimental testing

This section is divided into three parts; firstly the model validation for single phase is presented. Secondly the effect of one stage on the next stage's performance is simulated and finally the model of the full pump including the pump's three stages with the inlet chamber is studied.

4.1.1. Single phase model validation for single stage

The MVP G470 pump was tested in the Turbomachinery Laboratory test facility for single phase flow using water as the working fluid. The test is controlled using Labview code and the performance data is recorded for different operating conditions.

Figure 19 shows the performance curves for a single stage of the MVP pump for two different speeds; 3300 and 3600 rpm obtained experimentally.

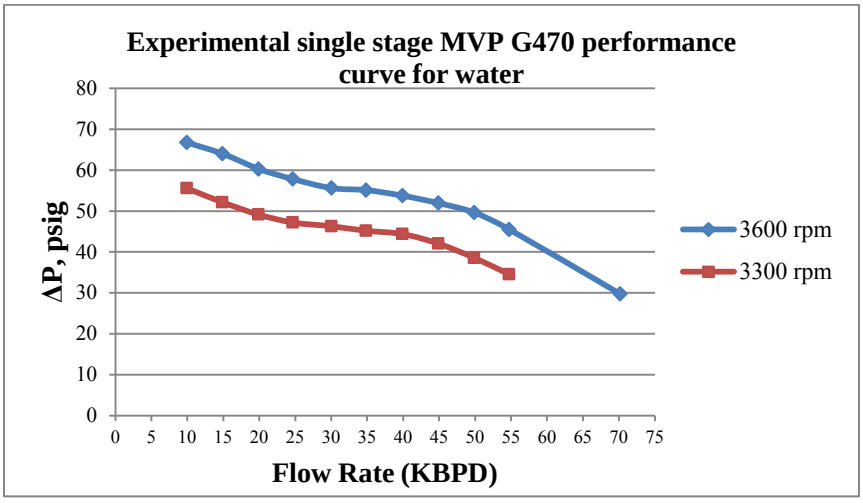

Figure 19. Experimental MVP G470 average single stage performance curves for 3300 and 3600 rpm

The data shown in Fig. 19 are based on the differential pressure measurements across the three stages, then these values were divided by three to obtain the pump head for a single stage. The unit for flow rate shown above is in Barrels per Day (BPD) which is equal to 34.2 US gallons per minutes (gpm).

Gambit was used to create the mesh for the MVP pump. The first attempt to simulate the pump was based on an axisymmetric assumption. However to reduce hydrodynamic forces, the pump was designed with 7 blades on the impeller and 8 blades on the diffuser. The difference in the number of blades of both the impeller and diffuser complicated the axisymmetric simulation. With that setup, the pump can only be simulated with steady state conditions. One blade of the impeller and one blade of the

diffuser were meshed using the polyhedral elements presented in ANSYS. The interface between the impeller fluid part and the diffuser fluid part was chosen to be mixing planes. When mixing planes are used, the two interfaces don't have to have the same area. The boundary condition of one interface is a pressure outlet and the boundary condition of the second interface is a pressure inlet, and this assumption is valid only for steady state problems as seen in Fig. 20.

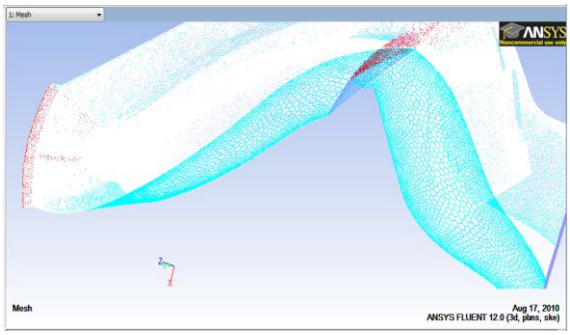

Figure 20. Single impeller blade and single diffuser blade steady state mesh

The mesh near the boundary was chosen to be small to allow for a small y* value for a standard wall function. The moving reference frame condition was applied to the impeller fluid to simulate the impeller rotation and the case was solved for the steady state condition. The flow rate was 1300 gpm which corresponded to the highest pump efficiency point for single phase flow at 3600 rpm. The axisymmetric simulation under estimated the pump performance by 10%. Moreover since the moving reference frame technique was used, the simulation did not capture the interaction between the impeller

blades and the diffuser blades due to the impeller rotation. Therefore, in order to have a more accurate simulation, a transient analysis had to be considered.

The transient analysis requires a better boundary condition than the mixing planes to handle the interface between the impeller fluid and the diffuser fluid. A more accurate boundary condition for interfaces known as sliding mesh is presented in Fluent that can simulate transient problems. Sliding mesh interpolates the conditions between nodes on one interface to provide an estimate of the conditions at the exact node location of the corresponding interface. In order to use sliding mesh at an interface between two faces, the two faces must have the same area. Since the impeller and diffuser do not have the same number of blades, the whole pump had to be meshed and simulated for transient analysis as seen in Fig. 16.

To simulate the pump transiently, a mesh was created using Gambit for the whole pump using 100% hexahedral elements where more than 90% of the volume was structured hexahedral elements and the rest was unstructured hexahedral elements. A thin boundary layer was created near the wall to ensure a low y* value near the wall as seen in Fig. 16. The model had 4.2 million nodes. The mesh was then adapted to keep the y* value within limit (y*<300). The mesh was refined based on the y* value and a grid independence study was performed to choose an optimum number of nodes.

Table 1. Model size for different y* values

	Model 1	**Model 2**	**Model 3**	**Model 4**
y* value	<560	<300	<220	<120
No. of Nodes	4,258,499	4,640,230	5,110,268	8,496,726

Table 1 shows the number of nodes for different models with different y* values. Also different parameters were used to compare models with different mesh sizes to ensure grid size independence for the full pump. Pump pressure head, torque on the impeller, and the pump axial thrust for a single stage were used as parameters to check for grid independence as seen in Figs. 21-23. In these figures, the pump pressure head, torque on impeller blades, and the pump axial thrust were compared to the results of the model with the largest number of nodes (8,496,726 nodes), and the difference is given as a percentage from this value.

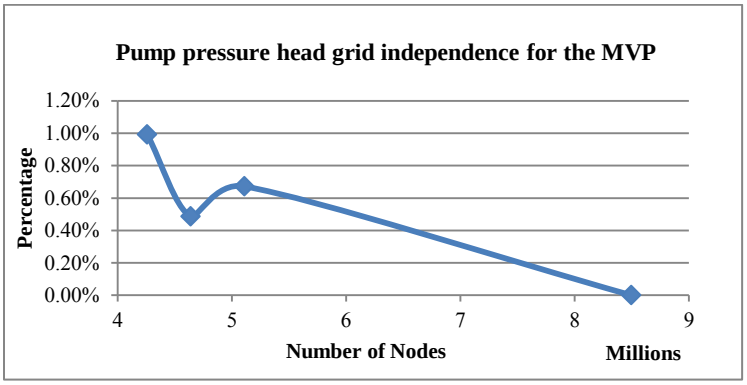

Figure 21. Pump pressure head grid independence for the MVP

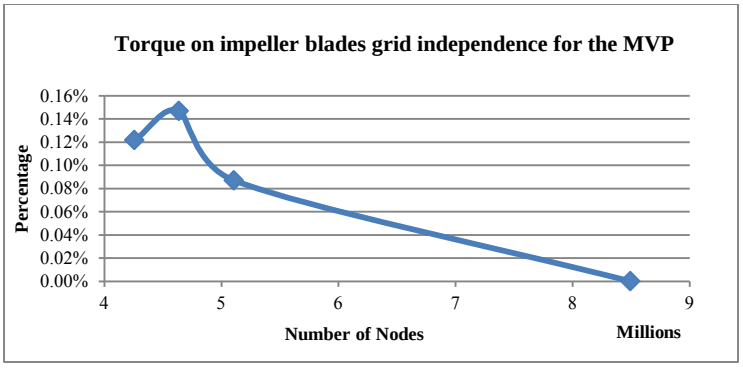

Figure 22. Torque on the impeller blades grid independence for the MVP

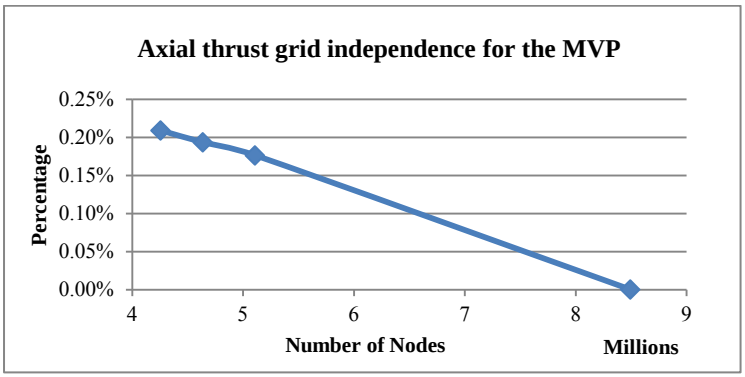

Figure 23. Axial thrust grid independence for the MVP

Model 2 presented in table 1 was chosen to simulate the pump as it has the y* value within the required range. According to the grid independence study, model 2 with the 4.6 million nodes had a maximum difference of 0.49% in pressure head, compared to model 4 that had 8 million nodes. The full pump was simulated with water as the working fluid and the pump pressure head was computed and compared to the experimental data shown in Fig. 19.

Moving reference frame was first used to simulate the impeller rotation. The full pump simulation was more accurate than the axisymmetric simulation but still the model was under predicting the pump pressure head by 5%. Moving mesh was then applied instead of moving reference frame and it gave a better estimate for the pump performance compared to the experimental results. Figure 24 shows the theoretical and experimental results of single phase flow inside a single stage of the MVP pump.

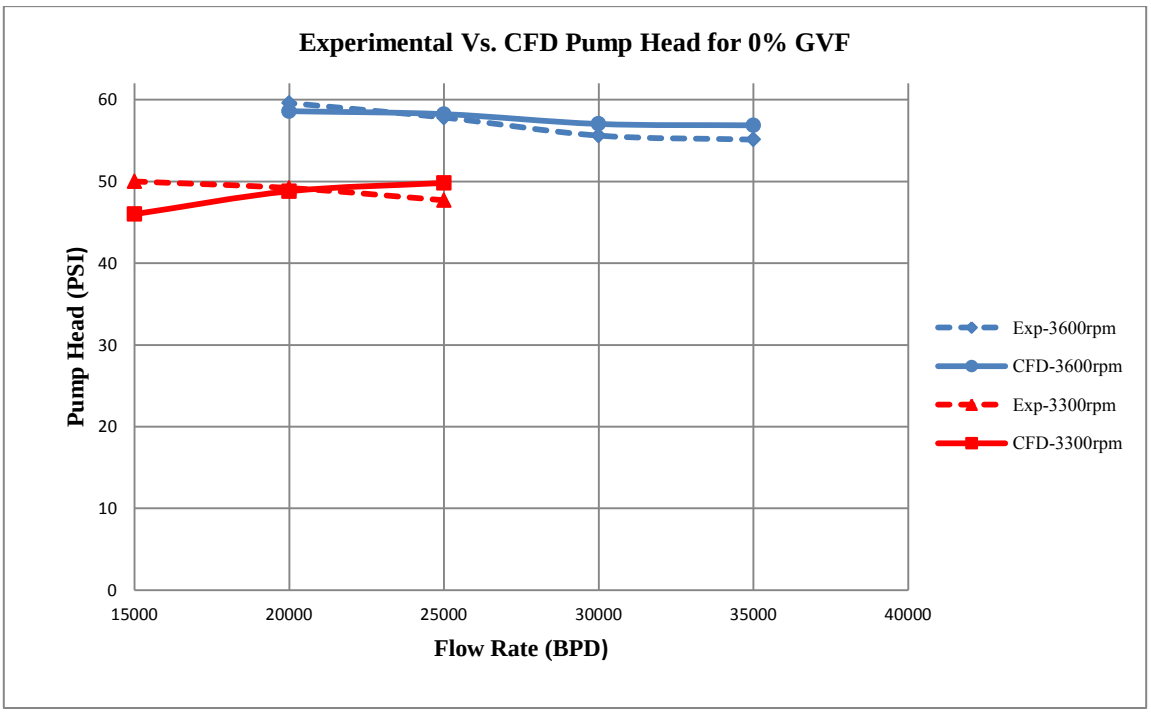

Figure 24. Experimental vs. theoretical pressure head for single stage of MVP pump

The theoretical and experimental results shown in Fig. 24 strongly agree with each other. However, the leakage and the balancing holes of the impeller were not modeled since the pump manufacturer would not supply this information. A study was

carried out to understand the effect of the diffuser on the next impeller performance. More results of the single phase simulation for water at different speeds and flow rates is shown in Appendix A.

4.1.2. Effect of one stage on the next impeller performance

A single impeller with no diffuser was simulated transiently as seen in Fig. 25, and the pressure was monitored until it became constant. The results were compared with a single impeller after a whole stage as seen in Fig. 26. The cases were run transiently for 2 full rotation rotations using 1 degree per time step. After two full rotations, the flow reaches a steady state condition, and the results become more accurate.

The impeller performance with and without the diffuser was monitored using two measures; static pressure head, and total pressure head across the impeller. The boundary conditions used for this case were mass flow rate at the inlet (35 KBPD) and pressure outlet at the outlet. Table 2 shows the comparison of the impeller performance with and without the previous stage. The results show that the irregularity of the flow from the previous stage causes the static pressure to be less by 2% and the total pressure to be less by 8.6%. The flow at the outlet of the diffuser is studied in more details in the last section of the results that shows that there is a flow separation in the diffuser causing strong vortices at the outlet of the diffuser.

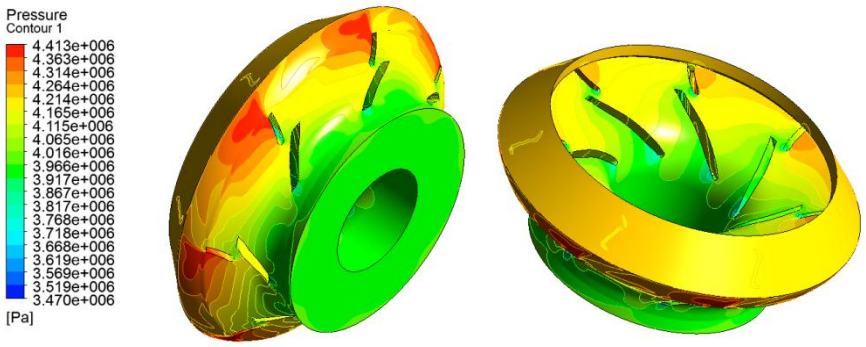

Figure 25. Static pressure for single stage impeller alone at 35 KBPD

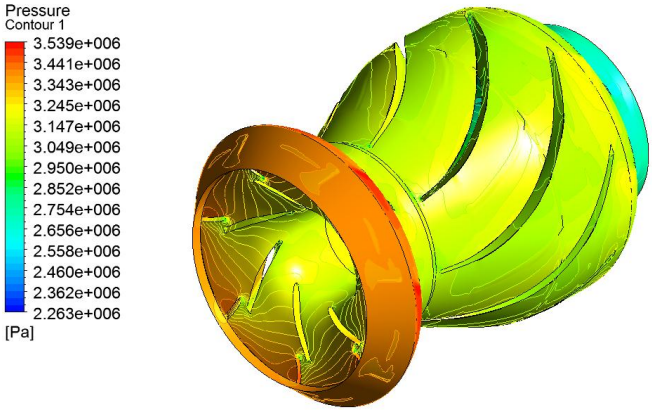

Figure 26. Static pressure for single stage impeller after a full MVP stage at 35 KBPD

Table 2. Comparison of a single impeller performance with and without the previous stage

Case	**Static Pressure (psi)**	**Total Pressure (psi)**
Single impeller alone	40.9	57.8
Single impeller after a full stage	40.06	53.19

4.1.3. Modeling and validation of 3 stages and the inlet mixing chamber

Three stages with the inlet were also modeled to study the effect of multiple stages on each other. The inlet was meshed with 100% hexahedral elements. More than 90% by volume was structured hexahedral mesh, and the rest was unstructured hexahedral. The mesh volume for the inlet was 5 million nodes. Figure 27 shows the mesh for the pump inlet with the smaller pipe at the bottom used as the gas inlet in case of the two phase flow, but it is used as a wall for the case of the single phase flow, while the bigger pipe at the bottom is used as the liquid inlet.

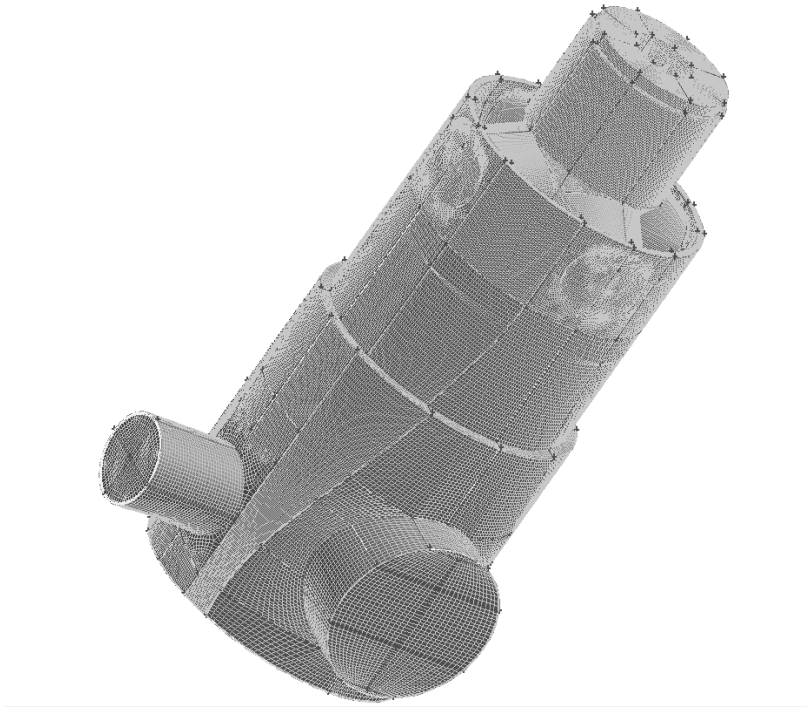

Figure 27. Pump inlet mixing chamber mesh

Figures 28-29 show the pressure contours and the streamlines for the 45 KBPD case respectively. Figure 30 shows the meridional plane contour plot for the static pressure for the 3 stages together, while Fig. 31 shows the pressure increase along the whole 3 stages. It shows a small drop at the end of each diffuser which is due to the flow separation as shown in Fig. 32.

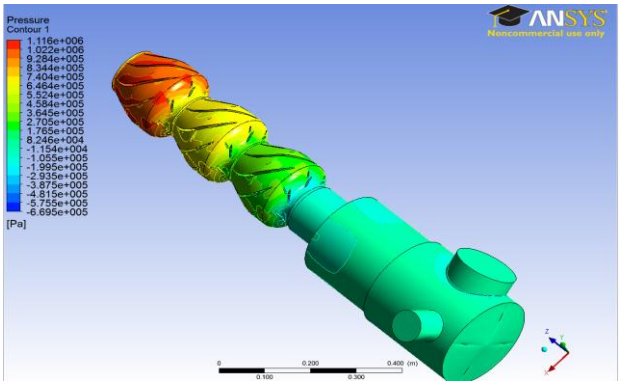

Figure 28. Static pressure contour plot for the inlet and the 3 stages at 45 KBPD

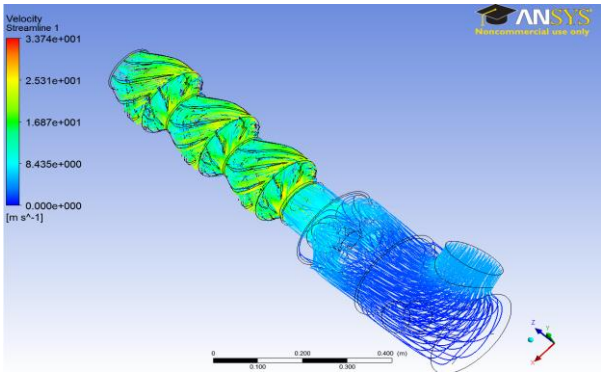

Figure 29. Streamlines for the inlet and the 3 stages at 45 KBPD

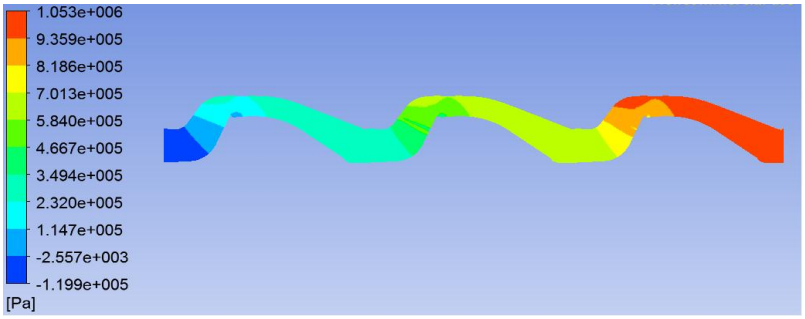

Figure 30. Static pressure in the meridional plane for the inlet and the 3 stages at 45 KBPD

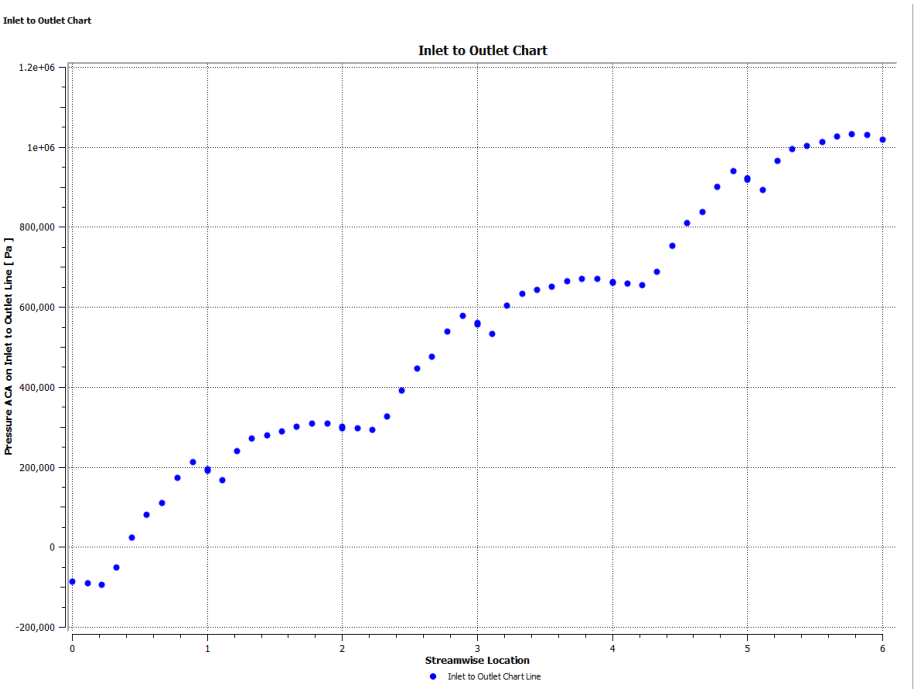

Figure 31. Static pressure across the three stages at 45 KBPD

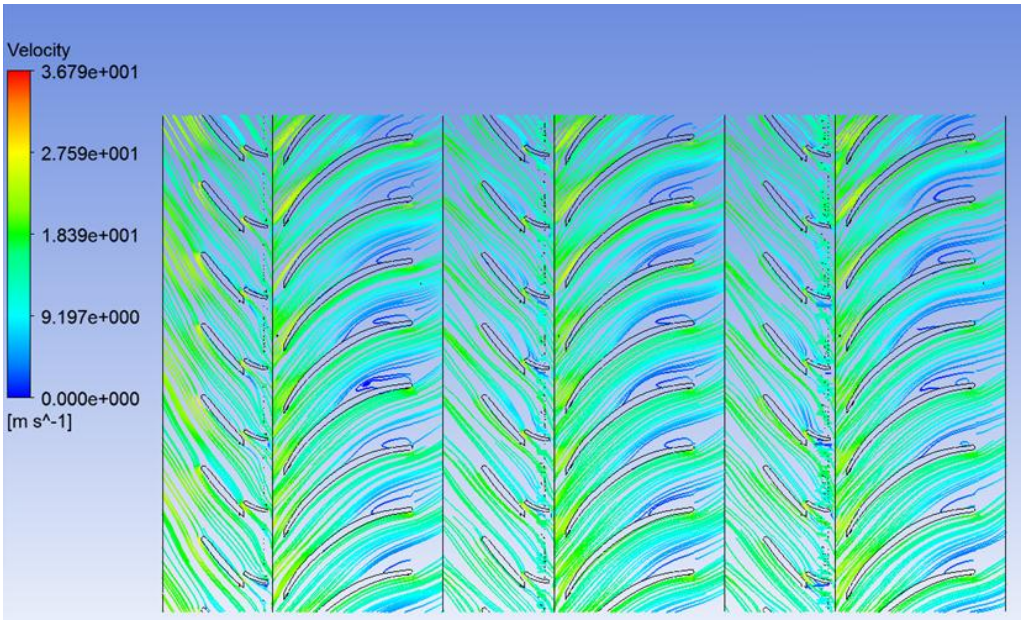

Figure 32. Stream lines of the 3 stages at 45 KBPD at the middle plane

Table 3. CFD predicted total pressure increase in the 3 stages and the mixing chamber assembly at 45 KBPD

Pump Stage	Total Pressure Head (psi)
Stage 1	53.1
Stage 2	49
Stage 3	49.3
Three stages theoretical	151.4
Three stages experimental	155.7

Table 3 presents the CFD predicted pump static pressure across each stage in the assembly and compares the theoretical and experimental results for the whole 3 stages.

This shows that there is an effect of one stage on the next stage's performance. Figure 32 shows that the flow separation in one stage causes the flow to have irregular velocity when it enters the next stage impeller. This phenomenon reduces the next impeller's efficiency. A quantitative analysis is presented in the third section of this chapter to better understand the losses in the diffuser.

4.2. Two Phase CFD simulation and experimental testing

Two phase CFD simulation and experimental validation are presented in this section. CFD simulation was carried out for three different inlet pressures; 200, 400, and 950 psi. The experimental facility at the Turbomachinery Laboratory for the MVP pump can handle up to 300 psi inlet pressure. The higher pressure was included to compare the results obtained by Shell Oil in their "Gasmer" facility. The pump mixing chamber and the first stage were simulated at 400 psi to understand the behavior of the two phases throughout the MVP pump. The objective was to verify the pump's ability to provide better mixing for the two phases. Since the data from the test rig were available at 200 psi, two cases with the whole three stages were simulated and compared to the experimental data to validate the model. Finally, 950 psi pressure inlet was simulated in order to predict the pump behavior at high pressures.

4.2.1. Mixing chamber and the first stage for 400 psi inlet pressure

One of the main functions of the MVP G470 pump is to mix the two phases of the flow; the liquid and the gas, as well as increasing the pressure head of the flow. When the flow becomes homogeneous, traditional ESPs can be used to provide pressure boosting to the flow without the gas locking takes place. Therefore, two designs for the mixing chambers were considered as seen in Figs. 17 and 18. The difference between the two designs is shown in Fig. 33. In design 1, the air is introduced inside the mixing chamber through a perforated tube that has eight holes. This design allows the air to be more uniformly distributed and creates a more homogenous two phase flow. However, in design 2, the air is directly introduced through the 2 inch pipe in the bottom. Therefore, as seen in Fig. 33, design 1 creates a more homogenous two phase flow at the MVP pump inlet compared to the flow in design 2.

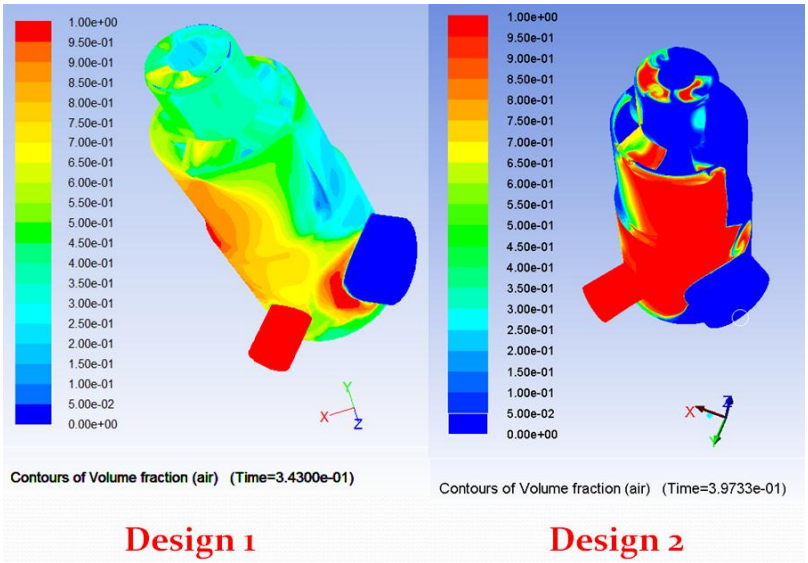

Figure 33. GVF contour plot for different mixing chambers

The results show that design 1 provides good mixing of the two phases while design 2 does not mix the two phases, therefore design 2 was chosen to test the pump at extreme conditions where the two phases are not premixed. Design 2 was tested and simulated. The CFD simulation showed that the MVP first stage is able to mix the flow as seen below in Fig. 34.

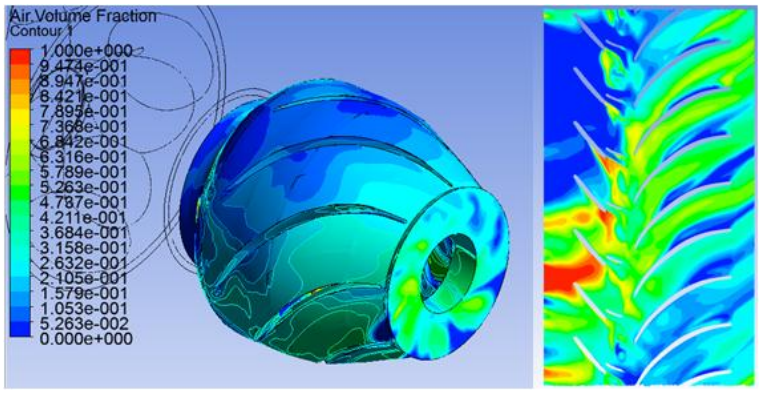

Figure 34. Contour plot of the GVF distribution at the first stage of the MVP at 32% GVF inlet pressure

As seen in Fig. 34, the two phase flow at pump inlet is not homogenous. It shows blue parts with 100% water and red parts with 100% gas. At 3600 rpm, and 25 KBPD flow rate, the average tangential velocity of the fluid inside the impeller is approximately 3.5 times the axial velocity of the flow. This difference in velocity allows the impeller to provide a homogenous distribution of the two phases inside the diffuser. Figures B1 and B2, in appendix B, show the GVF distribution at the pump inlet, outlet and the impeller/diffuser interface. Also Fig. B3 shows how the pressure distribution against the GVF distribution and the streamlines at the pump middle plane. The streamlines plot shows the separation taking place in the diffuser at the blade pressure side. This separation causes local vortices to take place and the resulting axial velocity of the flow at these vortices is almost zero. Therefore, there is a delay in the GVF distribution at the diffuser blade pressure side due to the vortices.

The boundary conditions applied for the case shown above are 100% mass flow rate of ideal gas air at the air inlet, 100% mass flow rate of water at the water inlet, and pressure outlet at the outlet of the pump. The water flow rate is 30 KBPD with 32% GVF at the pump inlet and the pump speed is 3600 rpm. Since the flow is not homogenous at the inlet of the pump as seen in Fig. 34, a moving mesh must be used to simulate the flow inside the rotating impeller and its interaction with the stationary diffuser. Fluent offers three different multiphase models; mixture model, Volume Of Fluid (VOF), and Euler-Euler model. The VOF model is applicable for cases with slug flow or free surface flow. The mixture model uses one mixture flow velocity and solves for the volume fraction as a variable. However, the Euler-Euler model has a separate set

of equations for each phase; therefore it can compute the slip velocity between the two phases. Also, depending on the particulate loading, it is recommended to use the Euler-Euler model at higher GVF. Since the pump will be running high GVF flows, the Euler-Euler two phase flow model is used. A full multiphase coupled scheme was chosen for the pressure-velocity coupling and Green-Gauss Node Based scheme was applied as well as it provides more stability to the model. For the momentum, turbulent kinetic energy, and turbulent dissipation equations power law scheme was used, while for volume fraction and energy equation, QUICK scheme was implemented as these schemes can better handle the two phase flow as presented in Dostal et al. (2008). The courant number was chosen to be 200, while the Under Relaxation Factors (URFs) for momentum, pressure, density, turbulent kinetic energy, turbulent dissipation rate, turbulent viscosity, and volume fraction were chosen to be 0.2. The URF for the body forces was chosen to be 0.3. The URFs were chosen to be low so the model would not diverge, however it was critical keeping the same ratio between the URF values. If one URF was much higher relative to the others, this could lead the model to converge with wrong results. The temperature was fixed throughout the whole two phase simulations to reduce the complexity of the model.

The results show that the pump pressure head is 31 psi and the MVP G470 could provide a good mixing for the two phases as shown in Fig. 34. This is mainly due to the high rotating speed of the pump impeller relative to the axial speed of the flow. More results are shown in appendix B for this case.

4.2.2. Two phase model validation for the three stages at 200 psi inlet pressure

This section presents the CFD model validation for the two phase flow using the experimental data at 200 psi inlet pressure. In the case of incompressible single phase water, a single stage was simulated and compared to the experimental results assuming that each stage of the three stage pump will behave in the same way. However, this is not the case with the two phase flow for two reasons. Firstly, the design of the pump inlet does not allow for a homogenous mixing of the two phases as seen in Fig. 33 design 2. Therefore, the inlet has to be simulated in the same way as the experimental setup in order to predict the right behavior of the first stage. Secondly, because the flow contains compressible gas (air), the GVF changes across the three stages and therefore each stage has a different GVF distribution at the inlet. Consequently, the model of the whole three stages and the pump inlet has to be simulated to obtain the accurate pressure head of the pump for the case of the two phase flow.

In order to simulate one flow condition for two phase flow, a complete model including the inlet mixing chamber and the three stages has to be built as seen in Fig. 28. However, the current computers could not handle the whole three stages with the inlet for two phase flow using the Euler-Euler model due to the high number of variables at each node and the whole model will exceed twenty million nodes. Another way to simulate the three stages is implemented in this section in order to compare the total pressure head of the three stages with the experimental results.

Instead of modeling the whole three stages and the inlet together as shown in Fig. 28, another approach is considered. Figure 35 shows the pump simplified inlet and the first stage simulated together. The outlet from the first stage is much more homogenous than the inlet of the first stage. Therefore, the second and third stages are also simulated separately with uniform GVF distribution at the inlet assuming that the first stage will provide homogenous mixing of the two phases.

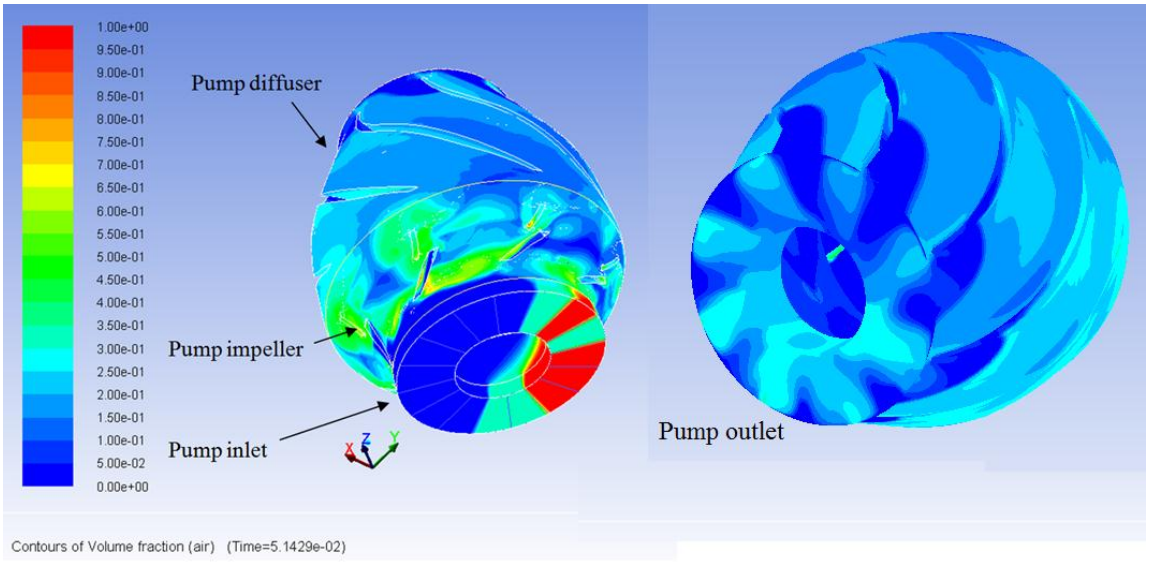

Figure 35. Pump inlet and first stage GVF distribution at inlet conditions of 20% GVF and 25 KBPD

Therefore, in order to simulate one operating condition of the pump, three models were simulated; the non-uniform pump inlet and the first stage together, the second stage with uniform inlet, and finally the third stage with uniform inlet. The boundary conditions used in these simulations were mass flow inlet at the inlets and

pressure outlet at the outlets. The pressure at the outlet was tuned during the simulation so the model would reach the exact inlet pressure as the experimental results.

Moving mesh was used to simulate the flow inside the rotating impeller and its interaction with the stationary diffuser and stationary inlet for the first stage. Euler-Euler two phase flow model was used. A full multiphase coupled scheme was chosen for the pressure-velocity coupling and Green-Gauss Node Based scheme was applied as well. For the momentum, turbulent kinetic energy, and turbulent dissipation equations power law scheme was used, while for volume fraction and energy equation, QUICK scheme was implemented. The courant number was chosen to be 200, while the Under Relaxation Factors (URFs) for momentum, pressure, density, body forces, and volume fraction were chosen to be 0.25. The URF for turbulent kinetic energy, turbulent dissipation rate and turbulent viscosity was chosen to be 0.1. The temperature was fixed throughout the whole two phase simulations to reduce the complexity of the model.

The model was simulated transiently and the pump speed was 3600 rpm. The bubble size chosen was 0.01 mm which is an assumed number based on the literature presented in Lissett (2007). Two GVF's of 10% and 20% were simulated for different flow rates of 20, 25, 30, and 35 KBPD, and the results were compared with the experimental data.

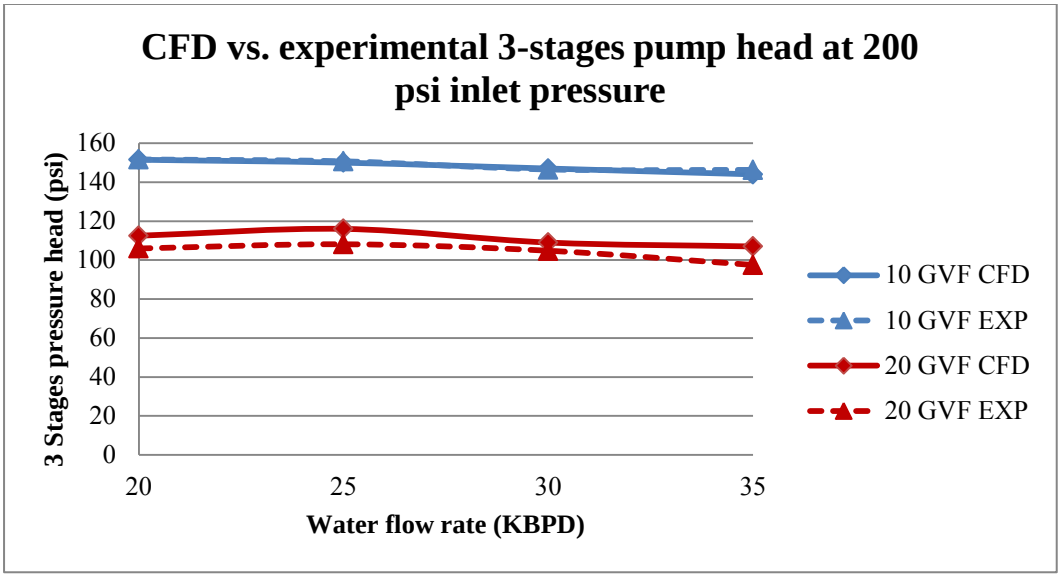

Figure 36. CFD vs. experimental data for the three stages at 200 psi inlet pressure

Figure 36 shows the data from both the CFD simulation and the experimental testing for the three stages MVP pump at 200 psi inlet pressure. The data shows that the CFD model is over predicting the pressure head at higher GVF (20%) by an average of 6.5%. The bubble size used in this CFD model is 0.01 mm. However, at lower GVF of 10%, the CFD model is predicting the experimental performance with very little error. This observation agrees with the data from the literature as the bubble size is smaller at lower GVF, so there is no need to change the bubble size at 10% GVF. However, more simulations were carried out with bigger bubble sizes (0.02, and 0.04 mm) for the 20% GVF inlet. The contour plot of the hub for one case is shown in Fig. 37 below. The model with 0.02 mm bubble size gives 3.15% lower pressure head than the 0.01 mm model, while the model with 0.04 mm bubble size shows 6.7 % less pressure head. At this flow condition the 0.04 mm bubble size model can better simulate the pump than the

smaller bubble sizes. Since the pump was simulated transiently, the higher GVF simulation takes a longer time to converge as the solution kept oscillating due to the dynamics involved with the compressible gas.

One of the main factors that cause ESP pressure degradation is the accumulation of the gas inside the pump impeller. According to the literature mentioned above, the gas pockets start to form on the impeller intake, and then they accumulate on the impeller blade pressure side. This phenomenon can still take place inside the MVP pump as seen in Figs. 37 and 41. Also, there is another gas pocket that starts to form at the small splitter blade of the MVP at the suction side as shown in Fig. 37. These gas pockets cause the pump head to degrade and affect the pump performance.

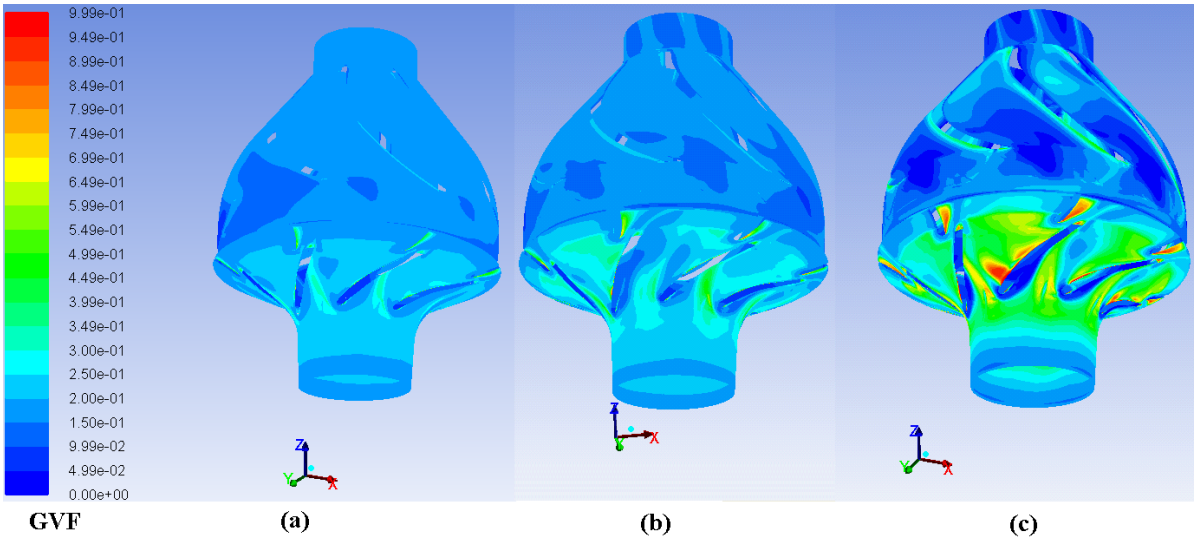

Figure 37. The GVF distribution for the uniform second stage with 30 KBPD and 20% GVF pump inlet, (a) bubble size 0.01 mm, (b) bubble size 0.02 mm, (c) bubble size 0.04 mm

Table 4. CFD results for the MVP pressure head per stage at 200 psi inlet pressure

Flow rate (KBPD)	Stage 1 GVF	Stage 1 (psi)	Stage 2 GVF	Stage 2 (psi)	Stage 3 GVF	Stage 3 (psi)
20	10%	43	8.26%	53	7.04%	55.5
20	20%	31.5	19.4%	40	16.4%	41
25	10%	42	8.4%	53	7.23%	55
25	20%	32	19.4%	41	16.5%	43
30	10%	41	8.4%	52	7.2%	54
30	20%	31	19.1%	38	16.2%	40
35	10%	40	8%	52	6.9%	52
35	20%	30	18.7%	38	15.8%	39

Table 4 shows the MVP pump pressure head for each stage from the CFD simulation. It is obvious that the pressure head is lower at the first stage as it is working to provide good mixing of the two phases as well as a pressure rise, while the pressure head of the second and third stages is higher as the flow is already mixed. The two phase CFD model can successfully predict the pump performance for the two phase flow at different flow rates and different GVF distribution.

4.3.3. Single stage at 950 psi inlet pressure

In this section, many single stage cases were simulated at 950 psi inlet pressure with uniform gas distribution at the inlet. Table 5 shows the test matrix for the different flow conditions simulated at 950 psi inlet pressure. Figures 38 and 39 show the Static pressure head of the pump at different flow rates and GVFs. The inlet conditions applied here were uniform mass flow inlet and pressure outlet.

Table 5. Test matrix for single stage MVP at 950 psi inlet pressure

		Static Pressure (psi) Differential Pressure relative to the pump inlet			Air Total Pressure (psi) Differential Pressure relative to the pump inlet			Water Total Pressure (psi) Differential Pressure relative to the pump inlet		
GVF%	**Flow-rate KBPD**	**inlet**	**interface**	**outlet**	**inlet**	**interface**	**outlet**	**inlet**	**interface**	**outlet**
5	15	0	42.53	50.12	0	45.58	50.31	0	81.21	54.879
5	20	0	43.17	48.09	0	46.18	48.33	0	81.54	53.5
5	25	0	43.762	49.03	0	46.51	49.34	0	78.974	55.057
10	15	0	41.902	49.272	0	45.01	49.465	0	81.38	53.76
10	20	0	41.5	47	0	46	47.7	0	83.1	52.7
10	25	0	40.93	45.53	0	44.5	44.9	0	78.45	51.2
25	15	0	34.994	39.524	0	38.11	39.78	0	74.42	44.504
25	20	0	37.2	41	0	39.6	40.6	0	71.8	46
25	25	0	33.4	38.9	0	36.1	39.3	0	66.5	45.3
32	15	0	32.557	36.877	0	35.55	37.15	0	70.42	42.079
32	20	0	30.612	36.722	0	33.429	37.133	0	66.361	43.195
32	25	0	28.7	30.9	0	31.2	31.6	0	58.2	38.78

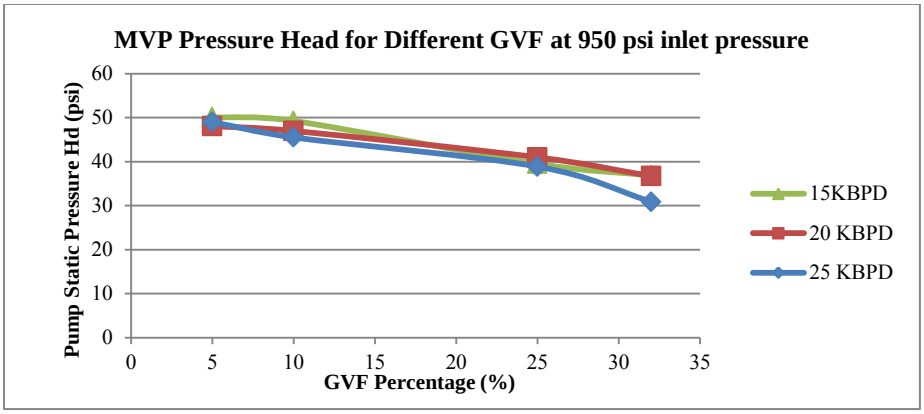

Figure 38. MVP static pressure head at different GVFs

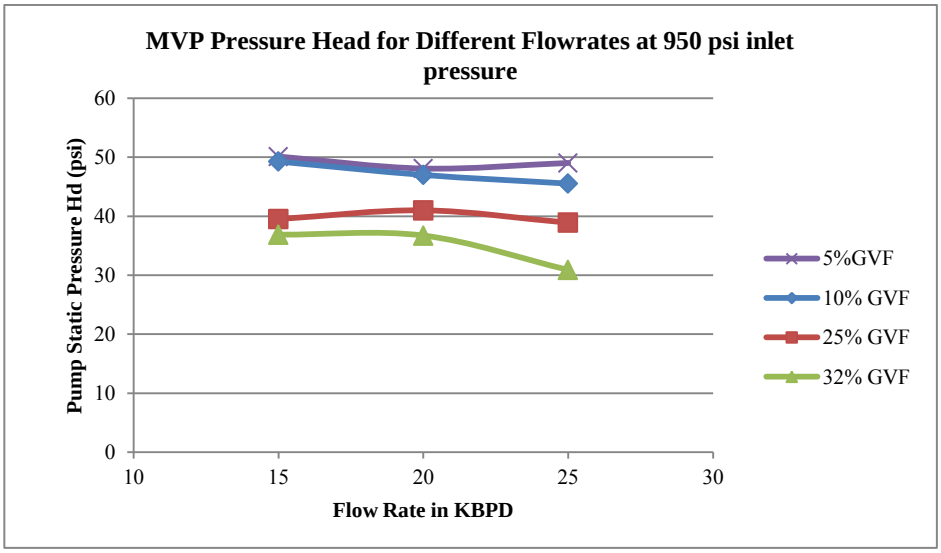

Figure 39. MVP static pressure head at different flow rates

The effect of using different bubble size in Fluent is given by equations (31) and (32). Increasing the bubble size increases the drag force between the two phases. According to the literature, the bubble size affects centrifugal pump performance. Different bubble sizes were simulated at 950 psi inlet pressure and 25 KBPD water flow rate with 25% GVF. The results are shown in Fig. 40 below, as increasing the bubble

size decreases the simulated pump performance. The exact bubble size can be determined using data from the literature or using a high speed camera to visualize the flow. More results from the CFD are presented in appendix B showing the effect of changing the bubble size in the model. When the bubble size increases, it becomes easier to separate the two phases from each other due to the higher drag force between the two phases. This leads to more gas accumulation that may lead to gas lock as seen in Fig. 41.

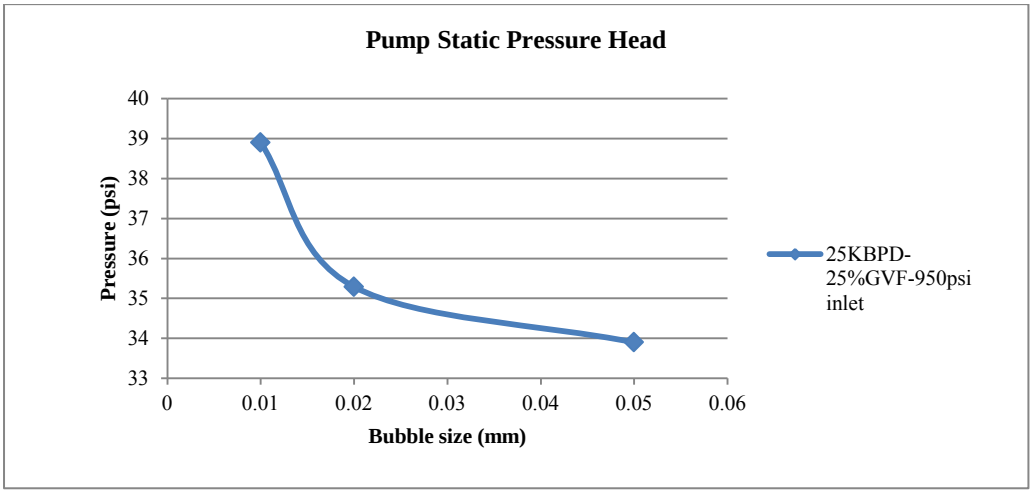

Figure 40. Pump static pressure for different bubble sizes

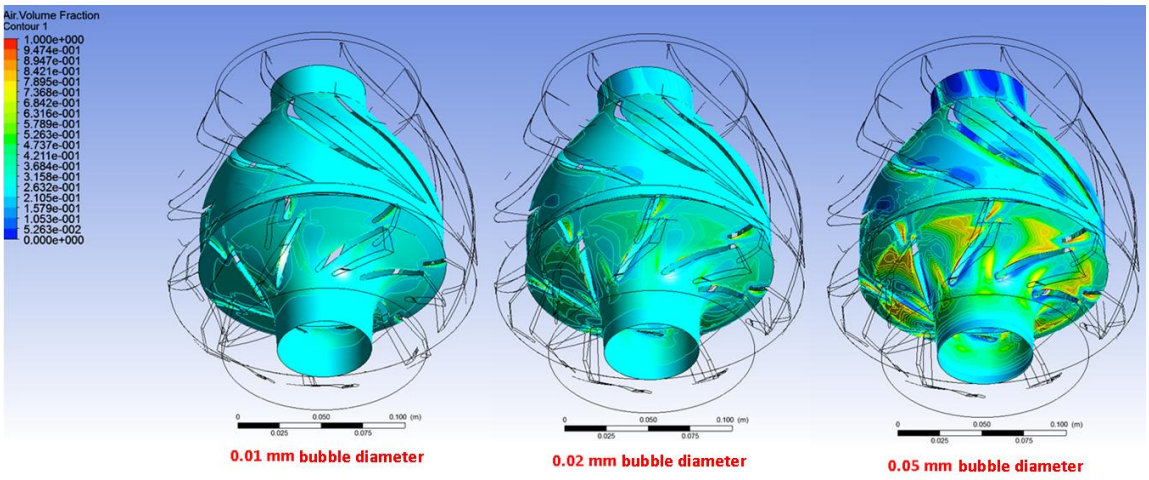

Figure 41. GVF distribution at different bubble sizes for 25 KBPD, 25% GVF, and 950 psi inlet pressure

Two phase modeling of the MVP was carried at different pressures and different flow conditions. The results from the CFD strongly match experimental results. Also the pump's first stage provides homogenous mixing of the two phases that enhances the performance of the next stages.

4.3. CFD based design

Many researchers such as Tonomura et al. (2004), Hui-min et al. (2010), and Fan et al. (2011), used CFD as a tool to improve existing designs. Since it is hard to analytically predict the behavior of fluids in complicated 3D geometries, CFD can be used to simulate the flow in different geometries and study the effect of changing these geometries on the behavior of the flow. In this section, a CFD-based design study is

presented that shows the behavior of the flow in different geometries. The new designs were able to increase the pump efficiency and reduce the losses in the diffuser.

4.3.1. Analysis for the existing pump design

After validating the CFD model for single phase flow, a more detailed analysis was carried out in an attempt to better understand the behavior of the flow inside the pump. A single stage of the MVP pump was simulated with 100% water as the working fluid at 3600 rpm. Two full revolutions of the impeller were simulated and the static and total pressures were monitored.

Table 6. Static and total pressures for 100% water for a single stage MVP

		Static Pressure (psi)				Total Pressure (psi)			
Speed (rpm)	**Flowrate (KBPD)**	**inlet**	**interface**	**outlet**	**Diffuser Pressure Increase**	**inlet**	**interface**	**outlet**	**Diffuser Pressure Loss**
3300	15	0	36.14819	38.88458	2.73639	0	75.04775	45.53859	29.50916
3300	20	0	38.38145	45.23201	6.85056	0	73.10127	48.80676	24.29451
3300	25	0	37.72714	45.92754	8.2004	0	72.55825	49.8251	22.73315
3600	15	0	46.47745	50.68195	4.2045	0	85.74508	57.76912	27.97596
3600	20	0	44.89183	53.29724	8.40541	0	85.91688	58.63568	27.2812
3600	25	0	45.71282	54.49746	8.78464	0	86.34242	58.17642	28.166
3600	35	0	42.15369	52.07612	9.92243	0	76.02186	55.07876	20.9431

Table 6 shows the static and total pressures for a single MVP stage with 100% water as the working fluid. A more detailed analysis at 35 KBPD shows that there are areas in the pump with flow separation and vortices causing significant losses. The current pump design includes an impeller with 7 splitter blades, and a diffuser with 8

solid blades as seen in Fig. 8. By examining the velocity contour plot and streamlines at the pump middle plane in Fig. 42, it is obvious that there are separation losses in the diffuser.

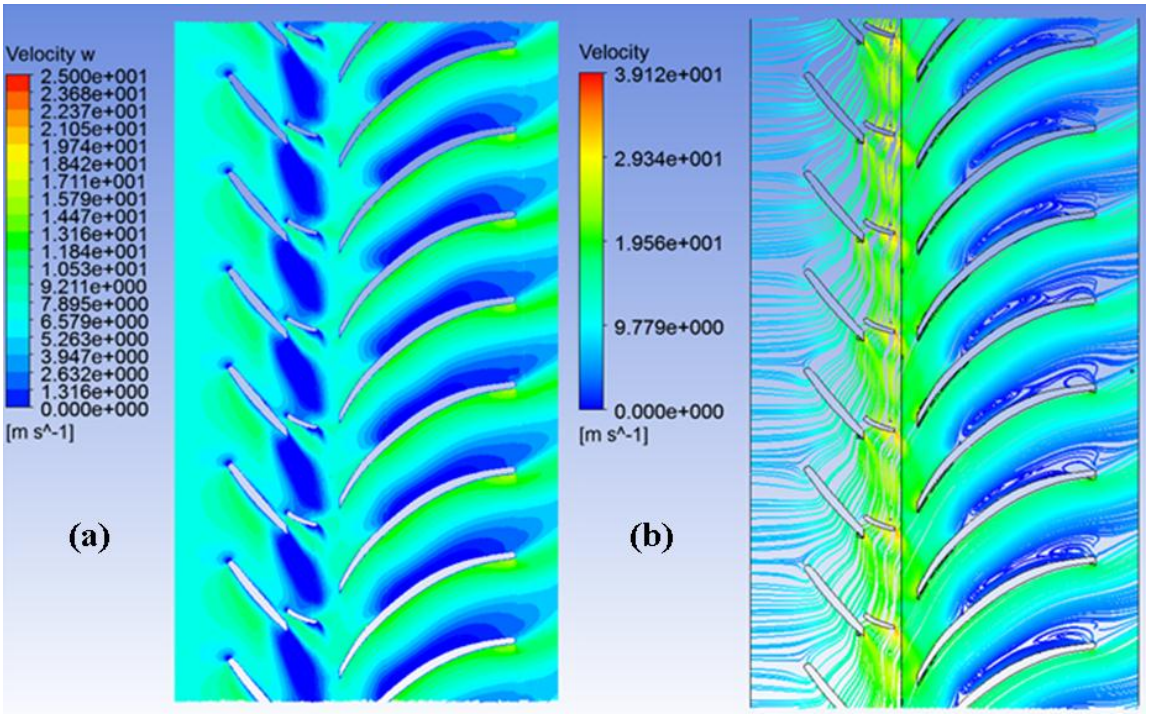

Figure 42. Velocity contour plot and streamlines for 35 KBPD with 100% water, (a) velocity in the Axial direction "w" (m/s), (b) absolute velocity magnitude (m/s)

Flow separation can be reduced by increasing the momentum of the flow. This can be achieved by either increasing the speed of the flow, or increasing the mass flow rate of the flow in the pump. Figure 43 shows that the static pressure increase across the diffuser increases with higher pump speeds and higher flow rates. Also Fig. 44 shows that the total pressure losses across the diffuser are less with higher speeds and higher

flow rates. The data in these two figures prove that increasing the momentum of the flow reduces the losses in the diffuser.

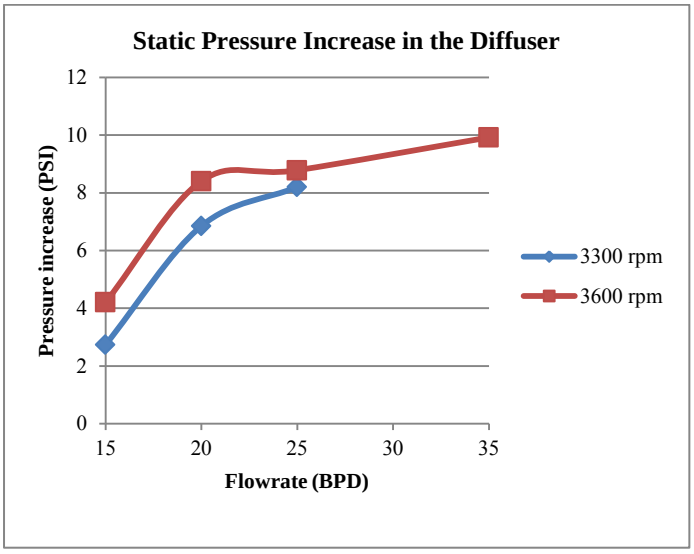

Figure 43. Static pressure increase across the diffuser

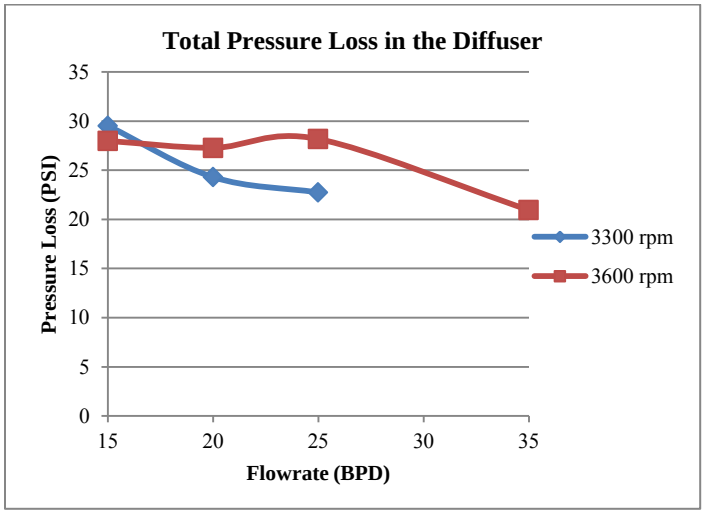

Figure 44. Total pressure loss across the diffuser

Separation losses in the diffuser also affect the efficiency of the diffuser as it inhibits the flow from reaching the desired static pressure at the diffuser outlet. This phenomenon reduces the efficiency of the current pump stage. Moreover, the flow at the diffuser outlet is not homogenous and has strong vortices that cause the flow at the outlet of the diffuser to be non uniform with areas of almost zero velocity as seen in Fig. 45 in blue contour plot. According to the study in the first section of this chapter; this increases the losses in the next impeller stage by 8%. Therefore, by reducing the separation losses in the current diffuser design, a better multistage pump performance can be achieved due to the higher efficiency diffuser in one stage and the higher impeller efficiency at the next stage.

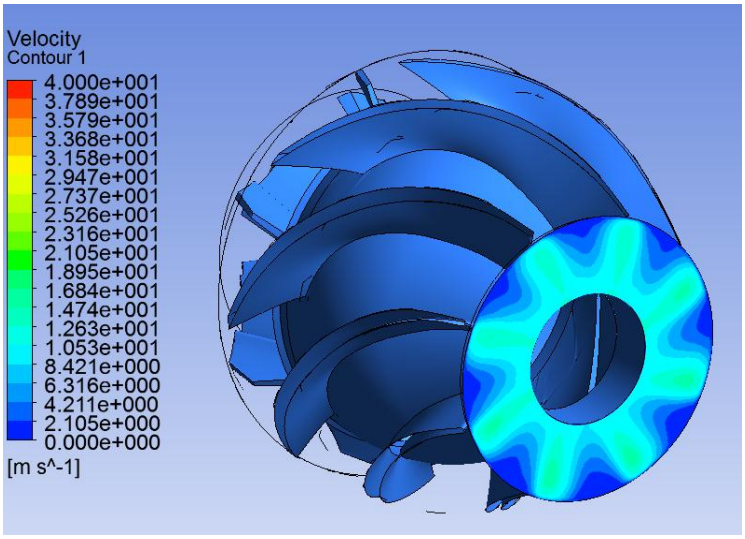

Figure 45. Velocity contour plot at the outlet of diffuser at 35 KBPD

4.3.2. New diffuser designs

In this section, new diffuser designs are presented in an attempt to reduce the diffuser losses and better understand the flow behavior inside the pump. This can be achieved by changing the diffuser design and utilizing the CFD to analyze the flow and compare its behavior to other designs.

4.3.2.1. Changing the diffuser length

In this section different diffuser lengths are presented. The main objective of this study is to understand the effect of changing the diffuser length on the pump behavior. Three different diffuser lengths are presented; shorter, normal, and longer diffuser designs. The shorter is 10% shorter than the original MVP G470 design, while the normal is the same like the original design and the longer is 10% longer than the original diffuser design. The working fluid is 100% water and the flow rate was set to be 45 KBPD. The study was carried out for single phase only in order to minimize the variables during the comparison of different designs. The static and dynamic pressures across the pump were both monitored. Figure 46 shows the three designs with the static pressure contour plot, while table 7 shows the data for each design. Also Fig. 47 shows the streamlines at the pump middle plane, which illustrates why the longer diffuser can be a worse design than the other two designs.

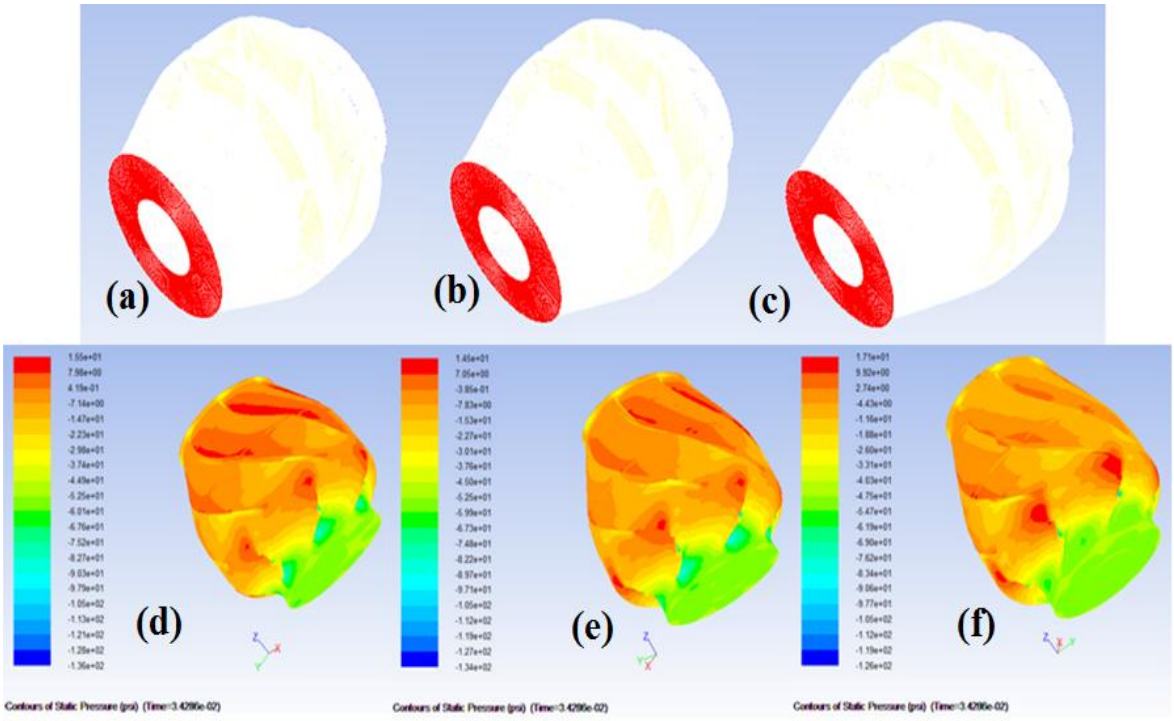

Figure 46. Different diffuser lengths, (a) shorter diffuser geometry, (b) normal diffuser geometry, (c) longer diffuser geometry, (d) shorter diffuser static pressure, (e) normal diffuser static pressure, (f) longer diffuser static pressure

Table 7. Pressures of different diffuser lengths

	Shorter diffuser	**Normal diffuser**	**Longer diffuser**
Pump Total Pressure (psi)	52.5	53.2	47.1
Pump Static Pressure (psi)	50.5	50.5	44.6

From the data shown in table 7, it is observed that the longer diffuser is much worse than the normal and shorter diffuser designs. This is because the separation losses

increase across the longer diffuser and extend to cover most of the diffuser blades as seen in Fig. 47 below that shows the streamlines at the middle plane.

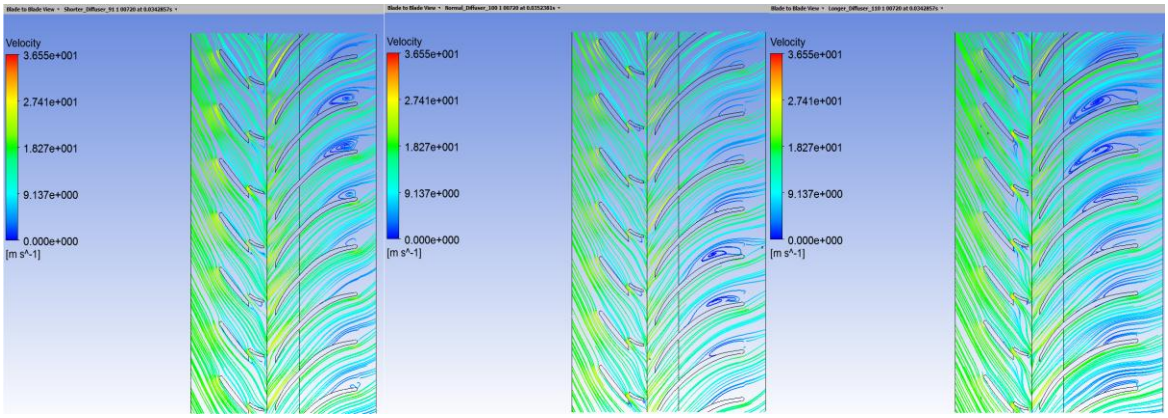

Figure 47. Streamlines of the shorter, normal, and longer diffusers from left to right

The shorter diffuser design almost has the same static pressure across the pump and does not affect the flow much compared to the original diffuser design. Since they both have the same pressure head, it may be more feasible to use the shorter design as it will occupy less space, and provide a more stiff assembly for the vertical pump.

4.3.2.2. Modifying the diffuser blade design

Since the flow separation shown above in Fig. 47 takes place on the pressure side of the diffuser blades, different features were considered to reduce the flow separation on the diffuser blades. A single stage of the MVP pump is simulated using single phase flow with 100% water as the working fluid at a flow rate of 35 KBPD. Figures 42 and 45

show the results from the original design. The results show the flow separation and the zones at the diffuser outlet with zero velocity due to the vortices.

In order to improve the existing design, a slot shown in Fig. 48 was created in the diffuser blade, and the model was simulated transiently until it reached steady state solution. The main objective of adding this slot is to allow the flow to go from the high pressure side to the low pressure side of the blade in order to increase the momentum of the fluid and reduce separation.

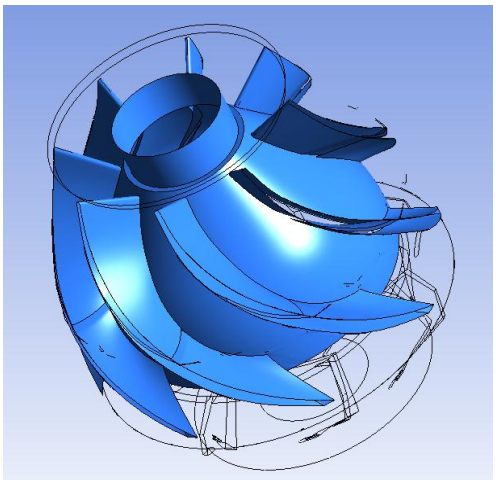

Figure 48. A single slot blade

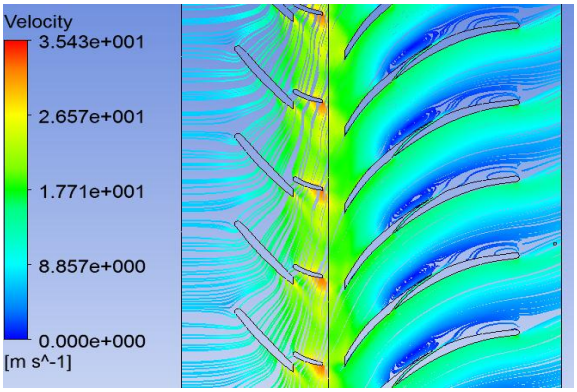

Figure 49. A single slot blade streamlines at the pump middle plane

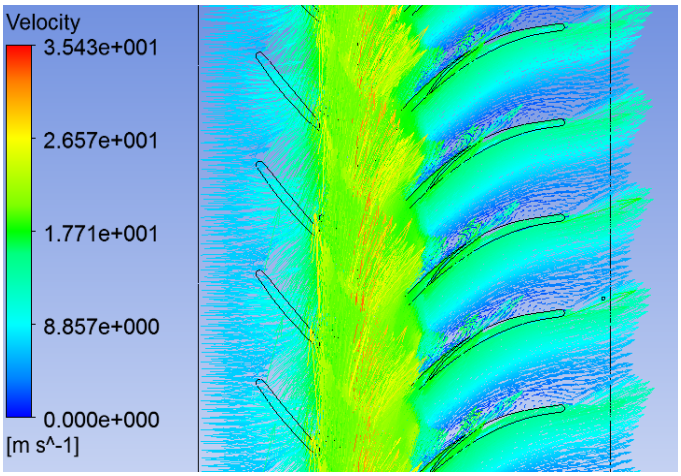

Figure 50. A single slot blade velocity vectors at the pump middle plane

Figures 49 and 50 show the streamlines and the velocity vectors after adding a slot to the current pump design. The results show that the water is flowing from the high pressure side to the lower pressure side, and this reduces the separation after the slot. However, the separation still occurs before the opening at the slot downstream.

Figure 51 shows the velocity contour plot of the flow at the outlet of the diffuser with the slotted blade. The velocity contour is slightly better than that of the original design shown in Fig. 45. The new design only increased the static pressure of the pump by 1%.

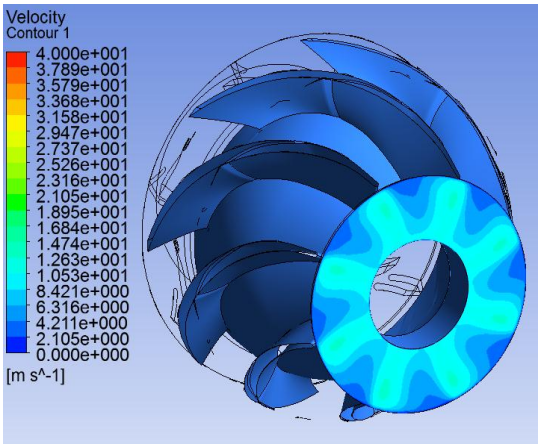

Figure 51. Velocity contour plot at the outlet of the diffuser for the single slotted design

Since the slot changed the direction of the flow and could not eliminate the flow separation, a new design was simulated with the diffuser blade split and shifted as shown in Fig. 52.

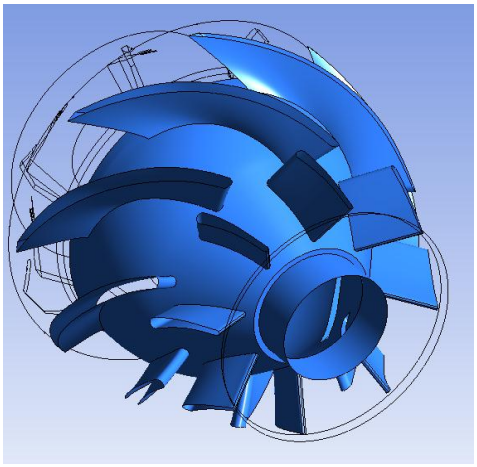

Figure 52. Split and shifted diffuser blade

The objective of having this design is to provide a mixing of the flow from the low pressure side and the high pressure side in an attempt to reach a more homogenous flow. This design should help eliminating the separation especially at the outlet of the diffuser.

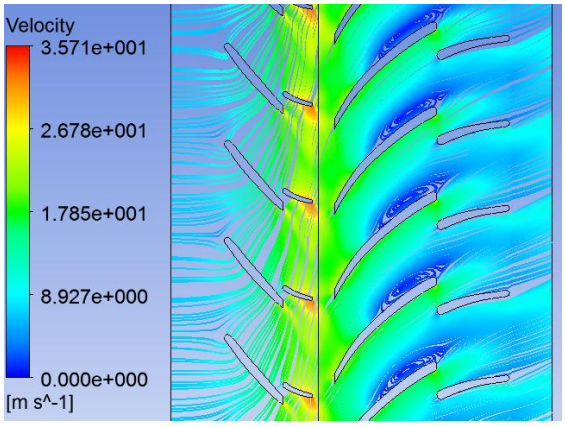

Figure 53. Split and shifted blade streamlines at the pump middle plane

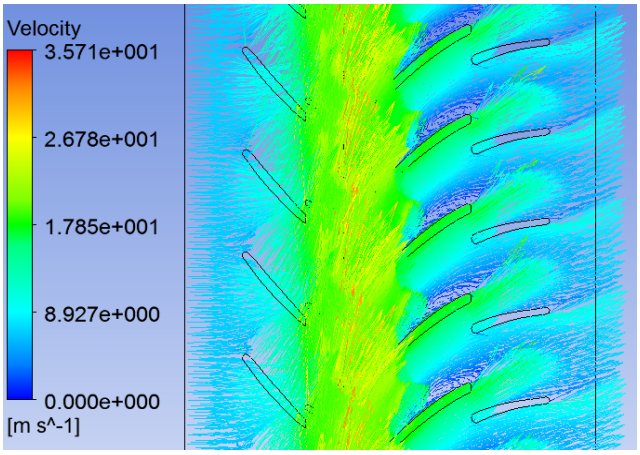

Figure 54. Split and shifted blade velocity vectors at the pump middle plane

Figures 53 and 54 show the velocity streamlines and vectors of the flow in the pump with the split and shifted blade. The new design provides better mixing of the flow. It also makes the flow more homogenous at the outlet of the diffuser, as shown in Fig. 53, which was shown previously to improve the next impeller's performance.

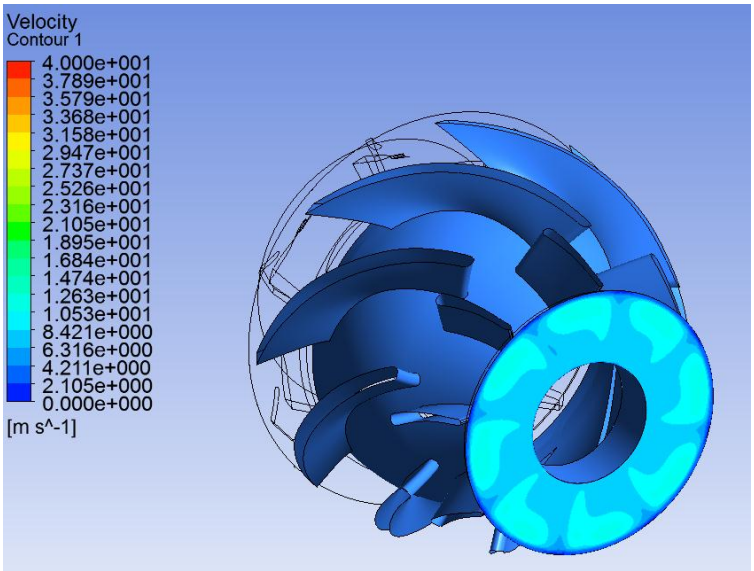

Figure 55. Splitted and shifted blade velocity contour at the pump outlet

Flow separation still takes place in the pump at the diffuser blades before the split. Moreover, the friction losses in the diffuser increased due to the splitter blade. Therefore, this design improved the outlet of the pump by making it more homogenous, but it increased the friction losses in the diffuser causing the static pressure across the pump to drop by 4% compared to the original design.

Another slot was added to the diffuser blades in order to eliminate the separation at the blades as seen in Fig. 56, however the friction losses were more and the outlet was les homogenous than the design seen in Fig. 55.The design shown in Fig. 56 resulted in a drop of 8% in static pressure compared to the original pump design.

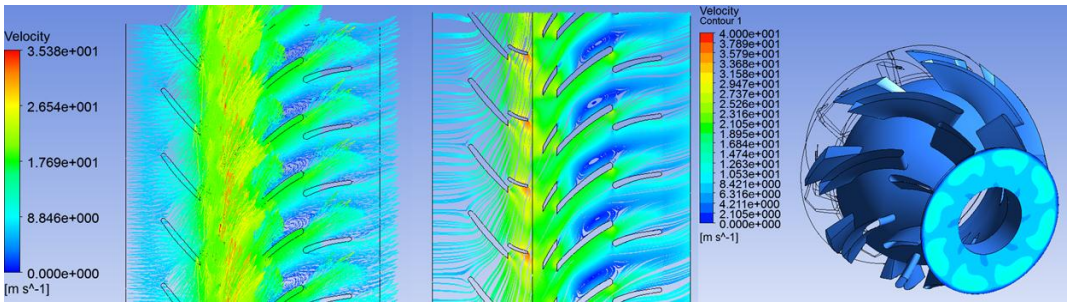

Figure 56. Three slplitted and shifted blades velocity vectors, streamlines, and contour plot

Another feature was added to the blades of the pump in order to improve the pump design as seen in Fig. 57. A nozzle slot was added near the blade upstream while two slots were added at the hub and the casing near the blade downstream. The main objective of the nozzle slot is to create a jet near the blade wall in order to eliminate the flow separation. However the other slots at the hub and the casing should relief the pressure and also help reducing the flow separation.

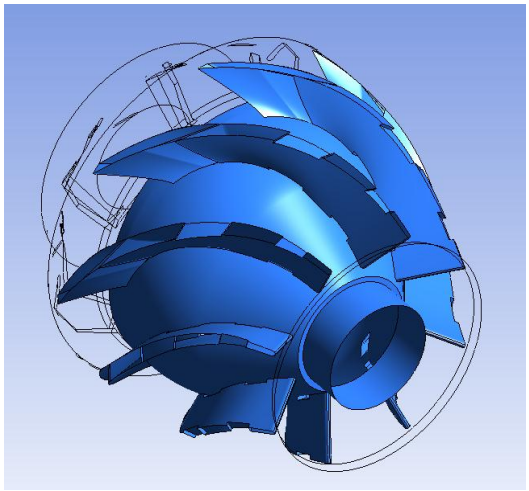

Figure 57. Three features in the diffuser blade

The design with the three features in the diffuser blade shown in Fig. 57 provided a better pump performance with an increase in the pump static pressure head by 1.5% compared to the original design. This was mainly because the nozzle split near the blade upstream created a jet with higher velocity causing the momentum of the flow to increase near the blade pressure side and this delayed the separation on the blade wall as seen in Figs. 58 and 59 and resulted in a more homogenous flow at the outlet of the diffuser as seen in Fig. 60 compared to the original design.

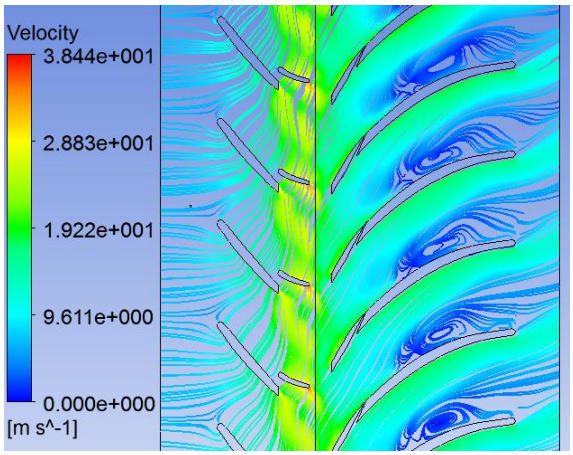

Figure 58. Streamlines for the pump design with three features in the diffuser blade

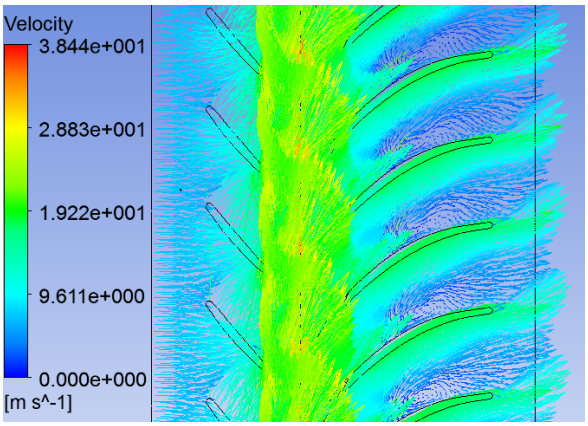

Figure 59. Velocity vectors for the pump design with three features in the diffuser blade

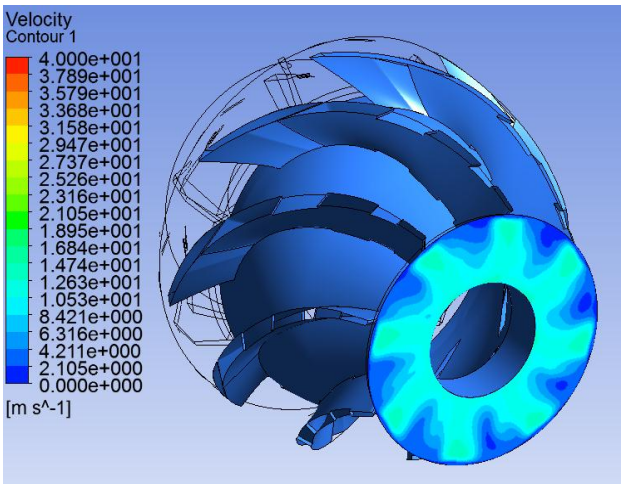

Figure 60. Velocity contour plot for the pump design with three features in the diffuser blade

The nozzle slot shown above was able to create a jet that pushed the flow at the area of separation and this improved the pump performance near the upstream side of the blade. A new design is considered with three nozzle slots across the diffuser blades that

should improve the pump performance and increase the pressure head across the pump as shown in Fig. 61.

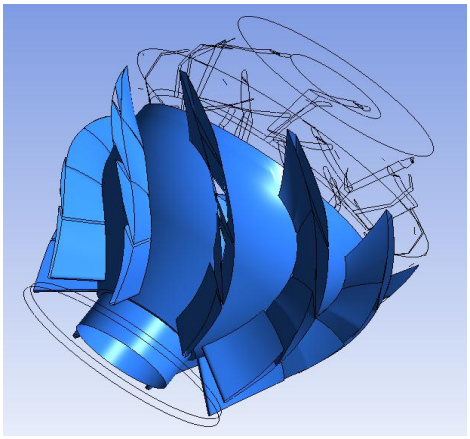

Figure 61. Three nozzle slots in the diffuser blade

These three nozzles were able to create a jet on the blade pressure side that totally eliminated the separation from taking place on the blade wall as seen in Fig. 62. Also, Fig. 63 shows the velocity vectors of the flow in the diffuser with the jets created at these three slots. The static pressure across the pump increased by 3.2% and the flow at the outlet of the diffuser became more homogenous as seen in Fig. 64. However, the separation still took place between the blades and this is due to the separation that happens on the hub of the diffuser as seen in Fig. 65. Therefore, more designs are considered to reduce the separation on the diffuser hub.

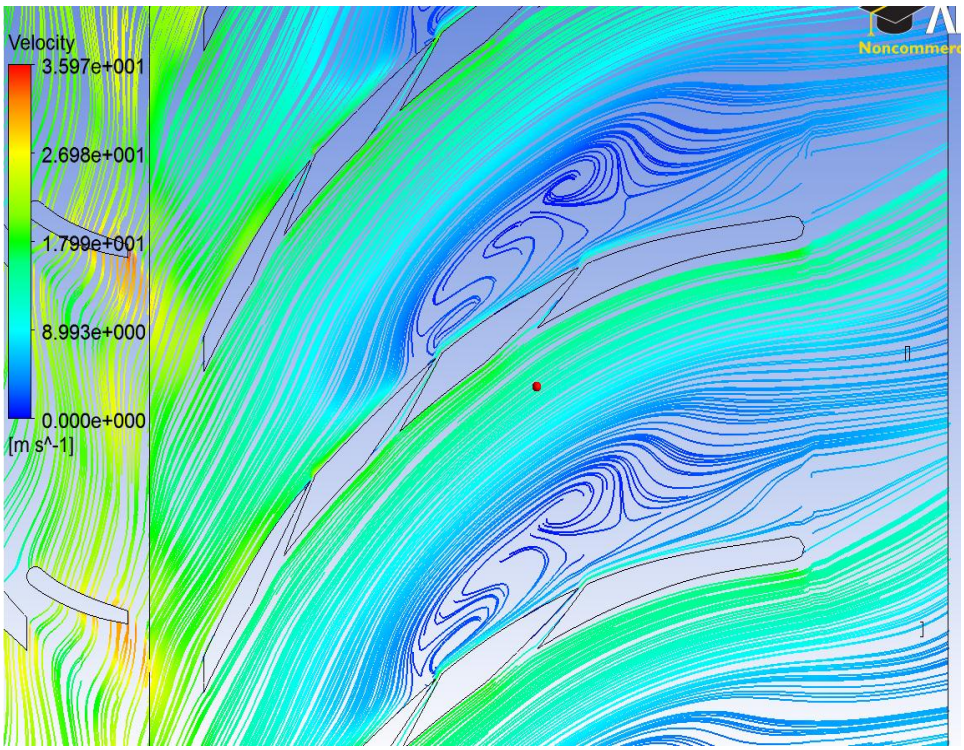

Figure 62. Streamlines for the three nozzle slots design

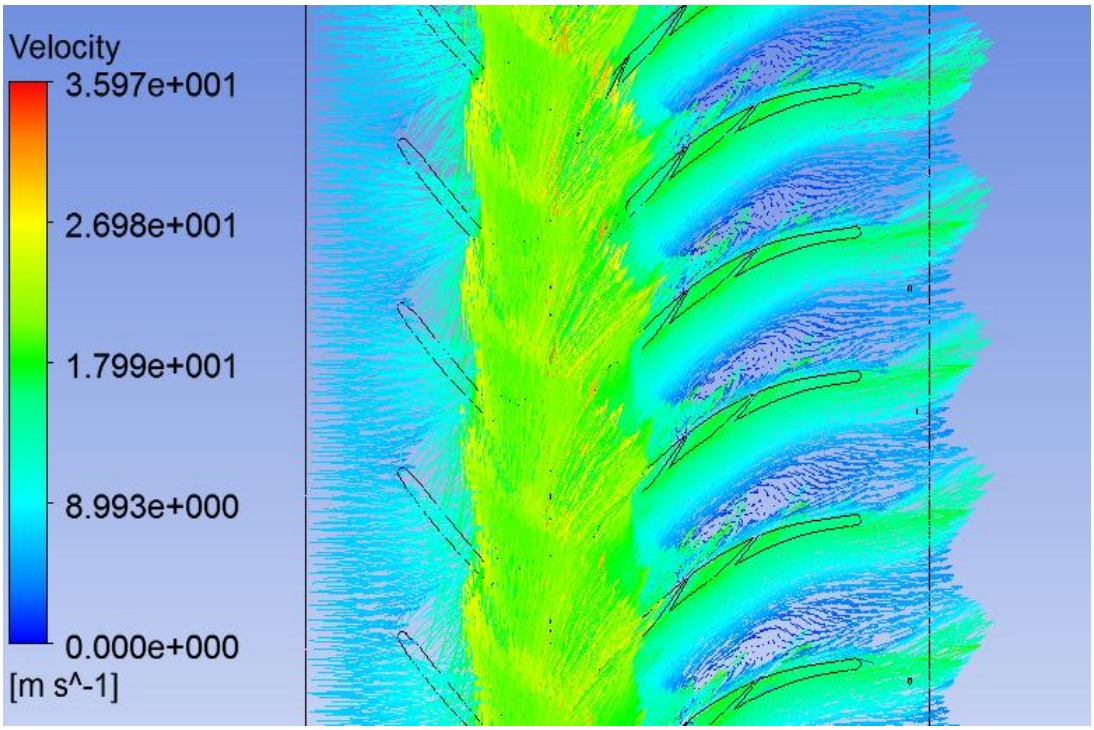

Figure 63. Velocity vectors for the three nozzle slots design

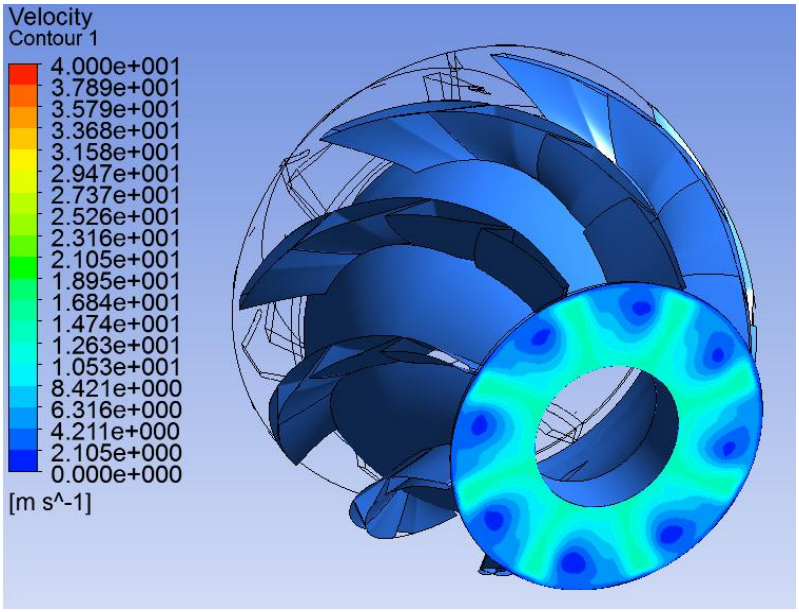

Figure 64. Velocity contour plot for the three nozzle slots design

4.3.2.2. Modifying the diffuser profile

By examining the flow in the meridional plane, a flow separation takes place on the diffuser hub due to the curvature in the diffuser profile as seen in Fig. 65.

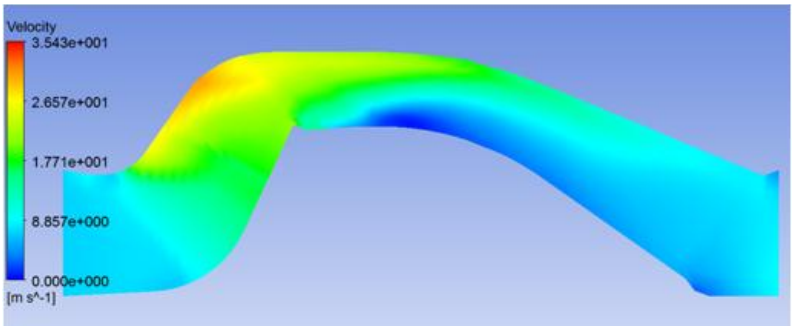

Figure 65. Velocity contour plot at the meridional plane of the original pump design

The dark blue area in Fig. 65 at the diffuser hub shows the flow at zero velocity, which indicates the flow separation at this area. Therefore, a different approach should be considered to reduce the separation in the diffuser other than modifying the diffuser blades. According to Schobeiri (2005), in compressors design, there is a tradeoff between separation losses and friction losses as increasing the number of blades in the stator decreases the separation losses while the friction losses increase. Therefore according to Fig. 66, there is an optimum number of blades that can be chosen to reduce the total losses across the stator. Utilizing the same concept in the MVP diffuser design, a new design with more number of blades was simulated and the performance of the new design was compared to the original diffuser design.

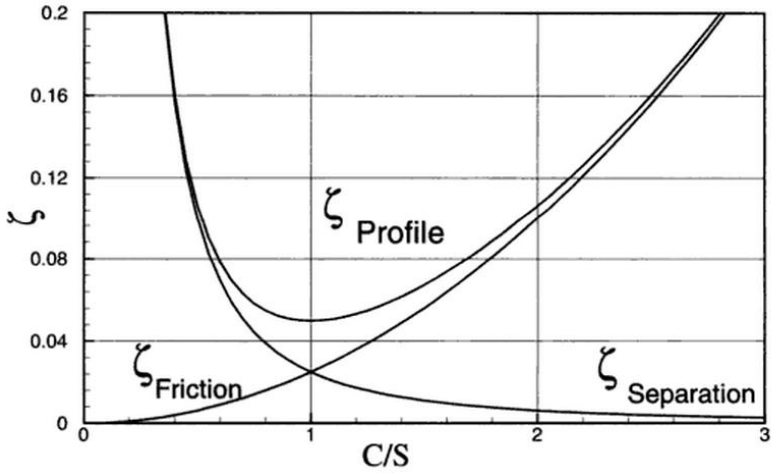

Figure 66. Profile loss coefficient as a function of C(spacing)/S(chord) ratio (Schobeiri 2005)

The new design consists of 10 diffuser blades as seen in Fig. 67, but the rest of the design is the same like the original MVP pump design. The results show that the 10 blades diffuser reduced the separation compared to the original design. The static pressure head across the pump with the 10 blades diffuser is 3.2% higher than the static pressure of the original pump design. Figures 68 and 69 show the streamlines and the pressure contour plot at the pump outlet respectively.

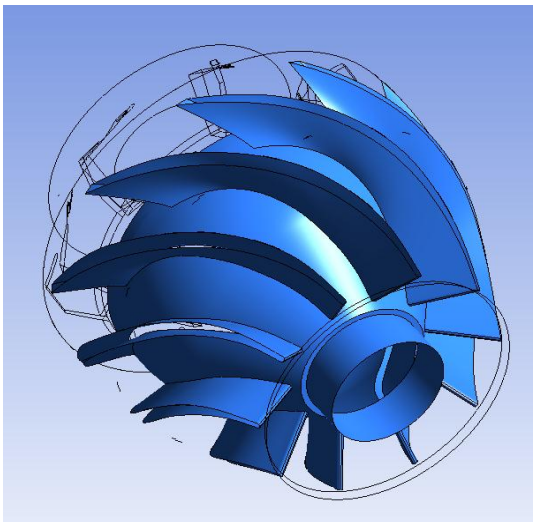

Figure 67. A ten blade diffuser

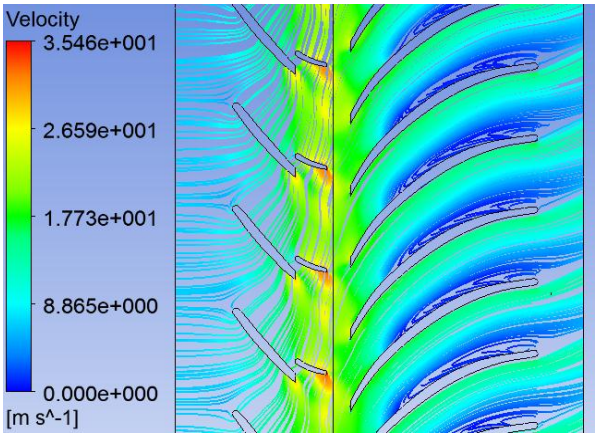

Figure 68. Streamlines for the ten blade diffuser design

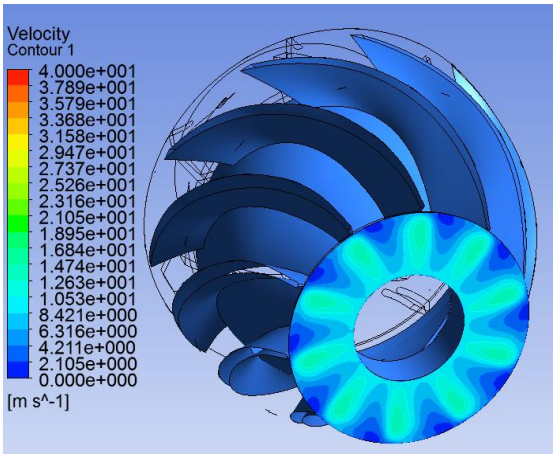

Figure 69. Velocity contour plot for the ten blade diffuser design

The profile of the diffuser in the meridional plane was also considered as the separation takes place on the curvature of the diffuser hub. In gas turbine engines, the shape and cross-section of the diffuser can reduce the separation at the exit of the turbine. Applying the same concept on the current diffuser design, changing the cross-section geometry of the diffuser can reduce the separation. Two different simple diffusers were simulated under the same flow velocity of 10 m/s at the inlet, and the results are shown in Figs. 70 and 71. The bell diffuser increases the cross-section of the diffuser rapidly in the beginning causing separation to happen early, while the trumpet diffuser increases the cross-section of the diffuser rapidly near the end causing the separation to delay.

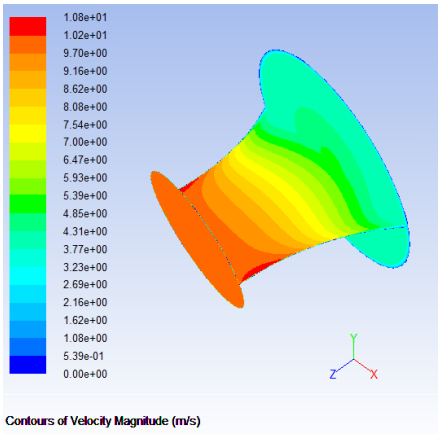

Figure 70. Trumpet diffuser velocity contour plot (m/s)

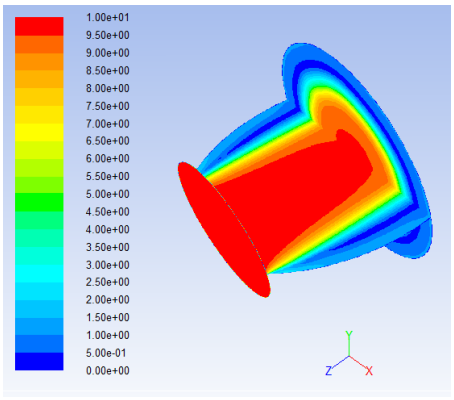

Figure 71. Bell diffuser velocity contour plot (m/s)

The static pressure increase across the bell diffuser was 1 psi only, while the static pressure increase across the trumpet diffuser was 6 psi. The blue contours in Fig. 71 show the flow separation, while with the other trumpet design there is no separation in such diffuser. The same concept of having a trumpet shaped cross-section diffuser was applied on the MVP diffuser design. The diffuser with the meridional cross section shown in Fig. 72 (a) is modified to the new design shown in Fig. 72 (b). The results

show better performance of the new design in Fig. 72 (b) as the static pressure head across the pump increased by 2.2%. Moreover, the blue contour showing the separation in the diffuser is very small compared to the separation in the original design.

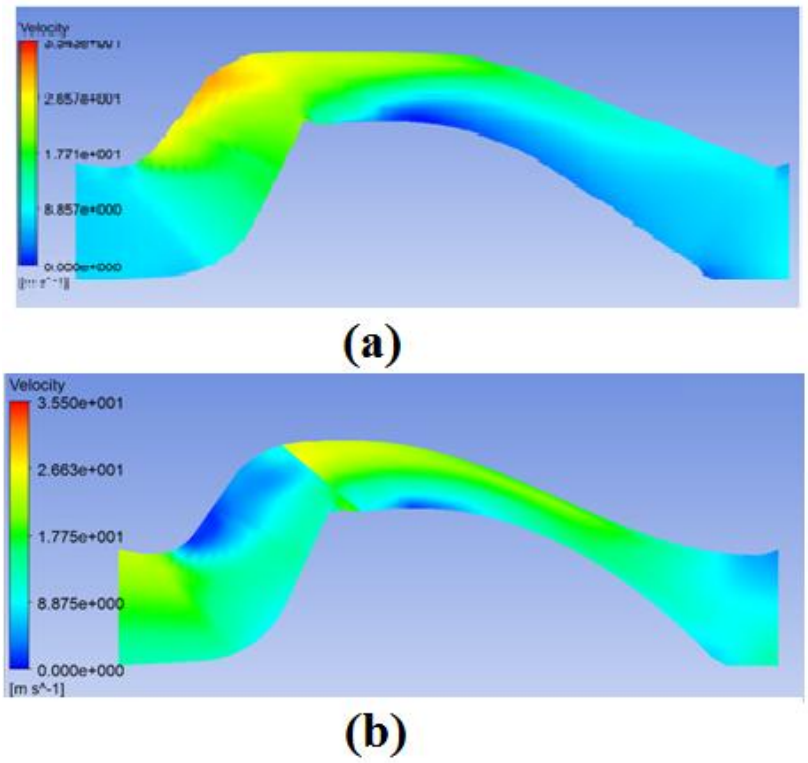

Figure 72. Velocity contour plot for trumpet diffuser design in the meridional plane

The separation is shown to be much less and is delayed up to the tip of the diffuser blades as shown in Fig. 73.

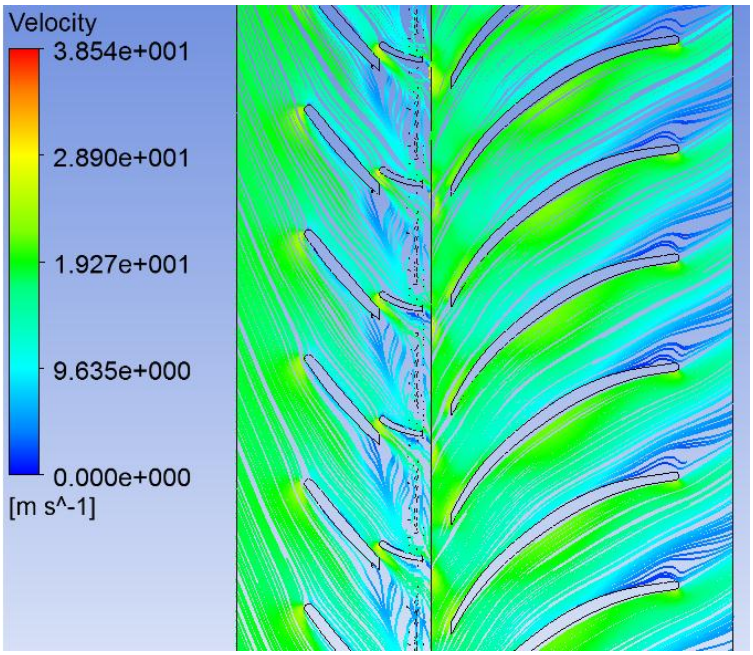

Figure 73. Streamlines for trumpet diffuser design at the pump middle plane

Another design is considered with a steeper trumpet shaped cross-section and 10 blades is considered. The results of the design are worse than the original design, and the static pressure is 5% less across the pump. The streamlines and velocity meridional plane are shown in Figs. 74 and 75. This is because the middle of the diffuser cross-section was made to be very thin compared to the designs shown in Fig. 72. However, the separation is delayed and it only took place at the end of the diffuser blade.

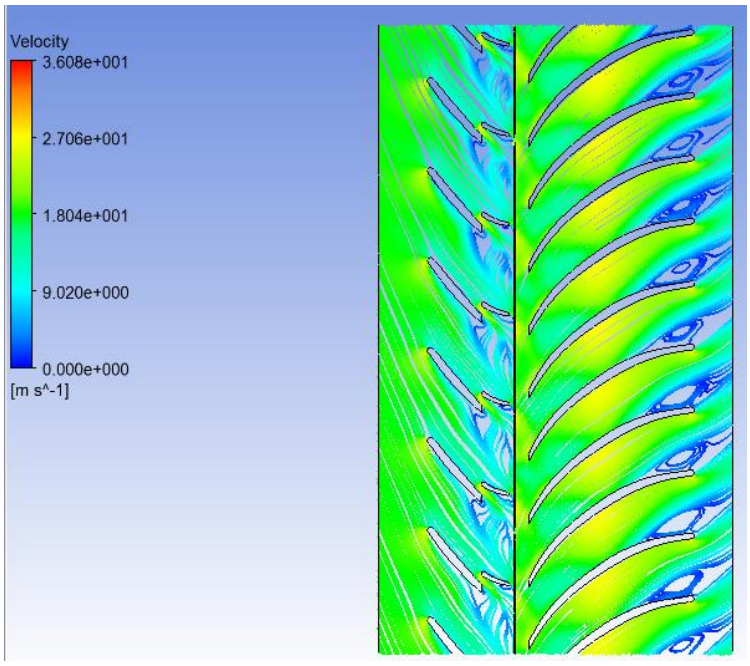

Figure 74. Streamlines at the middle plane of the trumpet diffuser with 10 blades

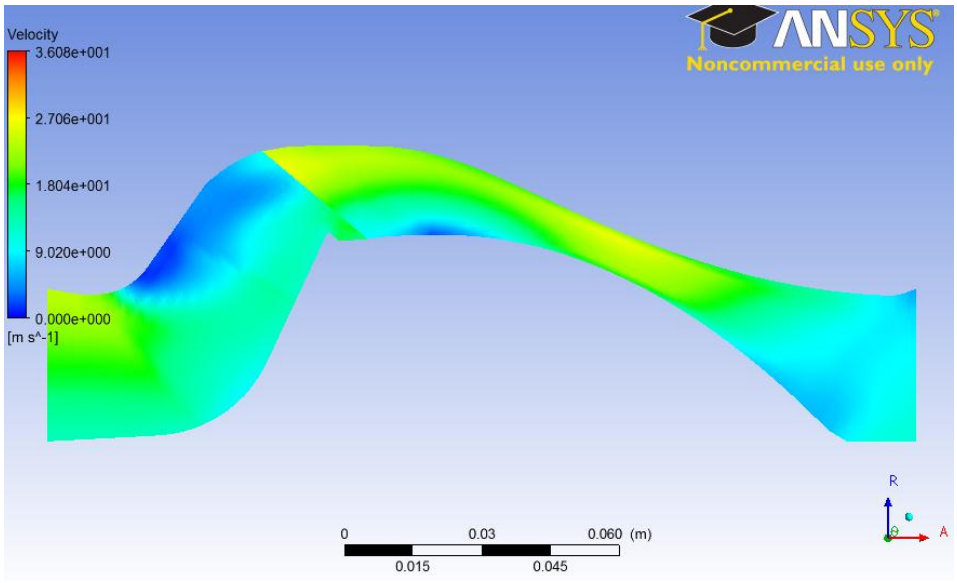

Figure 75. Meridional plane velocity contour of the trumpet diffuser with 10 blades

The losses in the MVP pump diffuser due to separation degrade the pump performance and reduce the pump efficiency. Different designs showed the potential of increasing the pressure head across the pump by reducing the diffuser losses. Optimizing the number of diffuser blades and improving the diffuser profile can reduce the losses significantly and improve the pump efficiency.

5. CONCLUSIONS AND RECOMMENDATIONS

The CFD simulations of the first three stages of a MVP electrical submersible pump are performed for single phase and two phase flows. The CFD models were validated using single phase and two phase flow experimental data. The CFD models showed excellent agreement with the experimental results. The analysis of the CFD results showed there are separation losses in both the pump impeller and diffuser. The pump inlet and the three stages were modeled together and the simulations showed that the separation in one stage of the pump reduces the performance of the next stage as well. The pump inlet and the first stage were modeled together for two phase flow at 400 psi inlet pressure with 32% GVF using Euler-Euler model. The data showed that the current pump inlet does not provide homogenous mixing of the two phases and this is better to understand the pump capability of mixing. The first stage helped providing good mixing of the two phases, but there was still significant circumferential variation, however, this improved the performance of the next stages of the MVP pump. Three stages were simulated using non-homogenous two phase flow at 200 psi at the pump inlet. The data of the static pressure head across the three stages were compared to the experimental results and the CFD model showed excellent agreement with the experimental results. More CFD simulations of two phase flow in a single stage MVP were simulated at 950 psi inlet pressure. The results showed that the pump performance decreases with increasing the flow rate and the GVF.

Different designed were simulated to achieve a better pump performance in an attempt to reduce the separation losses in the pump diffuser. The longer diffuser design showed more losses. Splitting the diffuser blade resulted in a more homogenous flow at the pump outlet but did not increase the pressure head across the pump. Three split blades at the diffuser caused more friction losses. Adding nozzle slots in the diffuser blades increased the pressure head of the pump by 3.2%, while increasing the number of blades by 2 increased the pressure head by 3.2%. Changing the diffuser meridional profile also improved the pump performance by 2.2% and delayed the separation in the diffuser significantly. A combination of the trumpet diffuser design with the 10 blades was carried out, but the results showed a lower pump head than the original design. This is due to the separation taking place near the trailing edge of the diffuser blades.

Since the CFD model could successfully predict the pump performance for single and two phase flows, it is recommended to use the CFD model to simulate extreme conditions using oil and natural gas as the working fluids. Moreover, there is a high potential of improving the pump performance by eliminating the separation losses in the diffuser. A better design that may combine more than one of the modified designs mentioned above can be considered that will provide a higher pump performance.

REFERENCES

Andras, E., 1997. Two Phase Flow Centrifugal Pump Performance. Ph.D. Dissertation, Idaho State University, Pocatello, ID.

Barrios, L., 2007. Visualization and Modeling of Multiphase Performance Inside an Electrical Submersible Pump. PhD. Dissertation, The University of Tulsa, Petroleum Engineering Department, Tulsa, OK.

Barrios, L., M. G. Prado, 2009. Modeling Two Phase Flow Inside an Electrical Submersible Pump Stage. ASME 2009 28th International Conference on Ocean, Offshore and Arctic Engineering. Honolulu, Hawaii, USA: ASME, 469-484.

Benra, K. F., H. J. Dohmen, 2004. Theoretical and Experimental Investigation on the Flow Induced Vibrations of a Centrifugal Pump. Biennial International Pipeline . Calgary, Alberta, Canada: Proceedings of the Biennial International Pipeline Conference, 39-46.

Bonaiuti, D., A. Arnone, M. Ermini, L. Baldassarre, 2006. Analysis and Optimization of Transonic Centrifugal Compressor Impellers Using the Design of Experiments Technique. Journal of Turbomachinery, 5, 786-797.

Byskov, Rikke K, Nicholas Pedersen, 2003. Flow in a Centrifugal Pump Impeller at Design and Off-Design Conditions - Part II: Large Eddy Simulations. Journal of Fluids Engineering, 125, 73-83.

Caridad, J., F. Kenyery, 2004. CFD Analysis of Electric Submersible Pumps (ESP) Handling Two-Phase Mixtures. Journal of Energy Resources Technology (ASME), 126.2, 99-104.

Dostal, V., Zelezny, V., Zacha, P., 2008. CFD Simulations of Pb-Bi Two-Phase Flow. International Youth Nuclear Congress. Interlaken, Switzerland: IYNC, 249.1-249.8.

Estevam, V., 2002. A Phenomenological Analysis about Centrifugal Pump in Two-Phase Flow Operation. Ph.D. Thesis, SP Brasil: Faculdade de Engenharia Mecânica, Universidade Estadual de Campinas, SP, Brazil.

Fan, J., Eves, J., Thompson, H. M., Toropov, V. V., Kapur, N., Copley, D., Mincher, A., 2011. Computational Fluid Dynamic Analysis and Design Optimization of Jet Pumps. Computers & Fluids, 46, 212-217.

Feng, J., Benra, F.-K., Dohmen, H.J., 2009. Unsteady Flow Visualization at Part-Load Conditions of a Radial Diffuser Pump: by PIV and CFD. Journal of Visualization, 12, 65-72.

Fluent, ANSYS, 2009. Fluent Theory Guide. Fluent Theory Guide, SAS IP, Inc., https://www.sharcnet.ca/Software/Fluent12/html/th/node3.htm

Furuya, O., 1985. An Analytical Model for Prediction of Two-Phase (Noncondensable) Flow Pump Performance. Journal of Fluid Engineering, 107, 139-147.

Gonzalez, J., Santolaria, C., 2006. Unsteady Flow Structure and Global Variables in a Centrifugal Pump. Journal of Fluids Engineering, Transactions of the ASME, 128, 937-946.

Gonzalez, J., Fernandez, J., Blanco, E., Santolaria, C., 2002. Numerical Simulation of the Dynamic Effects Due to Impeller-Volute Interaction in a Centrifugal Pump. Journal of Fluids Engineering, Transactions of the ASME, 124, 348-355.

Hui-min, F., Fang-wen, H., Guo-ping, Z., Liang, Y., Zhong-min, L., 2010. Application of CFD Technique in the Design and Flow Analysis of the Implantable Axial Flow Blood Pump. Journal of Hydrodynamics, 22, 518-525.

Jayakumar, J., Mahajani, S., Mandal, J., Iyer, K., Vijayan, P., 2010. Thermal Hydraulic Characteristics of Air–Water Two-Phase Flows in Helical Pipes. Chemical Engineering Research and Design, 88, 501-512.

Kaewnai, S., Chamaoot, M., Wongwises, S., 2009. Predicting Performance of Radial Flow Type Impeller of Centrifugal Pump Using CFD. Journal of Mechanical Science and Technology, 23, 1620-1627.

Kim, J.H., Duffey, R.B., Belloni, P., 1985. On Centrifugal Pump Head Degradation in Two-Phase Flow. Design method for two-phase flow in Turbomachinery. ASME Mechanics Conference, 26 Albuquerque, NM.

Majidi, K., 2005. Numerical Study of Unsteady Flow in a Centrifugal Pump. Journal of Turbomachinery, 5, 363-371.

Medvitz, R., Kunz,R., Boger, D., Lindau, J., Yocum, A., Pauley, L., 2002. Performance Analysis of Cavitating Flow in Centrifugal Pumps Using Multiphase CFD. Journal of Fluids Engineering, 124, 377-383.

Mikielewicz, J., Wilson, G., Chan, D., Goldfinch, A., 1978. A Method for Correlating the Characteristics of Centrifugal Pumps in Two-Phase Flow. Journal of Fluid Engineering , 100, 395-409.

Minemura, K., Uchiyama, S., Shoda, Kazuyuki, E.,1998. Prediction of Air-Water Two-Phase Flow Performance of a Centrifugal Pump Based on One-Dimensional Two-Fluid Model. Journal of Fluids Engineering, 120, 327-334.

Murakami, M., Minemura, K., 1974a. Effects of Entrained Air on the Performance of a Centrifugal Pump (First Report, Performance and Flow Conditions). Bulletin of the ASME, 1047-1055.

Murakami, M., Minemura, K., 1974b. Effects of Entrained Air on the Performance of a Centrifugal Pump (Second Report, Effects of Number of Blades). Bulletin of the ASME, 1286-1295.

Pak, E. T., Lee, J. C., 1998. Performance and Pressure Distribution Changes in a Centrifugal Pump under Two Phase Flow. Journal of Power and Energy, 212, 165-171.

Pessoa, Rui, Prado, M., 2003. Two-Phase Flow Performance for Electrical Submerisble Pump Stages. SPE Production & Facilities . New Orleans: SPE, 13-27.

Poullikkas, A., 2003. Effects of Two-Phase Liquid-Gas Flow on the Performance of Nuclear Reactor Cooling Pumps. Progress in Nuclear Energy, 42.1. 3-10.

Sachdeva, R., Doty, D., Schmidt, Z., 1994. Performance of Electrical Submersible Pump in Gassy Wells. SPE. 22767. SPE. 22767.

Sato, S., Furukawa, A., Takamatsu, Y., 1996. Air-Water Two-Phase Flow Performance of Centrifugal Pump Impellers with Various Blade Angles. ASME International Journal, 39.2, 223-229.

Schilling, R., Frobenius, M., 2002. Numerical Simulation of the Two Phase Flow in Centrifugal Pump Impeller. ASME FEDSM. Montreal, Quebec, Canada: ASME, 2002. 859-865.

Schobeiri, M., 2005. Turbomachinery Flow Physics and Dynamic Performance. Berlin: Springer.

Sun, D., 2002. Modeling Gas-Liquid Head Performance of Electrical Submersible Pumps. Ph.D. Dissertation , Tulsa: The University of Tulsa, Tulsa OK.

Suryawijaya, P., Kosyna, G., 2001. Unsteady Measurement of Static Pressure On the Impeller Blade Surfaces and Optical Observation on Centrifugal Pumps Under Varying Liquid/Gas Two-Phase Flow Condition. Journal of Computational and Applied Mechanics, 2.1, D9-D18.

Takemura, Kato, T., H., Kanno, H., 1997. Development of Rotordynamic Multiphase Pump: The First Report. Pipeline Technology, 5.

Thum, D., Hellmann, H., Sauer, M., 2006. Influence of the Patterns of Liquid-Gas Flows on Multiphase-Pumping of Radial Centrifugal Pumps. 5th North American Conference on Multiphase Technology. 79-90.

Tonomura, O., Tanaka, S., Noda, M., Kano, M., Hasebe, S., Hashimoto, I., 2004. CFD-Based Optimal Design of Manifold in Plate-Fin Microdevices. Chemical Engineering Journal, 101, 397-402.

Wilson, D., Chan, T., Manzano-Ruiz, J., 1979. Analytical Models and Experimental Studies of Centrifugal-Pump Performance in Two-Phase Flow. MIT, Cambridge, Massachusetts. EPRI NP-677.

Yang, Z, Peng, X., Ye, P., 2008. Numerical and Experimental Investigation of Two Phase Flow During Boiling in A Coiled Tube. International Journal of Heat and Mass Transfer, 51, 1003–1016.

Yedidiah, S., 2006a. Application of CFD to the Design of Centrifugal Pumps. Proceedings of 2006 ASME Joint U.S.-European Fluids Engineering Summer Meeting. Miami, Florida, United States: FEDSM, 2006a.

Yedidiah, S., 2006b. Translating Equations into Their Physical Meaning, as an Effective Tool of Engineering. Proceedings of ASME Fluids Engineering Division Summer Meeting. Miami, Florida, United States : FEDSM, 201-208.

Zakem, S., 1980. Determination of Gas Accumulation and Two-Phase Slip Velocity Ratio in a Rotating Impeller. Journal of Fluids Engineering, 102, 446-455.

APPENDIX A

SINGLE PHASE SIMULATION CFD RESULTS

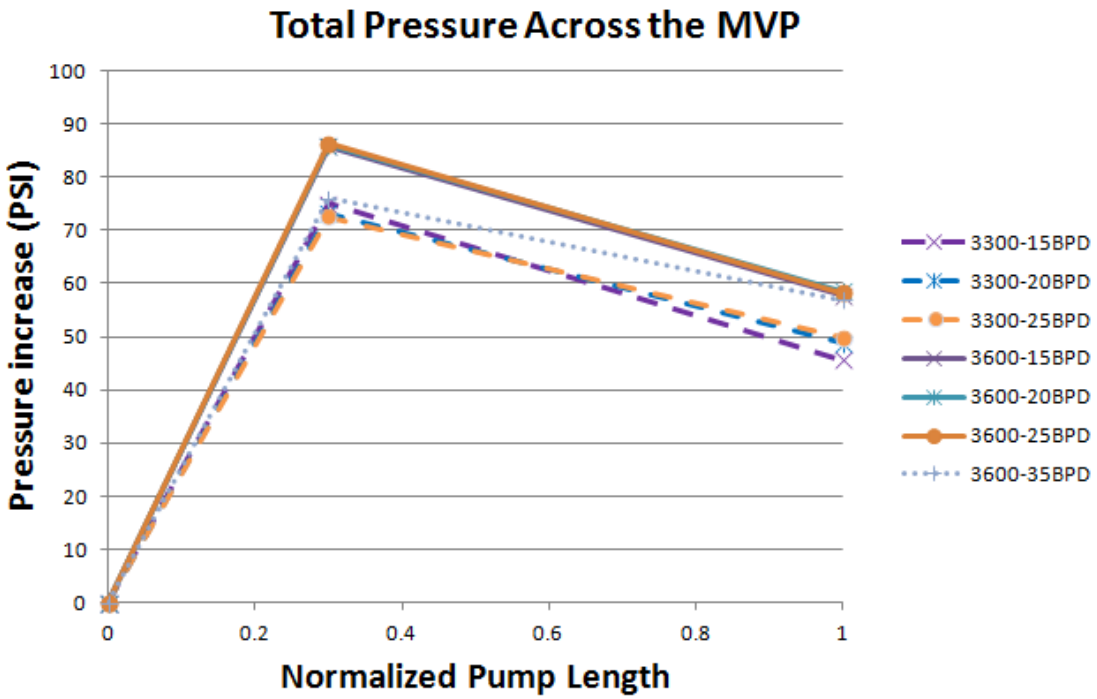

Figure A 1 Total pressure across a single stage MVP

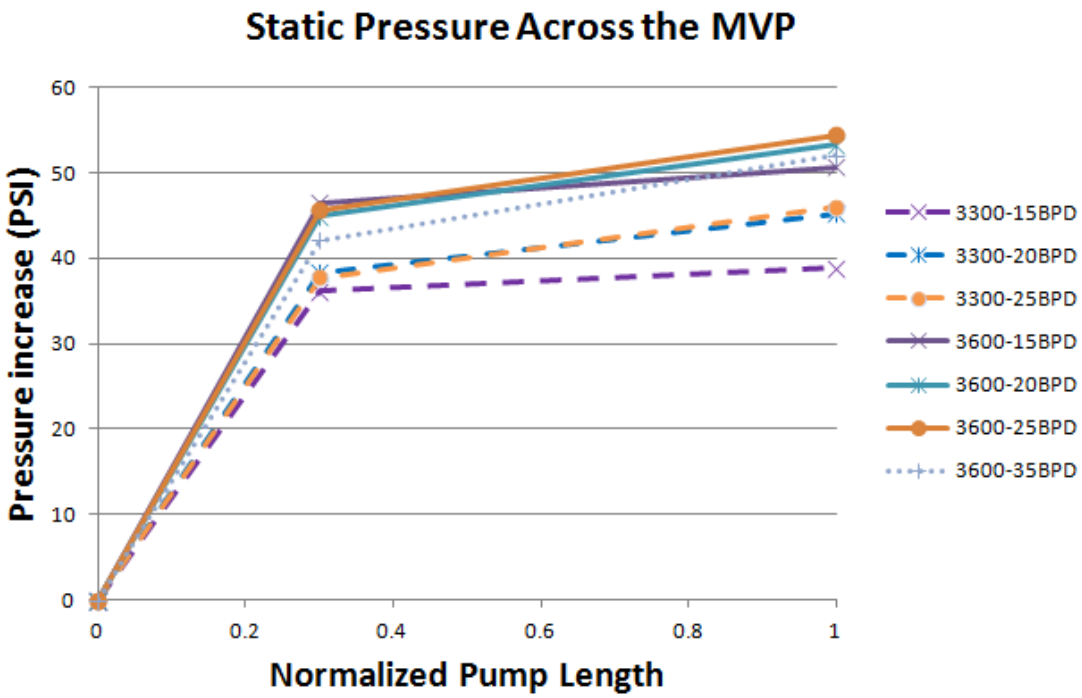

Figure A 2 Static pressure across a single stage MVP

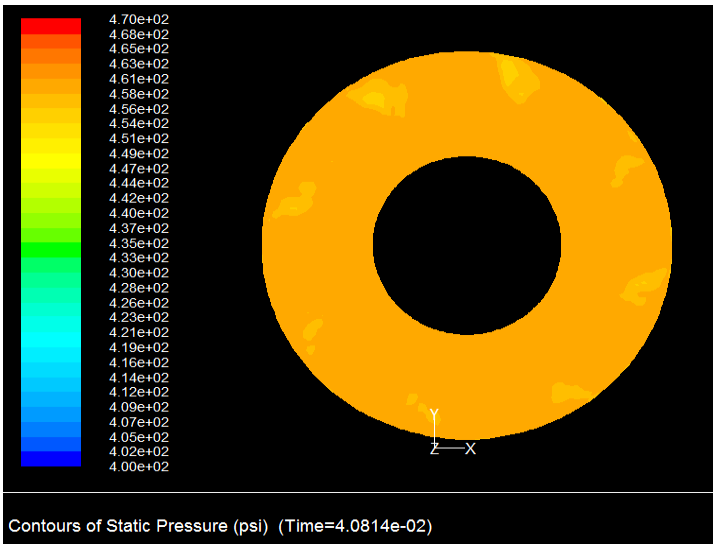

Figure A 3 Outlet static pressure distribution at 3300 rpm and 15 KBPD for single phase flow

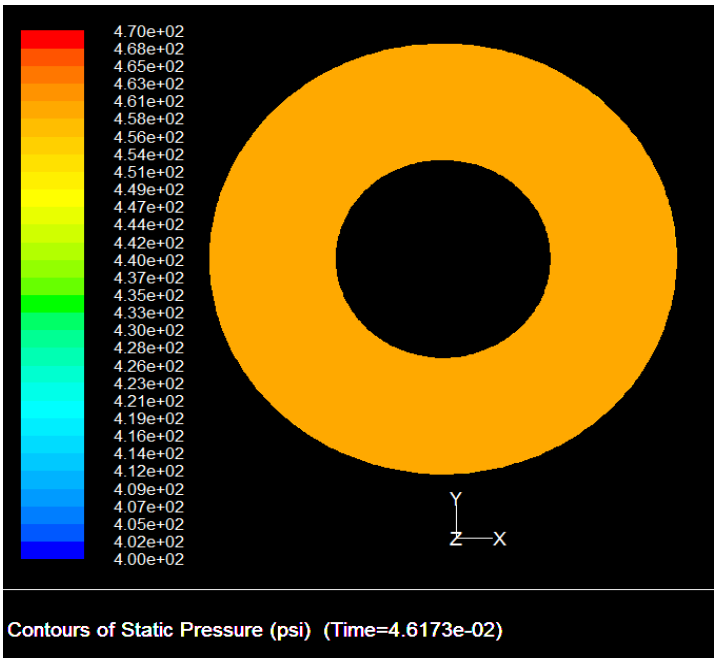

Figure A 4 Outlet static pressure distribution at 3300 rpm and 20 KBPD for single phase flow

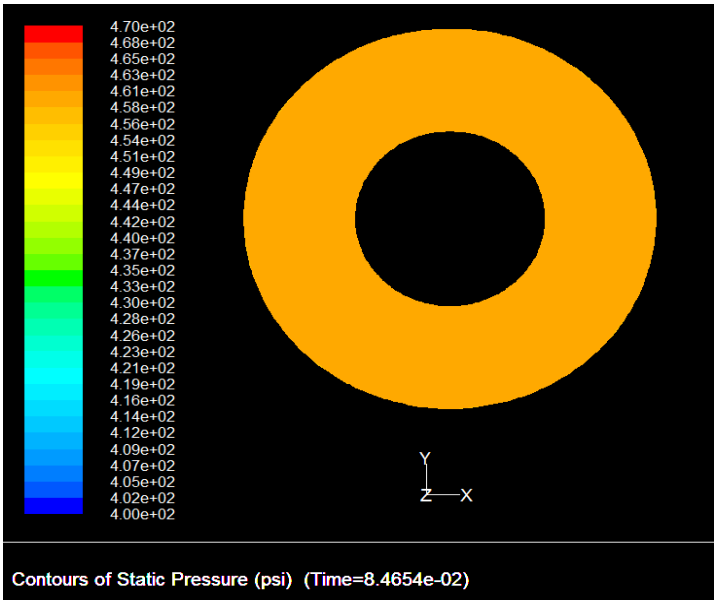

Figure A 5 Outlet static pressure distribution at 3300 rpm and 25 KBPD for single phase flow

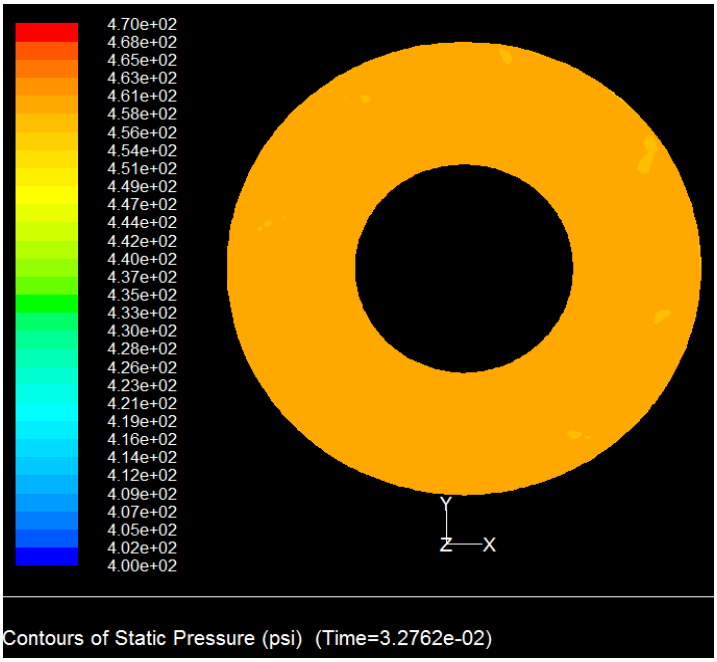

Figure A 6 Outlet static pressure distribution at 3600 rpm and 15 KBPD for single phase flow

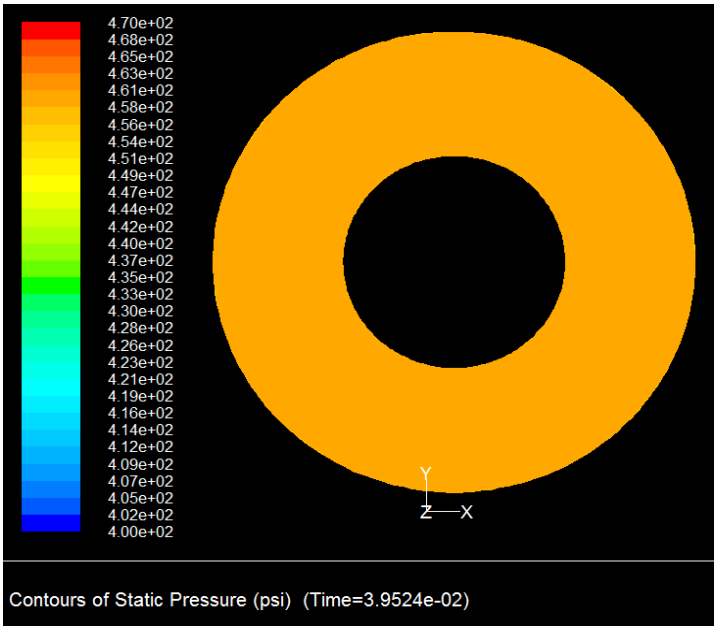

Figure A 7 Outlet static pressure distribution at 3600 rpm and 20 KBPD for single phase flow

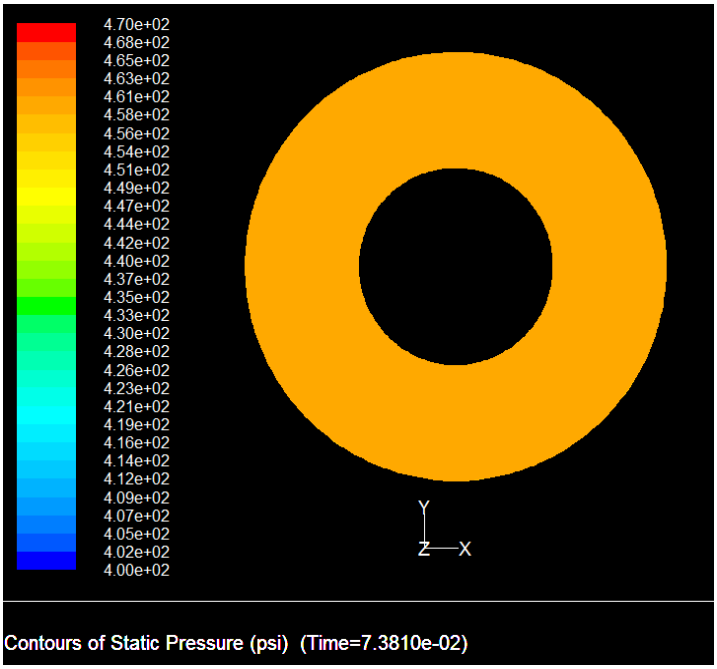

Figure A 8 Outlet static pressure distribution at 3600 rpm and 25 KBPD for single phase flow

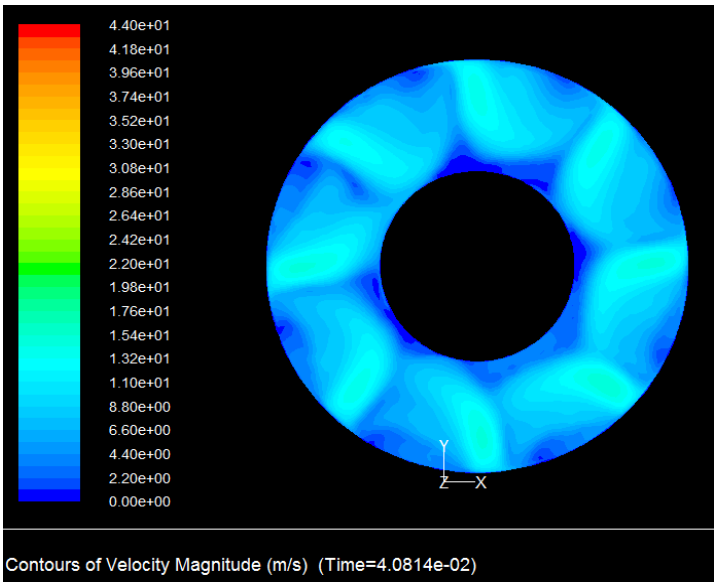

Figure A 9 Outlet velocity magnitude distribution at 3300 rpm and 15 KBPD for single phase flow

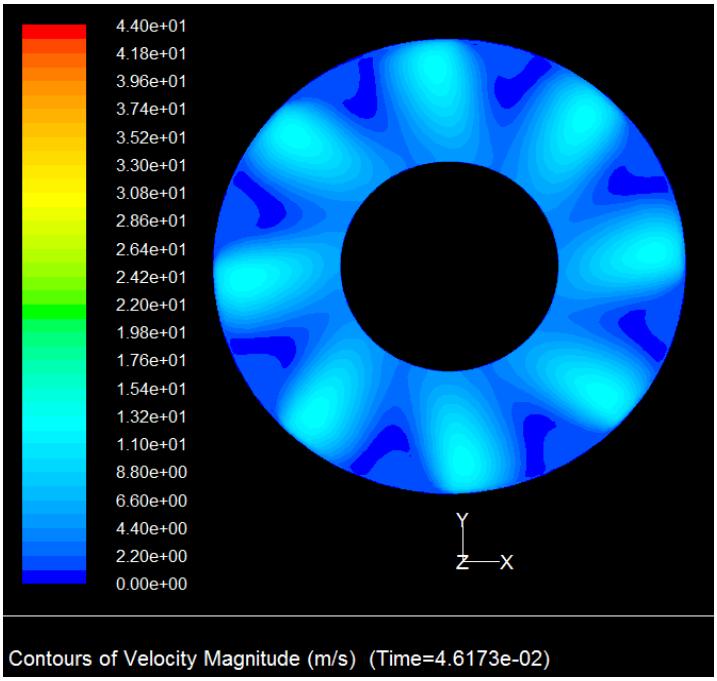

Figure A 10 Outlet velocity magnitude distribution at 3300 rpm and 20 KBPD for single phase flow

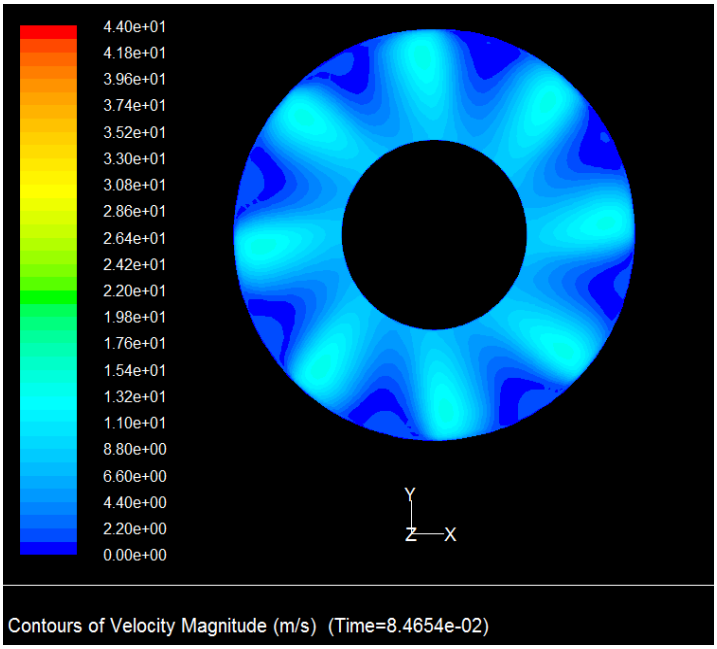

Figure A 11 Outlet velocity magnitude distribution at 3300 rpm and 25 KBPD for single phase flow

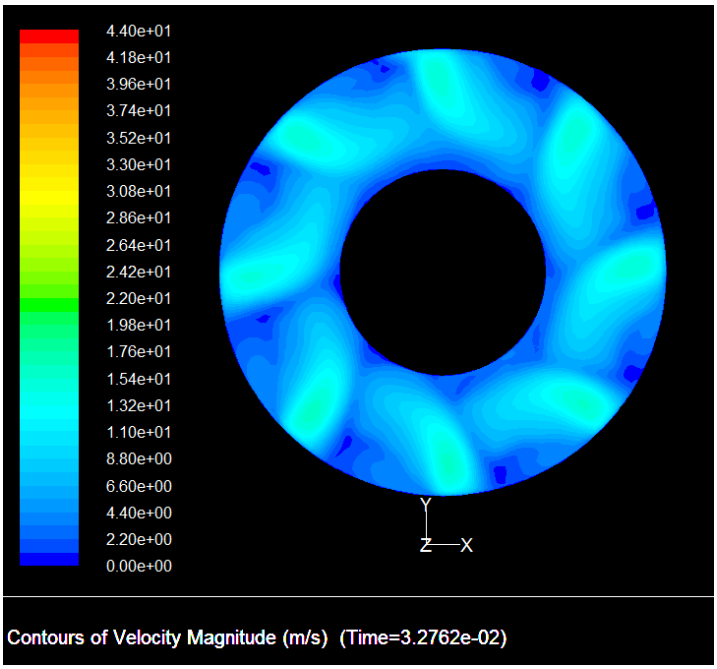

Figure A 12 Outlet velocity magnitude distribution at 3600 rpm and 15 KBPD for single phase flow

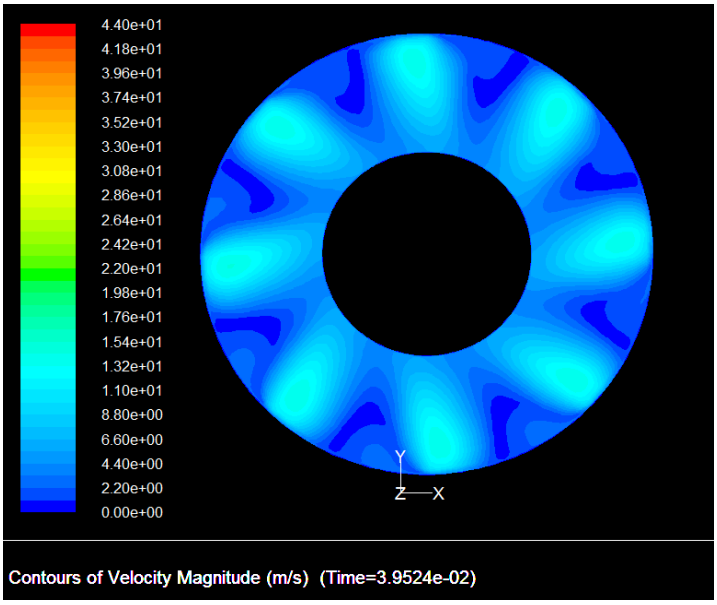

Figure A 13 Outlet velocity magnitude distribution at 3600 rpm and 20 KBPD for single phase flow

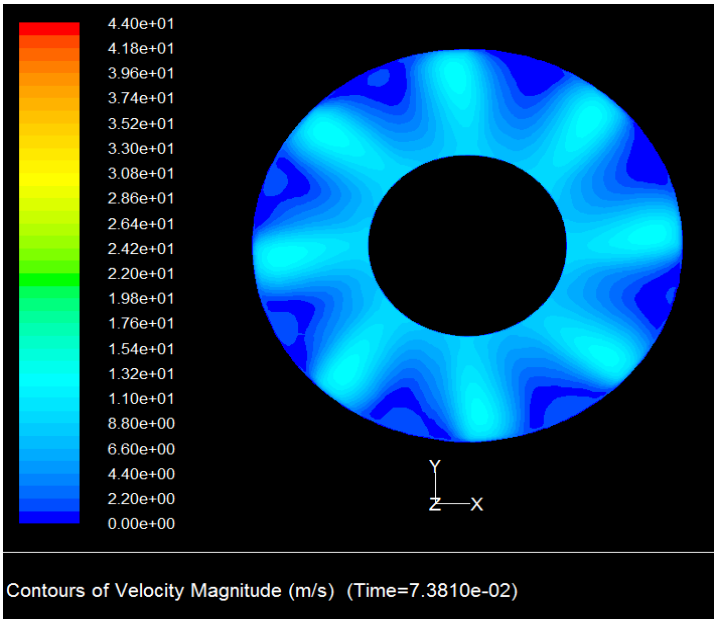

Figure A 14 Outlet velocity magnitude distribution at 3600 rpm and 25 KBPD for single phase flow

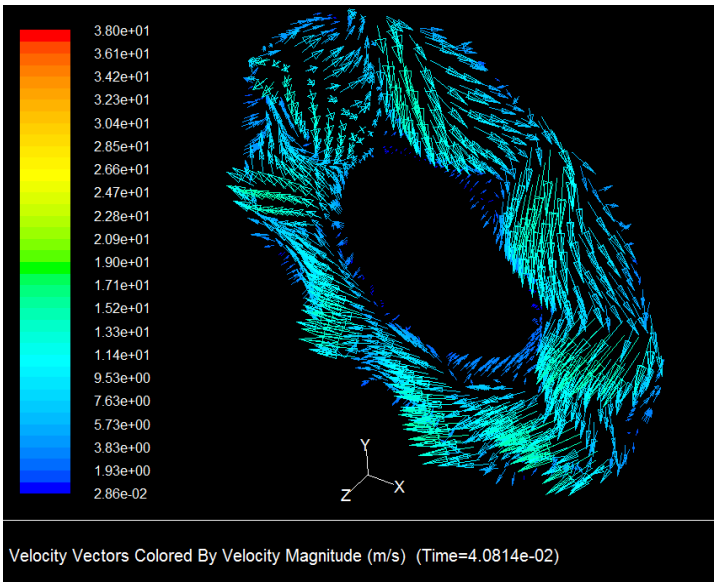

Figure A 15 Outlet velocity vectors distribution at 3300 rpm and 15 KBPD for single phase flow

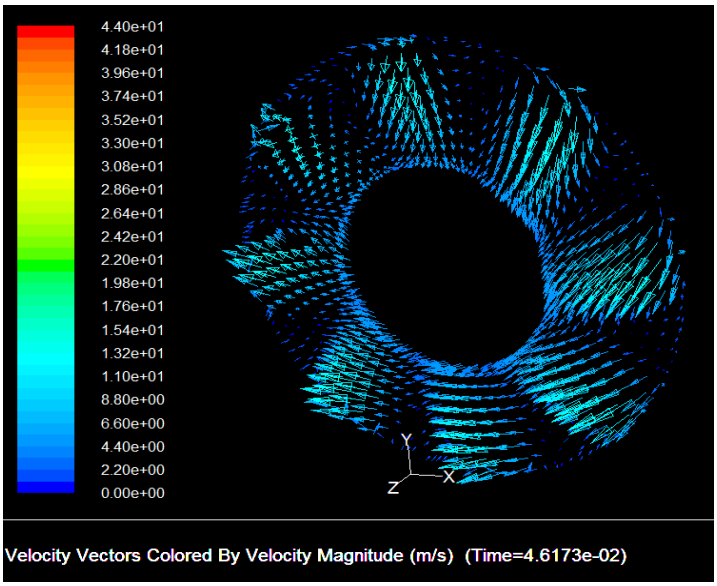

Figure A 16 Outlet velocity vectors distribution at 3300 rpm and 20 KBPD for single phase flow

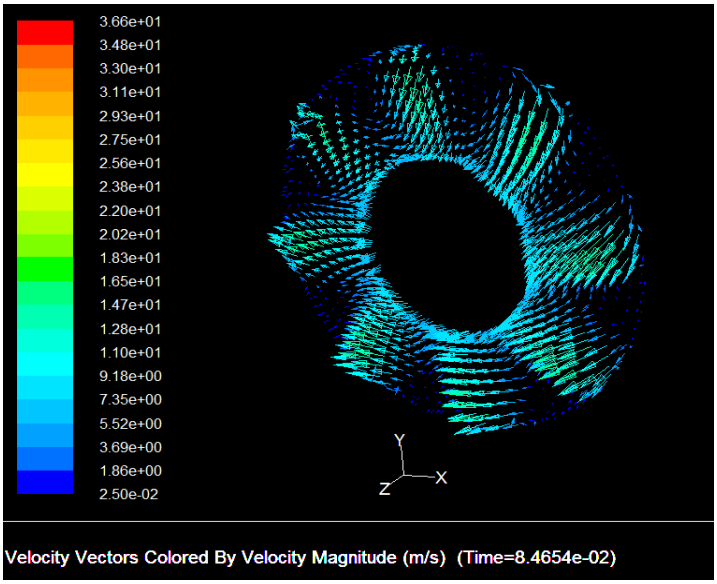

Figure A 17 Outlet velocity vectors distribution at 3300 rpm and 25 KBPD for single phase flow

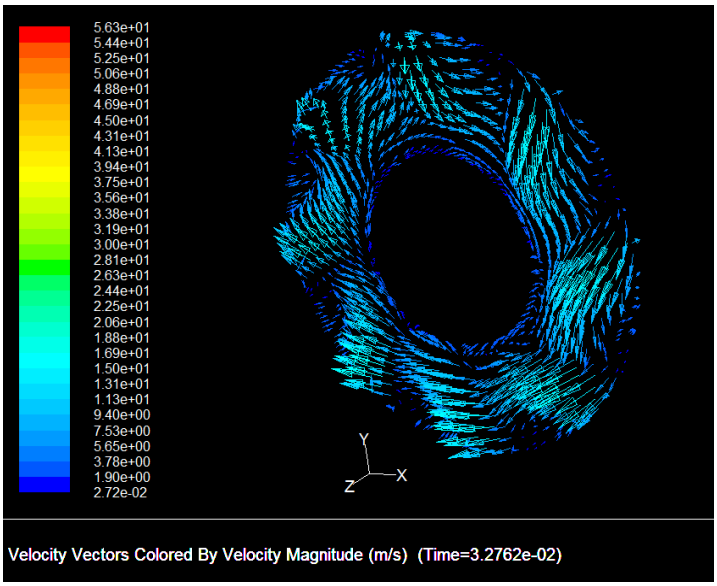

Figure A 18 Outlet velocity vectors distribution at 3600 rpm and 15 KBPD for single phase flow

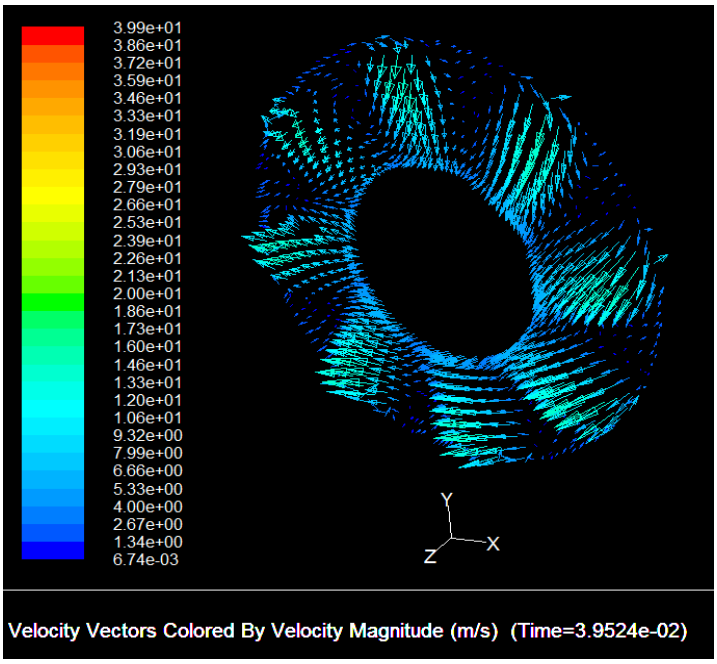

Figure A 19 Outlet velocity vectors distribution at 3600 rpm and 20 KBPD for single phase flow

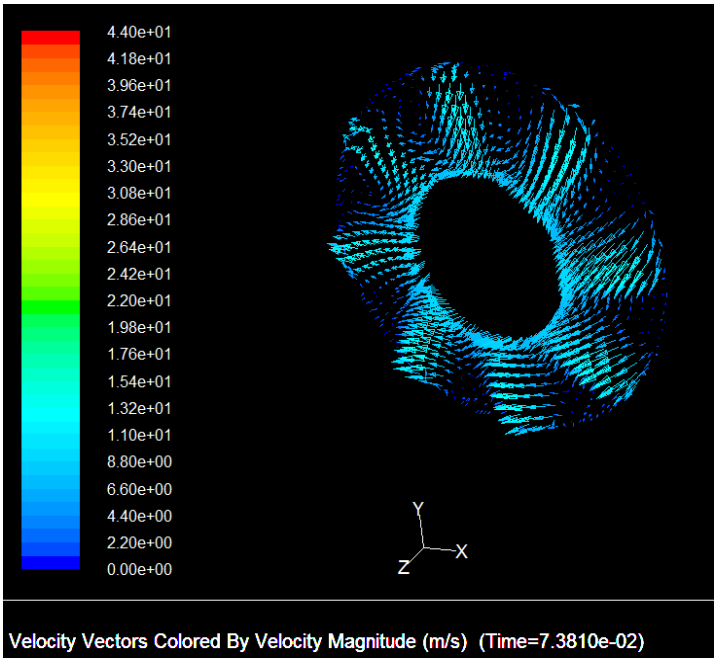

Figure A 20 Outlet velocity vectors distribution at 3600 rpm and 25 KBPD for single phase flow

APPENDIX B

TWO PHASE SIMULATION CFD RESULTS

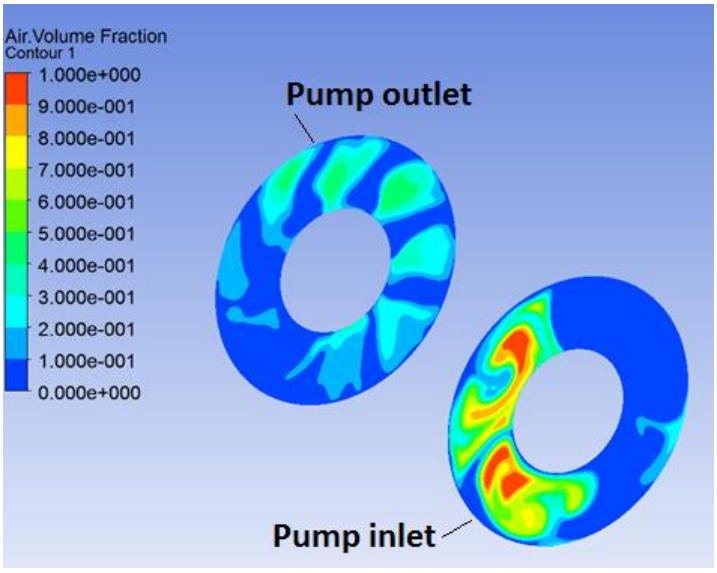

Figure B 1 GVF distribution at the pump inlet and pump outlet with the inlet mixing chamber simulated with the first stage at 400 psi inlet pressure, 30 KBPD, and 32% GVF at the inlet

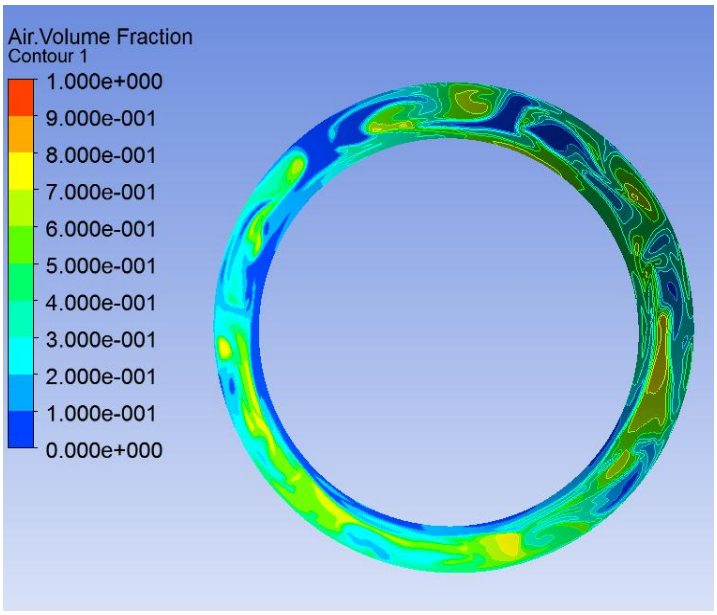

Figure B 2 GVF distribution at the impeller/diffuser interface with the inlet mixing chamber simulated with the first stage at 400 psi inlet pressure, 30 KBPD, and 32% GVF at the inlet

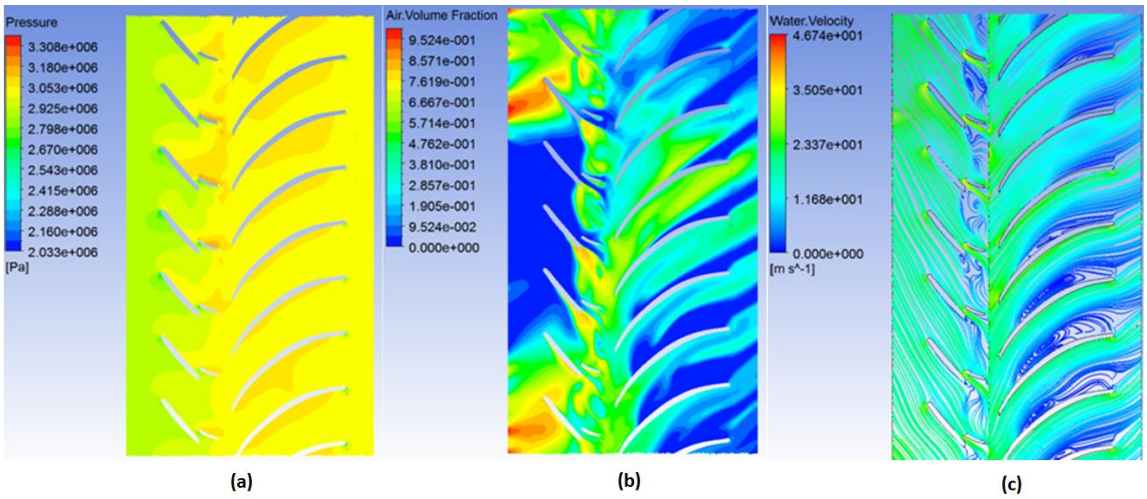

Figure B 3 (a) Static pressure, (b) GVF distribution, and (c) water velocity streamlines at the pump middle plane with the inlet mixing chamber simulated with the first stage at 400 psi inlet pressure, 30 KBPD, and 32% GVF at the inlet

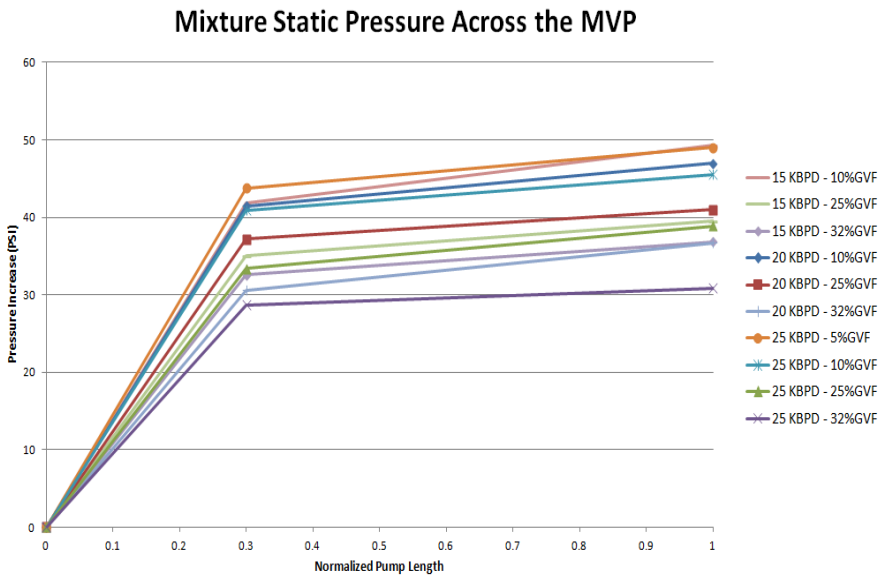

Figure B 4 Mixture static pressure across the MVP at 950 psi inlet pressure and 3600 rpm

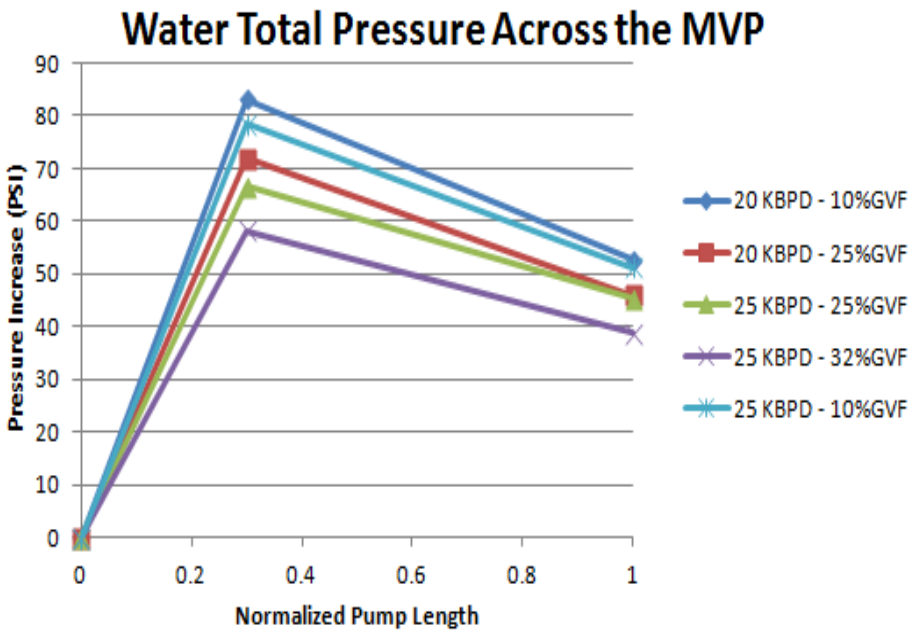

Figure B 5 Water total pressure across the MVP at 950 psi inlet pressure and 3600 rpm

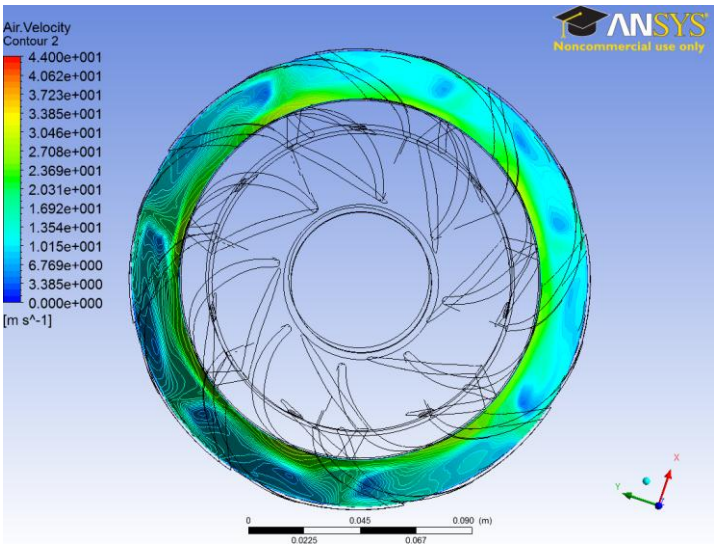

Figure B 6 Air velocity at the impeller/diffuser interface at 10% GVF inlet, 3600 rpm and 25 KBPD

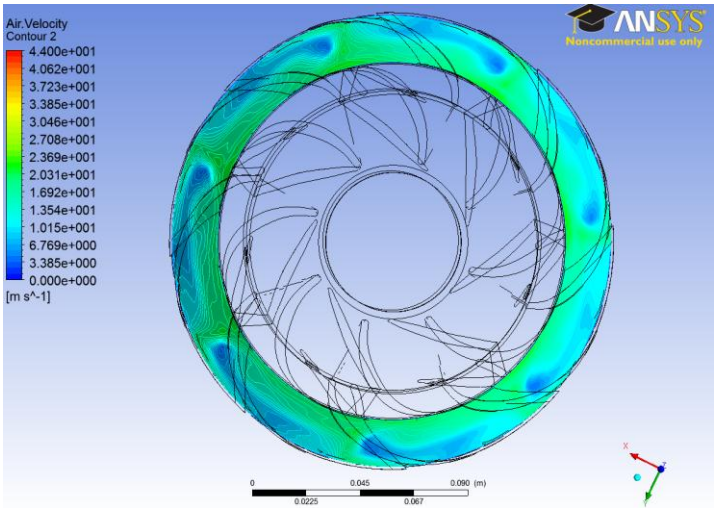

Figure B 7 Air velocity at the impeller/diffuser interface at 25% GVF inlet, 3600 rpm and 25 KBPD

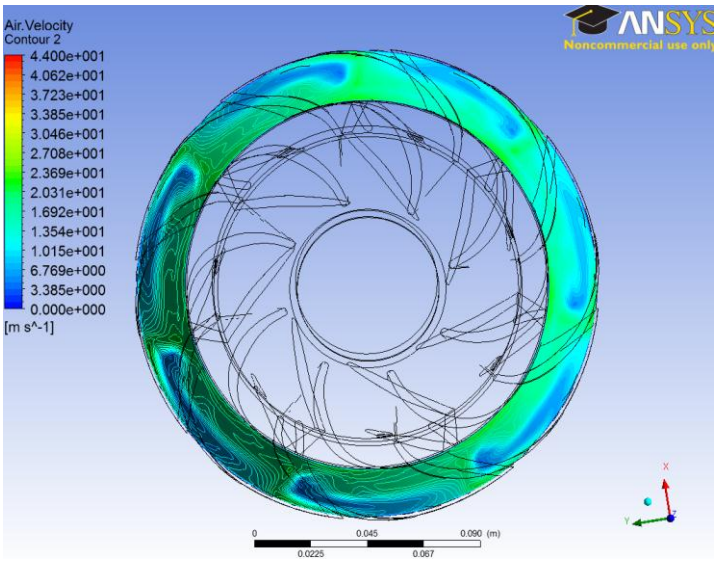

Figure B 8 Air velocity at the impeller/diffuser interface at 32% GVF inlet, 3600 rpm and 25 KBPD

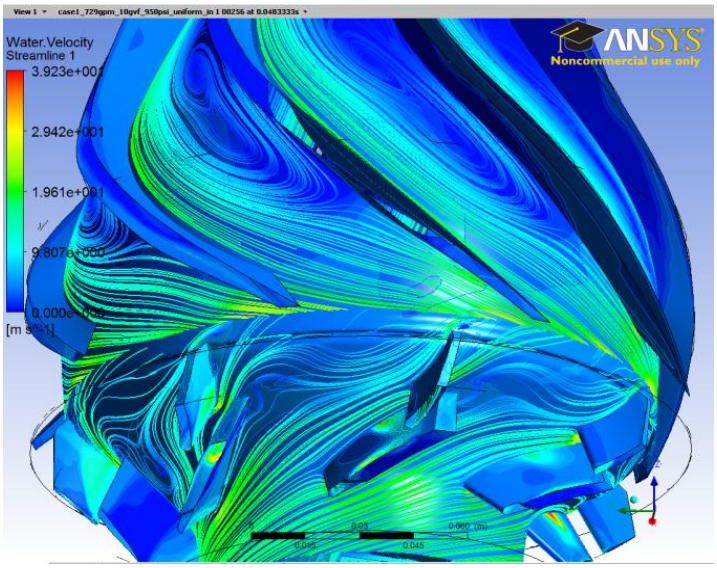

Figure B 9 Velocity streamlines shown on the GVF contour plot distribution at the pump middle plane at 10% GVF inlet, 3600 rpm and 25 KBPD

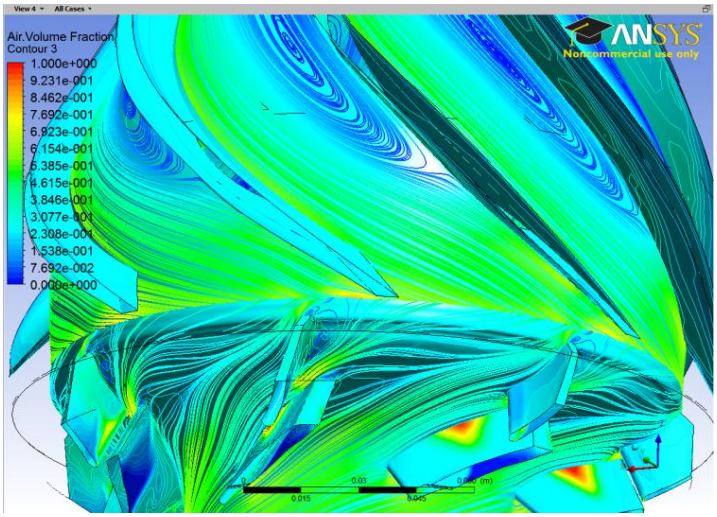

Figure B 10 Velocity streamlines shown on the GVF contour plot distribution at the pump middle plane at 25% GVF inlet, 3600 rpm and 25 KBPD

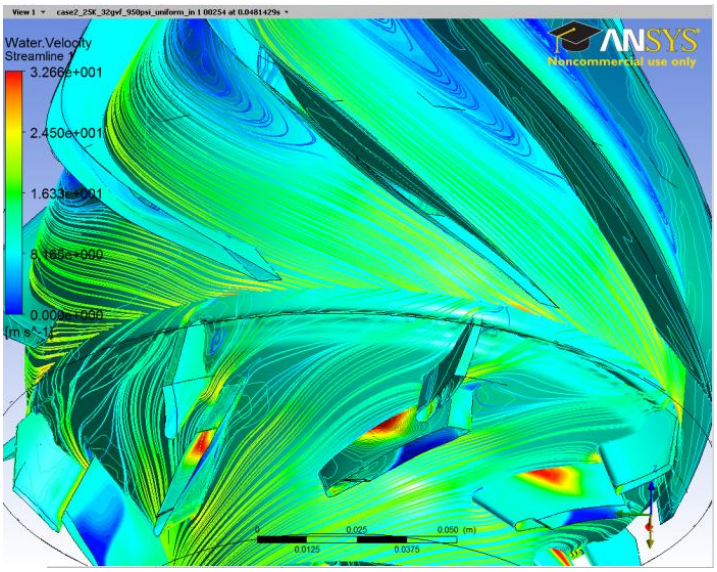

Figure B 11 Velocity streamlines shown on the GVF contour plot distribution at the pump middle plane at 32% GVF inlet, 3600 rpm and 25 KBPD

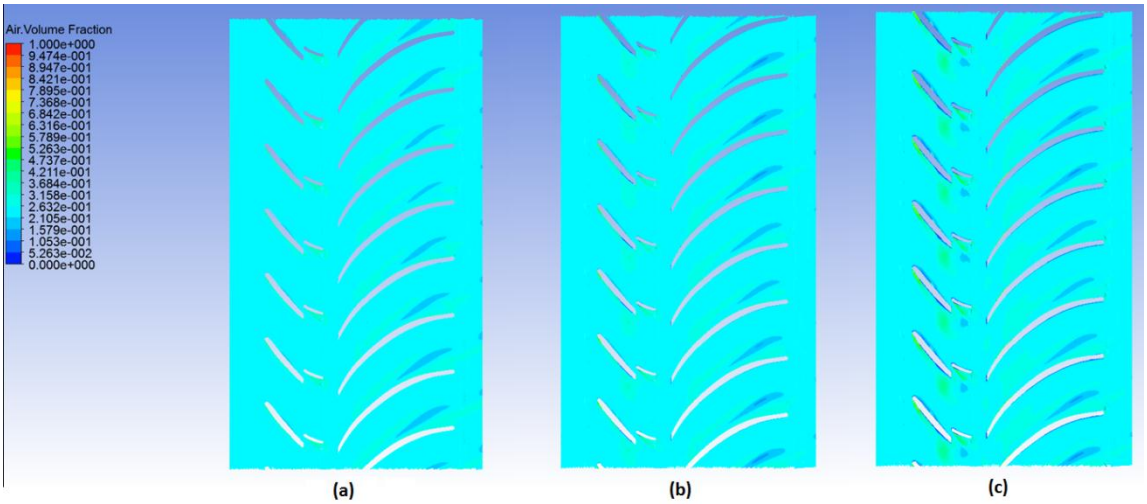

Figure B 12 GVF distribution across the middle plane of a single stage MVP at 25 KBPD, 25% GVF inlet, 3600 rpm, 950 psi inlet pressure, (a) bubble size 0.01 mm, (b) bubble size 0.02 mm, (c) bubble size 0.05 mm